

# Investigating the Role of Charge Imbalance on the Luminescence Production of Quartz and Feldspar

**Autzen, Martin**

*Publication date:*
2018

*Document Version*
Publisher's PDF, also known as Version of record



# Investigating the role of charge imbalance on the luminescence production of quartz and feldspar

Submitted for

PhD Thesis

Martin Autzen

September 30th 2018

Supervisor: Jan-Pieter Buylaert
Co-supervisor: Mayank Jain

DTU Nutech
Center for Nuclear Technologies

# Abstract

Luminescence dosimetry is now routinely employed in accident dosimetry and geochronological and archaeological studies, using natural minerals such as quartz and feldspar as dosimeters. Quartz and feldspar are the most common minerals in the regolith and can be used to record events related to such diverse phenomena as climate and landscape change, tectonic activity, catastrophic events, and human evolution/migration. Since luminescence dosimetry relies on the relationship of trapped charge and dose, and the recombination of trapped electrons with trapped holes, it is important to know how charge trapping relates to dose, and how trapping and recombination occur in nature and in the laboratory.

Dose distributions derived from measurements of luminescence from individual grains are often used to investigate whether a sample was completely reset or zeroed before final burial. However, the resulting dose distributions are almost always wider than can be explained by known measurement uncertainties. Some part of this over-dispersion may arise from differences in irradiation geometry at a scale of individual grains. In particular, there may be grain-to-grain variations in the charge balance. This thesis investigates whether a net excess of electrons or holes exists as a result of natural and/or laboratory irradiation, and whether such a charge imbalance can have an influence on the luminescence production of quartz.

Initial results showed that the over-dispersion of single grains increases with an increase in atomic number of the backscattering material. This coincides with an increase in dose rate resulting from an increased contribution from the backscattered spectrum. For a given backscattering material, degrading the incoming beta spectrum by passing it through an attenuator also leads to an increase in the observed over-dispersion. Both results indicate that low energy electrons may play a key role in over-dispersion. Surprisingly, it is also observed that feldspar experiences a $\sim$15% lower apparent beta source dose rate than quartz. This is despite their very similar composition; modelling shows that the two minerals have indistinguishable dose deposition when exposed to either beta or gamma radiation. It is con-

cluded that the difference in apparent dose rates is most likely to arise from differences in charge trapping and recombination, rather than the actual dose deposition, although the details of this remain unknown.

Charge imbalance during natural and laboratory beta and gamma irradiation is then investigated using radiation transport modelling. As far as is known, this is the first time this phenomenon has been considered in luminescence dosimetry. Simulations show that quartz grains acquire a net charge during external irradiations with charged particles; these modelling predictions form the basis for experiments investigating the impact of excess electrons at very large (hundreds of kGy to MGy) doses. As predicted, a depression of both luminescence production and sensitivity is observed with increasing dose from a 200 keV electron beam. This observation is attributed to the recombination by excess electrons of the trapped hole populations giving rise to luminescence. This conclusion is supported by further experiments comparing the effects of irradiating with a lower (100 keV) electron energy. In addition, these electron beam experiments suggest that the excess electron concentrations at high doses increase to the point that they generate electric fields sufficient to repel incoming electrons; this reduces and ultimately prevents further absorption of dose by the sample.

Because luminescence is a two stage process (electron detrapping and recombination) it does not give direct information on the behaviour of the trapped electron population alone. To allow investigations to study electron and hole populations separately, a new detector was designed and constructed to measure the electrons which leave the surface of individual grains; these electrons are known to derive from the same traps as the luminescence signals. The design and testing of the instrument is described, and preliminary results presented which show that it is capable of useful measurements of electrons emitted by a single quartz grain. Unfortunately, there was insufficient time to make use of this new detector to investigate over-dispersion, and so these preliminary results are included in an appendix.

# Resume

Luminescens dosimetri bliver rutinemæssigt brugt i uheldsdosimetri og geokronologi og arkæologiske studier ved at bruge naturlige mineraler såsom kvarts og feldspat som dosimetre. Kvarts og feldspat er de mest almindelige mineraler i regolitten og kan bruges til at dokumenterer såforskellige begivenheder såsom klima og landskabsændringer, tektonisk aktivitet, katastrofale begivenheder, og menneskets evolution/migration. Eftersom luminescens dosimetri bygger påforholdet mellem den lagrede ladning og dosis, såvel som rekombinationen mellem lagrede elektroner med lagrede huller, er det vigtigt at vide hvordan ladnings lagringen relaterer til dosis og hvordan lagringen og rekombination forløber i naturen og i laboratoriet.

Dosis fordelinger udledt fra luminescens målinger fra individuelle korn bliver ofte brugt til at undersøge om en prøve blev komplet nulstillet før den endelige begravelse. De resulterende fordelinger er dog næsten altid bredere end det der kan forklares ud fra kendte målings usikkerheder. En del af denne over-dispersion kommer måske fra forskelle i bestrålingsgeometri nede påenkelt-korns planet. Navnligt kan der være forskellige i ladningsbalancen fra korn til korn. Denne afhandling undersøger om et overskud af elektroner eller huller eksisterer pågrund af bestråling i naturen og/eller laboratoriet og om sådan en ladningsulighed kan have en indflydelse påluminescens produktionen fra kvarts.

De første resultater viste at over-dispersion fra enkelte korn stiger med en stigning i det atomare tal for det tilbagespredende materiale. Dette falder sammen med en stigning i dosis hastigheden pågrund af en større andel fra det tilbagespredte spektrum. For et givent tilbagespredende materiale stiger over-dispersion hvis det indkommende beta spektrum degraderes ved at passerer det igennem en attenuator. Begge resultater indikerer at lav energi elektroner muligvis spiller en vigtig rolle i over-dispersion. Overraskende nok observeres det ogsåat feldspat har en $\sim$15% lavere tilsyneladende dosis hastighed end kvarts. Dette er påtrods af deres lignende komposition;

simuleringer viser at de to mineraler har identisk dosis deponering når de bliver udsat for beta eller gamma stråling. Det konkluderes at forskellen i tilsyneladende dosis hastigheder sandsynligvis kommer fra forskelle i ladnings lagring og rekombination i stedet for faktisk dosis deponering selvom detaljerne for dette stadig er ukendte.

Ladningsulighed under beta og gamma bestrålinger i naturen og laboratoriet bliver herefter undersøgt ved brug af strålings transport simuleringer. Såvidt vides er dette første gang dette fænomen er blevet betragtet i luminescens dosimetri. Simuleringer viser at kvarts korn får en ladning under eksterne bestrålinger med ladede partikler; disse modellerings forudsigeler danner basis for eksperimenter der undersøger indvirkningen af overskydende elektroner ved meget høje (hundredvis af kGy til MGy) doser. Som forudset observeres der en svækkelse af både luminescens produktion og sensitivitet med stigende dosis givet med en 200 keV elektron stråle. Denne observation tilskrives rekombinationen af de overskydende elektroner med populationerne af lagrede huller der danner grundlag for luminescens. Denne konklusion understøttes af videre eksperimenter hvor effekterne ved bestråling med en lavere elektron energi (100 keV) sammenlignes. Udover dette antyder disse elektronstråle forsøg ogsåat koncentrationerne af overskydende elektroner ved høje doser stiger til en sådan grad at de generer et elektrisk felt der er stærkt nok til at frastøde de indkommende elektroner; dette reducerer og i sidste ende forhindrer prøven i at videre absorberer dosis.

Eftersom at luminescens er en to-stadie proces (elektron aflagring og rekombination) giver det ikke direkte information om hvordan den lagrede elektroner population opfører sig alene. En ny detektor blev designet og konstrueret der kan måle elektroner som forlader overfladen af enkelte korn for at undersøge elektron og hul populationerne separat; det vides at disse elektroner kommer fra de samme får lder som luminescens signalerne. Både design og test af instrumentet beskrives samt foreløbige resultater som viser at instrumentet kan bruges til nødige målinger af udstrålte elektroner fra enkelte kvarts korn. Desværre var der ikke nok tid til at gøre brug af denne nye detektor til at under over-dispersion og derfor er disse foreløbige resultater inkluderet i appendiks.

# Acknowledgements

Over the past three years, I have had the pleasure and privilege to work with, alongside, visit and be around fantastic and amazing people who have all helped shape this work in some way. I would like to thank everyone, I couldn't have done it without you. Before I start, I would like to thank the European Research Council (ERC) for funding through the EU Horizon 2020 programme ERC-2014-StG 639904 - RELOS.
First of all, thank you to my supervisor Jan-Pieter Buylaert who has been nothing but supportive and encouraging throughout the entire project. You have been an amazing teacher, always keen to listen and give me the chance to run with a new idea or tell me to focus on something more beneficial.

Secondly, I'd like to thank my co-supervisor Mayank Jain for helping me through much of the physics, your many input and ideas on new experiments which made this project what it is today, as well helping me when I got stuck.

I have been lucky enough to have two "non-supervisor" supervisors; Andrew Murray, we have had many discussions, some which left me frustrated for a few hours, but you have always been there with advice or as a sounding board for new ideas or problems, they have always made me better at what I do and for that I can not thank you enough . The second "non-supervisor" was Nigel Poolton, who I had the great pleasure of sharing a lab with for a year and who designed the new exo-electron system. You gave me a practical and fundamental introduction to instrumentation and luminescence physics which I have used every day of my thesis and I look forward to your next visit for more discussions about where we can go and new stories.

I have visited Guillaume Guérin and his group at Université Bordeaux multiple times, each time learning a bit more about GEANT4 than I did before. Thank you, Guillaume for teaching me how to code, for our many discussion on luminescence physics and always being very helpful when I inevitably crashed my code. I look forward to many more visits. I also got to visit Luis Baly at Centro Aplicacions Tecnológicas y Desarrollo Nuclear

(CEADEN) in Havanna, Cuba for a month during the "winter" of 2017. Thank you for showing me around and making me feel very welcome in your lab and your country.

Thank you to all the PhD students who I've been lucky enough to share an office with for the past three years as well the the trials and tribulations of finishing a PhD thesis on time; Grichar, Jeppe, Trine, Patrick, Rocio, Amit, Raju, Nicolo, Nikola, Nicolai, Jakob, Ashken, and Susanne. Thank you to Eike Rades for bringing me Katla hunting near Vimmerby, sampling an active, live shooting range, and a particularly memorable trip to Portual sampling rock art as well as our many climbing sessions, it has made my time a lot more fun. It has been a pleasure to work with the "Grand Old Lady of Exo-Electrons" Christina Ankjærgaard, thank you for all your input on the new exo-electron work, support and encouragement, I look forward to tackling our new common hobby; charge imbalance. Thank you to Reza Sohbati for many discussions, jokes and good times on conferences, lunch or just making a tedious measurement procedure a lot more entertaining. Thank you to Kristina Thomsen for showing me the wonderful world of single-grain luminescence, all the little tips and tricks for dealing grains that are stuck or the high-tech method for avoiding vibrations when turning the wheel. A huge thank you to the High Dose Reference Lab (Arne, Mark, Nina, Linda, Claus, Lars and Torben) for irradiating my samples and all the wear and tear I have put on the electron beam. Our secretaries, Merete Larsen and Pia Elhauge, have always been ready to provide answers to the many questions I have asked regarding forms, courses, teaching, travel expenses as well as handing in this thesis and moving to the next thing, your help has been invaluable.

Thank you to our wonderful technicians, Vicki Hansen, Louise Helsted, Warren Thompson and Eun-Young Yeo for their invaluable help in putting my samples through chemistry, saving me (and the immediate surroundings) from my failed chemistry career. Our talented and fantastic technical staff, Bo Dalsgaard, Per Sørensen, Lars Pirtzel, Finn Jørgensen, Karsten Nielsen, and Jørgen Jackobsen have been an incredible help with the integration of the exo-electron system as well every time a reader gave a new error message. Søren Dalsgaard has been integral in the design and construction of the exo-electron system as well as any new and exciting instrument or tool Andrew thought of and without his ability to build anything on short notice this thesis would be a lot shorter. Muyngho Kook has provided his technical expertise to the development of the exo-electron system, the use of the IRPL and spectrometer systems and his always cheery attitude has been a pleasure to share a lab with.

Finally, thank you my parents and Svenja for all your love and support,

helping me slow down when I was moving too fast, all the laughs, food and adventures.

# List of publications

Cunningham A. C., Murray, A. S., Armitage, S. J., **Autzen, M.** High-precision natural dose rate estimates through beta counting *Radiation Measurements* 2018 Accepted

**Autzen, M.**, Murray, A. S., Guérin, G. Baly, L. Ankjærgaard, C., Bailey, M., Jain, M., Buylaert, J.-P. Luminescence dosimetry: Does charge imbalance matter? *Radiation Measurements* 2018 Accepted

Murray, A. S., Helsted, L. M., **Autzen, M.**, Jain, M., Buylaert, J.P. Measurement of natural radioactivity: Calibration and performance of a high-resolution gamma spectrometry facility *Radiation Measurements* 2018 Accepted

Hansen, V., Murray, A., Thomsen, K., Jain, M. **Autzen, M.**, Buylaert, J.-P. Towards the origins of over-dispersion in beta source calibration *Radiation Measurements* 2018 Accepted

**Autzen, M.**, Guérin, G., Murray, A. S., Thomsen, K. J., Buylaert, J.-P., Jain, M. The effect of backscattering on the beta dose absorbed by individual quartz grains *Radiation Measurements* 2017:**106**:491-497

# List of acronyms

| | |
|---|---|
| $\mathbf{E_c}$ | Conduction band energy |
| $\mathbf{E_g}$ | Band gap |
| $\mathbf{E_T}$ | Electron trap depth |
| $\mathbf{E_v}$ | Valence band energy |
| **IR** | Infra-red |
| **IRSL** | Infra-red stimulated luminescence |
| **pIRIR** | post-IR IRSL |
| **K** | Non-luminescence centre |
| **L** | Luminescence centre |
| **OD** | Over-dispersion |
| **OSL** | Optically stimulated luminescence |
| **OSE** | Optically stimulated exo-electrons |
| **SMC** | Supplementary material for chapter |
| **T** | Electron trap |
| **TL** | Thermoluminescence |
| **TSE/TSEE** | Thermally stimulated exo-electrons |
| **Z** | Atomic number |

# Contents

# List of Figures

# List of Tables

# Chapter 1

# Introduction and overview

Thermally Stimulated Luminescence (TL) and Optically Stimulated Luminescence (OSL) are now routinely used in retrospective dosimetry to determine the exposure to ionising radiation (Bøtter-Jensen, 2003, p. xv). This is done using natural minerals or a synthetic compound with the ability to record and store a record of exposure as energy (actually as charge); these are called dosimeters because they are calibrated in terms of dose, the unit of which is Gray (Gy = J/kg absorbed from ionising radiation). One of the applications of retrospective dosimetry is luminescence dating - usually for archaeological and geological purposes using natural minerals such as quartz and feldspar. These natural dosimeters are the two most common minerals on Earth and are thus very suitable for dating events such as those related to human migration and evolution (e.g. Armitage et al., 2011) as well as a wide range of events of geomorphological significance (e.g. Tamura et al., 2012). The technique covers a considerable age range from a few years (see review by Madsen and Murray, 2009) to several hundred thousand years (e.g. Pawley et al., 2010; Stevens et al., 2018). It is typically applied to silt or sand grains extracted from sediment although more recently its potential to date solid rock surfaces has been demonstrated (Liritzis, 2011; Sohbati, 2013). Together with $^{14}$C and cosmogenic radionuclide dating, luminescence dating is now one of the major chronological tools in geology and archaeology.

During burial, naturally occurring radionuclides (U, Th and progeny, and K) in rocks or sediments expose the minerals to ionising radiation in the form of alpha, beta and gamma radiation, resulting in the trapping of charge (electrons) at defect sites in the minerals. During stimulation by heat or light, these trapped electrons are released from the defect sites and recombine at sites with an electron deficit (holes); during this energy release process luminescence is emitted and the trapped charge population (i.e. the

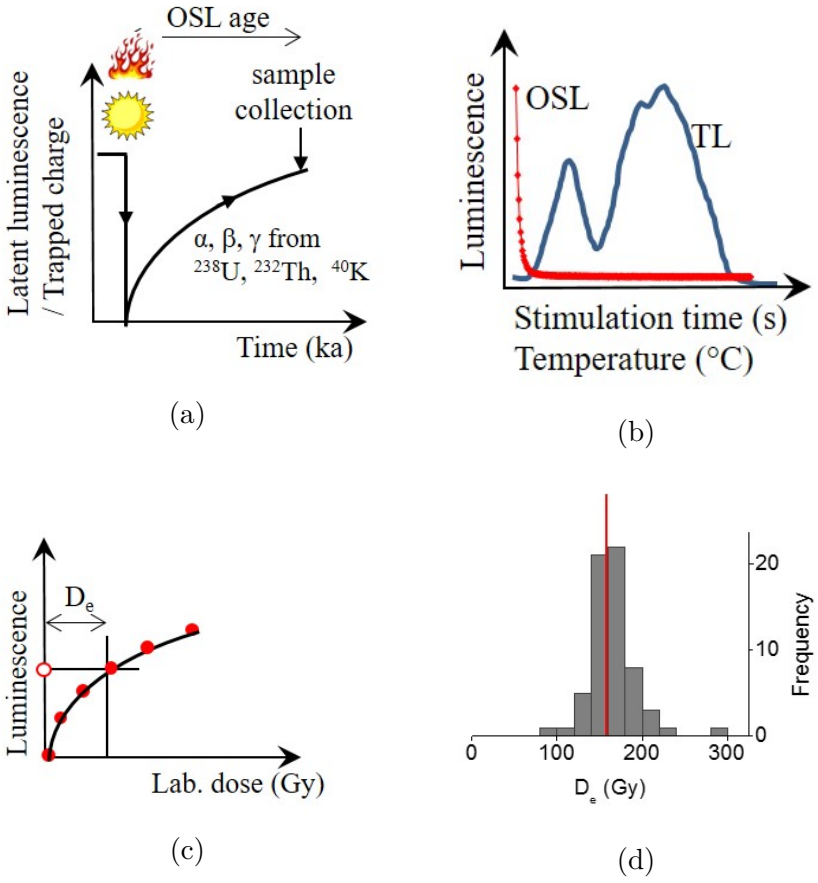


Figure 1.1: Principles behind luminescence dating. (a) Emptying of trapped charge by daylight during transport (solar resetting). After burial, natural ionising radiation ($\alpha$, $\beta$, $\gamma$) absorbed by quartz and feldspar crystals (dosimeters) causes the buildup of the natural trapped charge population. (b) After sample collection, this trapped charge is measured using an artificial light source (OSL) or heat (TL). (c) The natural signal (open symbol) is calibrated in terms of dose ($D_e$) using luminescence signals induced by known laboratory doses. (d) Repeated measurements of dose on individual subsamples containing several sand-sized grains (multi-grain) or individual quartz or feldspar grains (single-grain) yield a dose distribution. A statistical model is then used to extract the preferred $D_e$ for age calculation.

chronometric information) is reset (Aitken, 1985, 1998). During subsequent burial, minerals are shielded from light and the trapping of charge (buildup of a potential luminescence signal) starts again (Figure 1.1a). Each mineral grain contains a finite number of traps and at some point during burial time these traps become saturated with charge and there will be no further change in the trapped charge population, or in the resulting luminescence signal, with continued radiation exposure. In the laboratory, the charge trapped during burial is again released by heat or light of a certain wavelength and the resulting TL or OSL signal is measured (Figure 1.1b). This "natural" luminescence signal is calibrated in terms of dose by comparison with luminescence signals from known doses given in the laboratory (Figure 1.1c). Typically, several tens of repeated measurements of dose are made on individual subsamples (aliquots) consisting of several tens to hundreds of grains (multi-grain) or even individual grains to derive a dose distribution (Figure 1.1d). A statistical model (e.g. Galbraith et al., 1999; Galbraith and Roberts, 2012) can then be used to extract the equivalent dose ($D_e$) of interest, to be used for age calculation. This dose is related to the burial time by using the age equation:

$$t = \frac{D_e}{\dot{D}_{nat}} \tag{1.1}$$

where $t$ is the burial time and ($\dot{D}_{nat}$) is the natural dose rate in Gy/ka (dose absorbed from the environment per unit time). An accurate age estimation thus relies on accurate dose and dose rate estimations. The dose estimation can, for instance, be affected by incomplete resetting of the trapped charge population before burial (e.g. because the sample was not sufficiently exposed to light before burial). In such circumstances, it is common to date single grains of quartz or feldspar, on the grounds that this would reveal any inhomogeneity in the pre-burial bleaching (Duller, 2008) as a dose distribution skewed to unrealistically large doses. However, single grain dose/age distributions usually show a larger variability in $D_e$ values than can be explained by quantifiable measurement uncertainties, even for samples that have received sufficient light exposure during transport (Arnold and Roberts, 2009) or that were prepared under well-controlled laboratory conditions (Thomsen et al., 2005). There is considerable debate in the luminescence community as to how to separate the intrinsic (i.e. related to measurement) over-dispersion in such distributions from the extrinsic part that is related to environmental factors such as bleaching/mixing (Thomsen et al., 2016, 2017; Feathers, 2017).

Chapters 2 and 3 of this thesis contribute to the understanding of the origins of intrinsic over-dispersion in quartz single-grain dose distributions. These chapters also introduce the radiation transport modelling used in later chapters.

The process of charge trapping and luminescence production in natural minerals is not yet fully understood and relies on many assumptions (McKeever and Chen, 1997). One of these assumptions is that sand-sized grains remain electrically neutral during irradiation; i.e. at the single grain level the number of trapped electrons is equal to the number of trapped holes (e.g. Bøtter-Jensen et al., 2003). If on the other hand, this assumption is proven to be false and such a charge imbalance exists at the single grain level, it is likely to be grain specific, and so may contribute to over-dispersion. Furthermore, it is also assumed, either explicitly (Aitken, 1985, 1998) or implicitly (e.g. Bailey 2001, 2004; Adamiec et al., 2004, 2006; Pagonis et al., 2007, 2008) that the number of electron-hole pairs produced per unit dose (ionisation rate) and resulting trapped populations are identical for beta and gamma irradiations, both in nature and the laboratory. These assumptions are tested using radiation transport modelling and a series of experiments in Chapters 4 and 5 of this thesis.

Finally, exo-electrons, the direct emission of electrons from crystal surfaces, may provide a valuable tool for investigating over-dispersion and charge imbalance by probing the trapped electron populations directly. This is because exo-electron emission derives from the conduction band, and so competes directly with the recombination process during stimulation. However, no instrumentation existed for such measurements when the thesis was started. With major design contributions from others, a new exo-electron detector was developed and characterised with the ultimate goal of measuring exo-electrons at the single grain level. Unfortunately, there was insufficient time to make full use of this new instrument, but Appendix 1 describes its characteristics in detail and reports on the first measurement (to our knowledge) of exo-electrons emitted by individual sand-sized grains.

To provide a common background for interpreting the contents of this thesis, a typical energy-band model used in luminescence dosimetry is first discussed (section 1.1), the literature covering charge imbalance in insulators is reviewed (section 1.2) and a summary of recent exo-electron studies (section 1.3) presented. At the end of each section, the most important points and the relevance to this thesis are summarised. Finally, the overall aim and specific objectives of this thesis are outlined.

## 1.1 Energy-band model

When atoms form molecules, the atomic orbitals overlap. Pauli's exclusion principle states that there can only be one particle in a given quantum state, so the overlapping orbitals split into discrete orbitals with slightly different energies. In a crystal lattice containing a large number of atoms, the orbitals will split even further and have very low energy separation, effectively forming a continuum. The primary electrons involved in this process are the valence electrons, i.e. the outer and most weakly bound electrons.

A material can have an infinite number of bands, although most of these have very high energy and are thus usually of little interest in this context. Here the discussion of bands is confined to those around the Fermi energy (i.e. the theoretical energy level at thermodynamic equilibrium at which the probability of finding an electron is 50%); the band just above the Fermi level is called the conduction band and the one just below is the valence band. These bands are separated by a "forbidden" gap, called the band gap, where there are no allowed energy states; in an insulator such as quartz or feldspar, the Fermi level lies in this band gap. Natural crystals generally contain defects either as (i) empty lattice sites, (ii) occupied lattice sites which should be empty, or (iii) the integration of foreign atoms into the lattice. These defects create 'allowed' energy states within the band gap and are considered traps if they can retain either an electron (electron trap) or a hole (hole trap) (Elliot, 2000, p. 497) for some finite period of time. The width of the band gap ($E_g$) is defined as the difference between the lower edge of the conduction band ($E_c$), and the highest edge of the valence band ($E_v$); $E_g = E_c - E_v$ (Elliot, 2000, p. 314-317; Figure 1.2). For insulators (also known as dielectrics), this band gap is so large ($\sim$ 3-10 eV) that ambient temperature is not sufficient to excite an electron from the valence band into the conduction band.

Figure 1.2 shows a simple band diagram with a single electron trap and two hole traps located within the band gap. When the lattice is exposed to ionising radiation, electrons can be ionised from the valence band and moved into the conduction band if the transferred energy is larger than the band gap $E_g$ (process 1 in Figure 1.2). Generally, the average energy required for the ionisation is $\sim 4E_g$ (Wolff, 1954).

The unoccupied state left in the valence band by the electron is termed a hole. Since the most stable configuration for the crystal is a full valence band (i.e. no holes) this empty state will quickly be filled by either a de-excited electron from the conduction band, or another electron from either

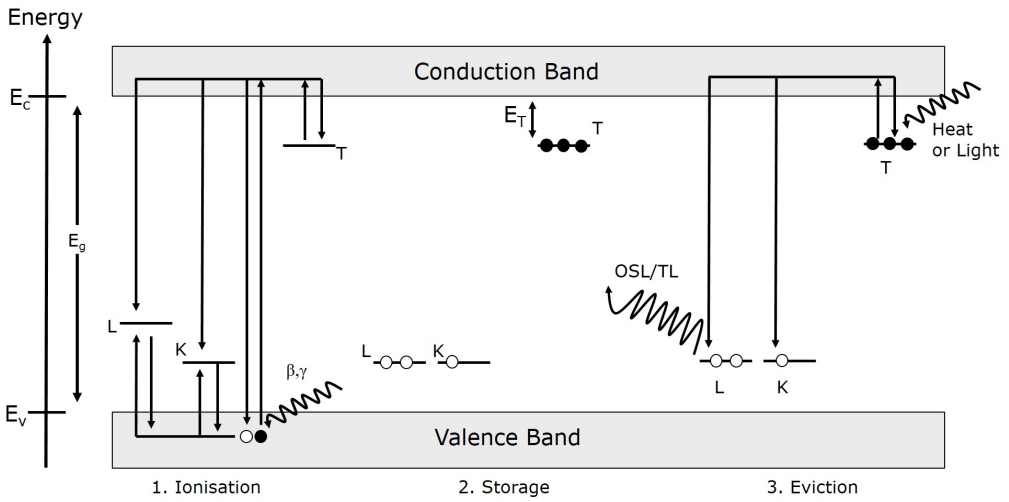


Figure 1.2: Illustration of the band model with a single electron trap (T) and two hole traps; luminescence centre (L) and non-luminescence centre (K). 1. shows the ionisation process, initiated here by $\beta$ or $\gamma$ radiation, 2. illustrates the storage of charge, and 3. charge eviction (in nature or the laboratory) by either heat or light, causing the emission of TL or OSL. $E_c$ and $E_v$ are the conduction band and valence band energies respectively, $E_g$ is the band gap energy, and $E_T$ is the trap depth of the electron trap, T.

within the valence band, or from the L or K traps (see Figure 1.2). This process can be viewed as hole hopping or migration in the valence band, until the hole is eventually trapped in a hole trap. The electrons in the conduction band can experience several competing processes. They can either de-excite and recombine with a hole in a hole trap (L or K), or they may become trapped in an electron trap, T. Direct recombination to a hole in the valence band is also possible, although this has a very low probability (McKeever, 1985 p. 34).

Storage of the trapped electrons (process 2 in Figure 1.2) is related to the stability of the electron trap, and therefore depends on the trap depth $E_T$. A shallow trap (small $E_T$) is likely to be unstable even at room temperature and is thus not suited for dating purposes. The main OSL trap in quartz is thought to be stable for $\sim 10^8$ years at room temperature (Murray and Wintle, 1999); indeed this turns out not to be a limiting factor in dating because quartz OSL dating has an upper dating limit of $\sim 150$ ka at typical dose rates due to saturation of the signal (Murray and Olley, 2002; Buylaert et al., 2007; Timar et al., 2010; Chapot et al. 2012; Timar and Wintle, 2013). For an electron to leave its trap, it must receive an energy

equal to or greater than $E_T$, this can either be supplied as heat or as light (process 3 in Figure 1.2). Once the electron has been excited from the trap into the conduction band, it may either become retrapped or recombine with a hole. The recombination can either take place at a luminescent recombination centre (L) or at a non-luminescent centre (K).

If the electron recombines at L, a photon (luminescence) will be released which can then be recorded. If the electron recombines at K, the energy will be released as lattice vibrations. From this description it is clear that luminescence does not directly measure the energy deposited in the crystal during exposure to ionising radiation. Rather, luminescence is related to the number of trapped electrons, via the recombination of these electrons with trapped holes. Only if the ionisation rate (the number of free electrons created per unit dose) is known, or can be calibrated, can this signal be correlated to the absorbed dose.

Band models are useful to visualise how charge trapping and recombination can occur during irradiation, storage and eviction as shown in Figure 1.2. Band models are very flexible and can range from simple one trap or two trap models (e.g. Bøtter-Jensen, 2003; Chen et al. 2001) to more advanced models including multiple electron and hole traps with different concentration and physical properties. Some of these more advanced luminescence models (e.g. Bailey, 2004) are used in this thesis to predict luminescence production following irradiation.

## 1.2 Charge Imbalance

Dielectrics, such as quartz and feldspar, can become charged in different ways. The most common way of charging a dielectric is through frictional or triboelectric charging. Here, charge is transferred from one object to another through frictional contact. For instance, a plastic or glass rod can be charged by rubbing it with a piece of cloth, transferring charge from the rod to the cloth leaving them both with a net but opposite charge. This charge is located on the surface of the material and can thus migrate to other objects and quite easily be neutralised. Smith (1955) studied the charge on rain drops and found that small rain drops tended to have an average positive charge which shifted to negative as the diameter increased. Similar observations of charge on dielectrics have been observed in dust storms on Earth (Kok and Renno, 2008; Gajewski and Szaynok, 1981) where frictional charging can build sufficient electrical potentials to cause discharges in the

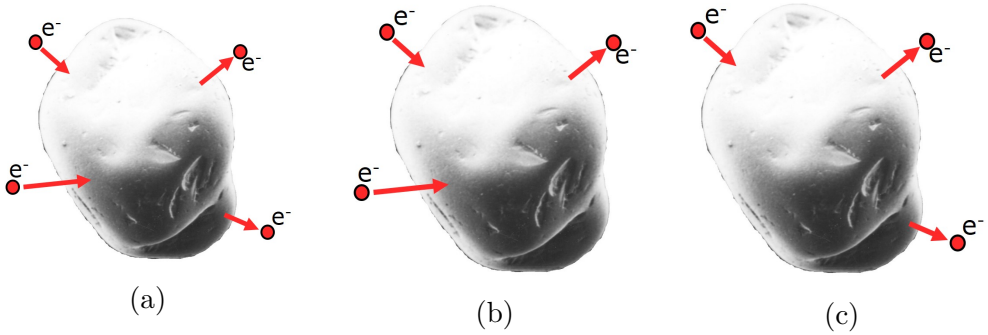


(a) (b) (c)

Figure 1.3: A charge neutral grain. Each electron entering the grain is balanced by an electron leaving. b) A negatively charged grain. There are more electrons entering the grain than leaving. c) A positively charged grain. There are more electrons leaving the grain than entering.

air. The same phenomenon is also observed in volcanic plumes where electrical storms are well documented (Mendez Harper et al., 2016; McNutt and Williams, 2010). Charging of sand-sized grains in granular flows and dust storms may also exist on Mars (Furstenau and Wilson, 2003; Melnik and Parrot, 1998) and Titan (Mendez Harper et al., 2017).

In section 1.1, the trapping of charge due to ionising radiation, and its subsequent recombination, implicitly assumed charge neutrality, i.e. the crystal was initially neutral, and remained so during charge separation and storage. Taking the system as a whole, there was an equal number of electrons and holes in total in the conduction and valence bands, and the various electron and hole traps. Since charge must enter a crystal during irradiation with e.g. alpha and beta particles, charge neutrality implicitly assumes than an equal number of charges must leave the crystal (Figure 1.3a).

However, electrons have a finite range in matter, and so this assumption cannot reflect reality. Under external irradiation with electrons of a given range, a slab of quartz which is thin compared with the electron range, will stop a different amount of the incoming electrons than a slab which is thicker than electron range. It is far more likely that the thicker slab will stop a larger number of the incoming electrons (Figure 1.3b). In this scenario, there would be more electrons available in the conduction band to undergo trapping or recombination than there are holes in the valence band. Unless the charge can easily leak from the material (including from otherwise deep electron traps) this would lead to a net excess of electrons in the grain, and the grain would build up a negative charge.

Conversely, if the material contains an internal source of radioactivity, then it is readily conceivable that more electrons would leave the material than enter it (Figure 1.3c). In this case, there would be an excess of holes available in the valence band and so the material would gain a net positive charge. Figures 1.3b and 1.3c represent situations of charge imbalance. Problems arising from excess charge on dielectrics due to ionising radiation are particularly well known in scanning electron microscopy (SEM), Auger electron microscopy (AEM), electron probe microanalysis (EPMA), electron spectroscopy chemical analysis (ESCA), secondary ion mass spectrometry (SIMS) and other analytical methods (Le Gressus et al., 1989).

### 1.2.1 Charge buildup during irradiation

Gross (1957) studied the formation of charge on borosilicate glass following irradiation with 2 MeV electrons. He observed a change in the colour of the glass, corresponding to the creation of colour centres, which extended to a depth of 0.4 cm, equal to the penetration depth of the incoming electrons. Furthermore, it was observed that electrical breakdown could be initiated by touching the sample with a pointed piece of metal. This was accompanied by a flash of light and the creation of a characteristic discharge pattern in a well-defined plane parallel to the surface leading to the point of contact. It was also observed that breakdown could be initiated several months after irradiation suggesting that the excess charge was stable. This charge could be removed by annealing to high temperatures. It is further suggested that the stored negative charge gives rise to a compensation charge at the unirradiated sample surface. This was further expanded by Gross and Wright (1959) who observed charge deposition curves in aluminium and Plexiglass following irradiation by 3 MeV electrons. These experimental curves confirmed the existence of a charged layer in the dielectric.

During irradiation, the electrostatic potential of the implanted charge can increase up to the accelerating voltage of the beam, producing reflection of the beam by the sample (Reimer, 1985; Vigouroux et al., 1986). The thickness of the implanted charge layer is equal to the penetration depth of the incident electrons. The reflection of the incident beam is due to the trapped charge population generating an electrostatic field. If the density $\rho$ is known, then the field can be evaluated using classical electrostatics. Le Gressus et al. (1989) give a detailed summary of the influence of the surrounding media on the electric field within the dielectric.

Janowski and Miller (1986) studied the effects of excess charge on dose

depth curves in PMMA and aluminium by using two different irradiation geometries; stacked sheets and a block made of two wedges. The total heights of the phantoms were sufficient to completely stop the incoming electrons. The phantoms were irradiated using 8 MeV electrons and given a nominal dose of 17 kGy. The dose was monitored using radiochromatic dye film placed between the sheets/wedges. They observed no effect due to excess charge on the dose depth curve and were able to obtain good agreement with the theoretical energy absorbed (7.8 MeV).They conclude that while the effects of accumulated charge are clearly seen in irradiated plastics it does not appear to affect the dose depth curve measurements.

### 1.2.2 Trapping of charge

Vigouroux et al. (1985) proposes that excess charge is stored at defects in crystals, potentially even defects created by the electron bombardment. Storage of excess charge at defects, they argue, is supported by the production of a mirror effect, i.e. reflection of incoming electrons, observed for various amorphous and monocrystalline $SiO_2$ samples with different concentrations of impurities. It should be noted that the impurity concentrations in these samples are likely much less than those in naturally occurring quartz and feldspar. They suggest that the electron traps responsible for the mirror charging are oxygen vacancy - peroxide linkage pairs and favour this over the Si-Si antibonding orbital. Vigouroux et al. (1985) mention that non-bridging oxygen hole centres and E'-centres function as hole traps, which is consistent with luminescence literature (Preusser et al., 2009).

Blaise and Le Gressus (1991) define two types of single-crystal oxides; (i) those that show no vacancies in their structure, such as $\alpha$-$Al_2O_3$ and MgO and (ii) $\alpha$-quartz and $Y_2O_3$ which shows vacancies. Group (i) shows a low sensitivity to irradiation damage and does not charge up negatively under electron bombardment, as long as the number of irradiation-induced defects are insignificant. Group (ii), however, is sensitive to electron irradiation and acquires a large charge during electron bombardment. On the other hand, the authors also note that polycrystalline MgO, technological alumina, or powder produced by milling, charges up very strongly. This further indicates that elementary defects, either structural or radiation induced, are important for the charging behaviour during irradiation. They observed that once the dielectric is charged, a small increase in temperature causes the charge to migrate $\sim 1$ mm without breakdown, and also concluded that electron trapping regions exist in group (ii) before irradiation occurs.

Electrons entering the material are slowed down until they quasi-thermalise,

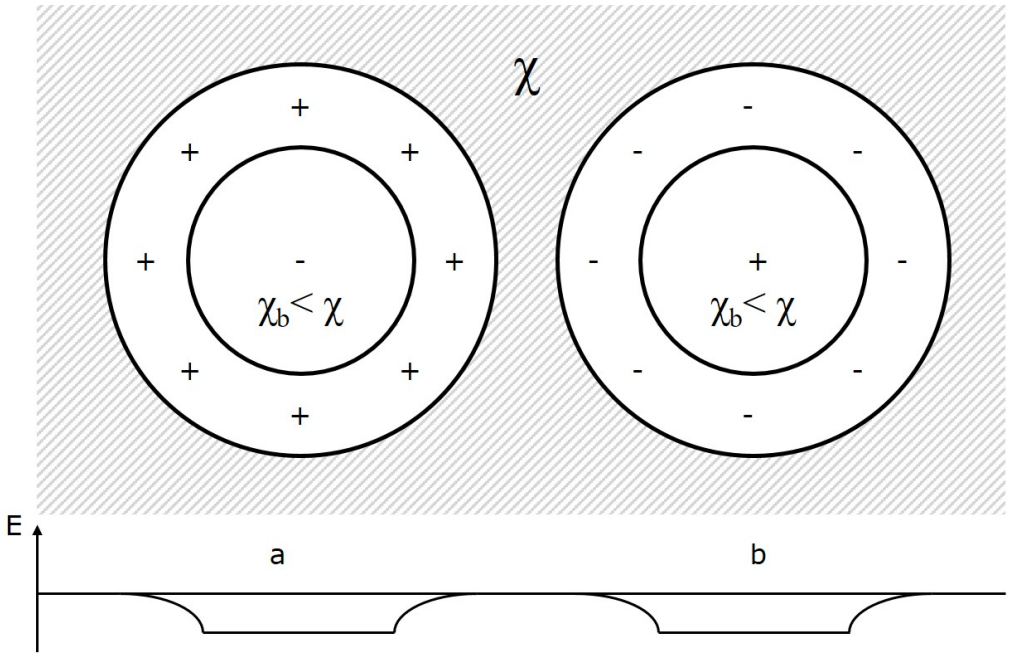


Figure 1.4: Polaron trapping as defined by Blaise and Le Gressus (1991). A bulk medium (shaded area) with smaller regions of lower susceptibility. a) Electron trapped inside a spherical region of lower susceptibility than the bulk and b) positive charge (hole) trap inside a similar region. Reproduced from Blaise and Le Gressus (1991) Figure 1.

at which point they become quasi-particles called polarons, which polarise the surrounding medium. The existence of polarons was first suggested by Landau (1933, expanded by Landau and Pekar, 1948) and refers to both an electron in a crystal lattice and the local polarisation it induces, as one particle. Blaise and Le Gressus (1991) consider the electron as sitting inside a potential well generated by the polarisation of the surrounding medium. These polarons are mobile in their own energy band either by hopping or by "conduction". As a consequence of this, migration of polarons should allow charges to flow towards a grounding potential, neutralising any net charge. But the observation that at least some of the charge is stable (see Section 1.2.1) implies that there is a trapping of polarons. Based on their model (Figure 1.4) they propose that the susceptibility of neighbouring atoms is lower than that of the surrounding medium, effectively trapping the polaron at an atomic site and stabilising it.

Blaise and Le Gressus (1991) also state that for each trapped hole there must be a corresponding trapped electron but also acknowledge that there can be an excess of charge.

### 1.2.3 Stability

The stability of charge during irradiation depends on the conductivity of the material and presumably also the presence and availability of stable trapping sites. Frederickson (2004) found that the surface voltage of glass samples, irradiated with 10 keV electrons, dropped ∼20% over a storage period of 11 days for slightly leaky glass. Non-leaky glass showed no decrease in surface voltage after 11 days. Vigouroux et al. (1985) found that the potential induced at a distance of 2 mm from the surface of $SiO_2$ could be changed if the irradiation temperature was elevated. Their data was fitted by Cazaux (1986), who found decay times of 17.7 minutes at 150 °C which dropped to ∼1.7 minutes at 240 °C. Above 300 °C there was no longer any formation of a mirror charge. The anneal temperature of the mirror charge is at about the same temperature as the E'-centres in high-OH fused silicas (Griscom, 1984), this temperature is, however, almost 100 °C lower than that listed in Preusser et al. (2009) for mineral quartz. They also found that while cleaning the sample surface by ion etching, the surface charge was reduced, but it did not reduce the bulk charge. Blaise and Le Gressus (1991) give two remarks regarding the equilibrium of the trapped polarons. Given that the repulsion between trapped polarons is weak it is possible to achieve rather high charge densities. However, the spatial gradient of the charge distribution must be kept low enough so that the resulting electric field is not strong enough to cause detrapping. Furthermore, it is the polarisation of the medium that allows the buildup of charges to relatively high densities. Without such a polarisation, the charges would disperse upon entering the material unless they were trapped in deep potential wells of several eV.

While such traps are common in luminescence dating, Blaise and Le Gressus (1991) state that it is not clear how these charges could be detrapped and moved when the external stimulation is small. Blaise et al. (2009) found an 85% loss of charge for muscovite mica irradiated with 500 eV electrons after a 5 minute storage. The mica was positively charged after the initial irradiation. They found a relaxation time of 150 s for electrons and 250 s for holes in mica, deducing that from a practical standpoint the irradiated area could be considered neutral after 15 minutes. They attribute this apparent neutrality to diffusion of charges in the sample volume until they are evacuated through contact with the metal holder. The relaxation times of mica indicate that the number of free carriers at room temperature is small, as holes are considered to have very low mobility, neutralisation only occurs through the more mobile electrons. That mica, a low conductivity material,

appears to behave like a trapping dielectric (such as MgO or single $SiO_2$ crystals) where no charge relaxation is observed, indicated that the flowing charge rate during irradiation is much less than the incoming charge rate in the experimental conditions mentioned in the article (Blaise et al., 2009).

### Summary

The literature discussed in this section describes experimental evidence which suggests that, depending on the experimental configuration, excess charge almost certainly exists and that its stability can vary greatly between different materials. While the effects of excess charge in and on dielectrics has been studied in the fields of SEM and other analytical techniques using charged particles, particularly electrons, the effects, if any, on trapped charge dosimetry (including luminescence dating) are unknown. Observations suggest that charge is held in defects, a notion shared with luminescence dosimetry (Aitken, 1985, 1998; Preusser et al., 2009), and that excess charge may also be stored at such defects. This implies that once the charge is in the conduction band it can either migrate to ground potential or become trapped at a defect.

The stability of such trapped charges is clearly important; since luminescence dating is based on electron/hole recombination, any excess charge could significantly alter the sensitivity of the sample when dealing with large accumulated doses. It is thus important to understand and predict what levels of charge imbalance may arise in nature and in the laboratory, in order to better understand the relationship between luminescence production in quartz and feldspar and absorbed dose.

## 1.3 Exo-electron emission

Exo-electron emission is the structure-dependent low energy emission of electrons from the surfaces of materials as a result of structural change. Such a change could be brought on by processes as mechanical deformation, physical phase change, chemical reaction or even exposure to ionizing radiation (Becker, 1970). After the surface-altering process has ended, some materials may show spontaneous emission of electrons decaying with time, while others may require stimulation to enable emission (Crase, 1971). If the required stimulation is heat, the electron emission is known as Thermally Stimulated Exo-Electron Emission (TSEE), while it is known as Optically Stimulated Exo-Electron Emission (OSE) if the stimulation of the surface is done using photons. For consistency, thermally stimulated exo-electrons

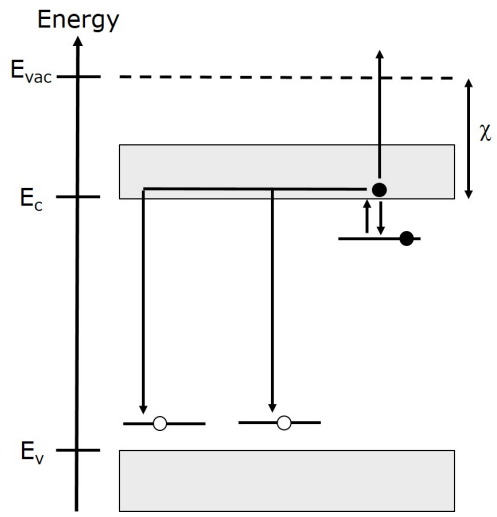


Figure 1.5: Band model showing the emission of exo-electrons. Once an electron is in the conduction band, it may escape the surface of the crystal if it is able to overcome the electron affinity, $\chi$. This process is in direct competition with the recombination responsible for luminescence production.

will be referred to here as TSE instead of TSEE. While TL and OSL are bulk phenomenon, probing the trapped charge population of the entire crystal, exo-electron emission is a surface phenomenon and as such only probes traps close to the surface, potentially only those surficial crystal cells (100 - 1500 Å, Oster et al. 1999).

Once an electron has been able to overcome the electron affinity of the insulating solid and escapes the material into the surrounding atmosphere (Figure 1.5) it will usually react readily with electrophilic species such as water vapour. The challenge in the detection of exo-electrons is to extend the period before this reaction occurs for a sufficiently long time that the electron can be detected. One solution to this is to operate the detector in vacuum or the system may be flushed with a gas that promotes ionization over electron absorption (Turner 1995).

According to Oster (1999), exo-electrons due to thermal stimulation (TSE) were first observed by Tanaka in the period 1935 to 1940. Tanaka observed the slow emission of electrons from the surfaces of metal oxides which had previously been exposed to radiation. However, it was not until Kramer (1950) that they were given the name exo-electrons. Kramer (1950, 1951) believed that the electron emission was due to exothermic processes,

now known not be the case, but the term is still used. After Kramer's initial work on the subject, the emission of exo-electrons from various materials were studied (Crase, 1971). Exo-electron emission occurs particularly from ionic crystals, such as alkali and alkali-earth halides and sulphates, other metal sulphates, metal oxides as well as numerous other materials and even some organic compounds; a comprehensive list of materials can be found in a review by article by Becker (1970). Kramer (1962) was the first to suggest that exo-electrons could be used for dosimetric purposes and previous work has primarily used artificial materials such as BeO, $Al_2O_3$, and LiF (Crase et al., 1971).

Previous TSE studies using gas counters have used a wide range of materials such as ceramics (Zastowny, 1998) and fired quartz (Zimmerman, 1971). Davies (1983a) studied powdered human enamel and enameloid from a Great White shark without any chemical or thermal treatment. Davies (1983b) used African sediments that had been chemically treated with 0.1 M hydrochloric acid and 30% hydrogen peroxide to remove carbonate and organic matter before TSE measurements. The TSE signals could be used to distinguish areas previously contaminated by elephantiasis. Sediment samples from affected areas showed a distinct peak at 75 °C not seen in samples from the unaffected areas. This appears to be the first report of TSE in applied toxicology. Ankjærgaard et al. (2006, 2008, 2009) and Tsukamoto et al. (2010) also used a gas counter and chemically cleaned quartz and feldspar extracted from sediments for their measurements.

Ankjærgaard et al. (2006) were the first to measure OSE. The exo-electron detector developed by Ankjærgaard et al. was used with an automated Risø TL/OSL reader (Bøtter-Jensen et al. 2010) and allowed simultaneous measurement of TL/OSL with TSE/OSE. This allowed the authors to construct dose response curves from OSL and OSE and to compare the behaviour of the two signals. Ankjærgaard et al. (2009) show several dose response curves for OSL/OSE; for some samples the OSE signal has a higher characteristic dose ($D_0$) than the fast component OSL signal (Singarayer and Bailey 2004; Jain et al., 2004) usually used for quartz OSL dosimetry, while for others it is lower. For two of the four samples the $D_0$ of both signals agreed. A dose recovery test (Murray, 1996) on one of these samples yielded satisfactory OSL and OSE dose recovery ratios. Furthermore, they also observed good agreement between the shapes of natural and regenerated OSE decay curves. This and other evidence allowed them to conclude that the two signals originated from the same traps. These observations show the potential of exo-electron emission as a tool for investigating and perhaps

even dating natural sediments using sand-sized quartz.

Tsukamoto et al. (2010) followed the work of Ankjærgaard et al. (2006, 2008, 2009), and investigated the time resolved OSE and OSL signals. They found that the time-resolved OSE (TR-OSE) signals from quartz and NaCl decayed much faster ($< 1\,\mu s$) than the corresponding $\sim 40\,\mu s$ for time-resolved OSL (TR-OSL). As such, they conclude that the fast decay of TR-OSL arises not from conduction band emptying but mainly from decay of excited states of recombination centres. Their work also provided constraints on the rate of charge movement in natural dosimeters.

### Summary

Exo-electron studies provide a valuable alternative to luminescence for exploring quartz and feldspar crystal behaviour because they do not rely on the recombination of trapped electrons with holes. Exo-electrons are in fact in direct competition with recombination processes and so they have the potential to be particularly useful in deciphering the relative probabilities of detrapping, retrapping and recombination processes occurring during stimulation. As such, we can in principle use the exo-electron signal as a measure of the trapped electron population in a grain without relying on TL or OSL for determining the absorbed dose.

## 1.4 Purpose, Objectives and Outline of Thesis

Given what is known about charge imbalance and its effects, we can now return to this thesis. The overall aim of the research reported here is to improve quartz luminescence dosimetry through a more solid understanding of electron trapping and recombination processes in sedimentary quartz. This can be split in two primary objectives: I) identify contributions to intrinsic over-dispersion in single-grain dose distributions from natural minerals such as quartz and feldspar, especially those arising from heterogeneity in irradiation geometry, and II) to investigate the effects charge imbalance might have on luminescence production in quartz.

This thesis aims to answer the following questions regarding intrinsic over-dispersion in apparent dose distributions observed using individual luminescent grains:

- Does grain size and shape contribute to over-dispersion?

- What effect does the backscattering material have on over-dispersion?
- Do dosimetrically similar minerals with very different luminescence characteristics experience the same laboratory dose rate?

These questions are addressed in Chapters 2 and 3, based on Autzen et al. (2017) and Hansen et al. (2018), respectively.

In published research, grains have been considered charge neutral during irradiations in nature and the laboratory. However, any imbalance in deposited charge within and between individual sand-sized quartz grains may have an effect on over-dispersion, raising the following questions:

- Does charge imbalance actually exist in sand-sized quartz grains?
- Can radiation transport modelling be used to predict this?
- What are the possible effects on luminescence production of natural minerals?

These questions are addressed in Chapters 4 (based on Autzen et al. 2018) and 5. Chapter 4 considers particularly the first two questions, and Chapter 5 builds and expands on the modelling and experimental work carried out in Chapter 4. It revisits the earlier experimental work and expands on it, and also uses radiation transport modelling output as input to luminescence modelling. The resulting predictions are then compared with the experimental observations. Finally, Chapter 6 provides a summary of the most important findings in this thesis and gives the author's view on future research directions.

# References

Adamiec, G., Garcia-Talavera, M., Bailey, R.M., Iniguez de la Torre, P., Application of a genetic algorithm to finding parameter values for numerical simulations of quartz luminescence. *Geochronometria*. 2004:**23**:9-14

Adamiec, G., Bluszcz, A., Bailey, R., Garcia-Talavera, M. Finding model parameters: genetic algorithms and the numerical modelling of quartz luminescence. *Radiation Measurements*. 2006:**41**:897-902

Aitken, M.J. *Thermoluminescence Dating* 1985 Academic Press, London

Aitken, M.J. *An Introduction to Optical Dating: The Dating of Quaternary Sediments by the Use of Photon-simulated Luminescence* 1998 Oxford University Press

Akselrod, M. S., Odegov, A. L., and Durham, J. S. Aluminium oxide exoelectron dosimetry. *Radiation Protection Dosimetry* 1994:**54(4/3)**:353-356

Ankjærgaard, C., Murray, A. S., Denby, P. M., and Bøtter-Jensen, L. Measurement of optically and thermally stimulated electron emission from natural minerals *Radiation Measurements* 2006:**41**:780-786

Ankjærgaard, C., Denby, P. M., Murray, A. S., and Jain, M. Charge movement in grains of quartz studied using exo-electron emission *Radiation Measurements* 2008:**43**:273-277

Ankjærgaard, C., Murray, A. S., Denby, P. M., and Jain, M. Using optically stimulated electrons from quartz for the estimation of natural doses. *Radiation Measurements.* 2009:**44**:232-238

Armitage, S. J., Jasim, S. A., Marks, A. E., Parker, A. G., Usik, V. I., Uerpmaan, H.-P. The Southern Route "Out of Africa": Evidence for an Early Expansion of Modern Humans into Arabia, *Science* 2011:**331(6016)**:453-456

Arnold, L.J., Roberts, R.G. Stochastic modelling of multi-grain equivalent dose ($D_e$) distributions: Implications for OSL dating of sediment mixtures *Quaternary Geochronology* 2009:**4(3)**:204-230

Bailey, R.M. Towards a general kinetic model for optically and thermally stimulated luminescence of quartz. *Radiation Measurements.* 2001:**33**:17-45

Bailey, R.M. Paper I - simulation of dose absorption in quartz over geological timescales and its implications for the precision and accuracy of optical dating. *Radiation Measurements.* 2004:**38**:299-310

Becker, K. Principles of thermally stimulated exoelectron emission (TSEE) dosimetry. *IAEA Atomic Energy Review* 1970:**8**:173-218

Becker, K. Solid State Dosimetry. 1973. CRC Press, Ohio, US.

Blaise, G., and Le Gressus, C., Charging and flashover induced by surface polarization relaxation process *Journal of Applied Physics* 1991:**69(9)**:6334-6339

Blaise, G., Pesty, F., and Garoche, P. The secondary electron emission yield of muscovite mica: Charging kinetics and current density effects *Journal of Applied Physics* 2009:**105**:034101

Buylaert, J. P., Vandenberghe, D., Murray, A. S., Huot, S., De Corte, F., Van den haute, P. Luminescence dating of old (>70 ka) Chinese loess: A comparison of single-aliquot OSL and IRSL techniques *Quaternary Geochronology* 2007:**2**:9-14

Bøtter-Jensen, L., McKeever, S.W.S, Wintle, A.G. *Optically Stimulated Luminescence Dosimetry* 2003. (Amsterdam: Elsevier) Chapter 2

Bøtter-Jensen, L., Thomsen, K. J., Jain, M. Review of optically stimulated luminescence (OSL) instrumental developments for retrospective dosimetry *Radiation Measurements* 2010:**45(3-6)**:253-257

Cazaux, J. Some considerations on the electric field induced in insulators by electron bombardment *Journal of Applied Physics* 1986:**59(5)**:1418-1430

Chapot, M. S., Roberts, H. M., Duller, G. A. T., Lai, Z. P., A comparison of natural- and laboratory-generated dose response curves for quartz optically stimulated luminescence signals from Chinese Loess *Radiation Measurements* 2012:**47**:1045-1052

Chen, R., Leung, P. L. Natural dose dependence and dose-rate dependence of optically stimulated luminescence and Thermoluminescence *Radiation Measurements* 2001:**33**:475-481

Crase, K. W., Becker, K., and Gammage, R. B. Parameters affecting the radiation-induced thermally stimulated exoelectron emission from ceramic beryllium oxide. PhD thesis, University of Tennessee, Oak Ridge National Laboratory, Tennessee

Davies, J. E. Exoemission and thermoluminescence from human enamel and shark enamleoid. *Radiation Protection Dosimetry* 1983a:**4(3/4)**:181-184

Davies, J. E., and Townsend, P. D. Exoemission of Ethiopian soils and the endemicity of non-filarial elephantiasis. *Radiation Protection Dosimetry* 1983b:**4(3/4)**:185-188

Duller, G.A.T. Single-grain optical dating of Quaternary sediments: why aliquot size matters in luminescence dating *Boreas* 2008:**37(4)**:589-612

Elliot, S.R. *The Physics and Chemistry of Solids* John Wiley & Sons Ltd, England, 2000

Feathers, J.K. A response to some unwarranted criticisms of single-grain dating: Comments on Thomsen et al. *Quaternary Geochronology* 2017:**37**:108-115

Frederickson, A. R., Dennison, J. R. Measurement of Conductivity and Charge Storage in Insulators Related to Spacecraft Charging *IEEE Transactions on Nuclear Science* 2004:**50(6)**:2284-2291

Fuerstenau, S., and Wilson, G. A particle charge spectrometer for determining the charge and size of individual dust grains on Mars *Electrostatics 2003 Proceedings of the Inst. Phys. Conf. Ser. No 178: Section 4* 2003:143-148

Gajewski, J. B., and Szaynok, A. Charge measurement of dust particles in motion, *Journal of Electrostatics* 1981:**10**:229-234

Galbraith, R., Roberts, R.G., Laslette, G. Yoshida, Olley, J. Optical dating of single and multiple grain Quartz from Jinmium Rock Shelter, Nothern Australia. Part I, experimental design and statistical models *Archaeometry* 1999:**41(2)**:339-364

Galbraith, R.F., and Roberts, R.G. Statistical aspects of equivalent dose and error calculation and display in OSL dating: An overview and some recommendations *Quaternary Geochronology* 2012:**1**:1-27

Griscom, D. L. Characterization of three E'-center variants in X- and gamma-irradiated high purity a-SiO2 *Nucl. Instrum. Methods B.* 1984:**1(2-3)**:481-488

Gross, B. Irradiation Effects in Borosilicate Glass *Physical Review* 1957:**107(2)**:368-373

Gross, B., and Wright, K. A. Charge distribution and range effects produced by 3-MeV electrons in Plexiglas and aluminum, *Physical Review* 1959:**114(3)**:725-727

Jain, M., Thomsen, K. J. Bøtter-Jensen, L., Murray, A. S. Thermal transfer and apparent-dose distributions in poorly bleached mortar samples: results from single grains and small aliquots of quartz *Radiation Measurements* 2004:**38(1)**:101-109

Janowsky, I. and Miller, A., Depth-Dose Profiles in Polymethyl Methacrylate and in Alumnium Irradiated by 8-MeV Electrons, *Appl. Radiat. Isot.* 1986:**37(12)**:1251-1252

Kok, J. F., and Renno, N. O, Electrostatics in Wind-blown sand, *Phys. Rev. Lett.* 2008:**100(1-11)**: 014501

Kramer, J. Unterschuchungen mit dem Geiger-Spitzenzähler an bearbeiten Nichtmetallen *Zeitschrift für Physik.* 1950:**128(128)**:538-545

Kramer, J. Unterschuchungen mit dem Geiger-Spitzenzähler an bestahlten Kristallen *Zeitschrift für Physik* 1951:**129(129)**:34-44

Kramer, J. Der Nachweis ionisierender Strahlung mit Exoelectronen *Zeitschrift für angewandte Physik* 1962:**15**:20-28

Landau, L. D., Über die bewegung der Elekronen in Kristallgitter *Phys. Z. Sowjetunion* 1933:**3**644-645

Landau, L. D., Pekar, S. I., Effective Mass of a Polaron *Zh. Eksp. Teor. Fiz.* 1948:**18(5)**:419-423

Le Gressus, C., Valin, F., Gautier, M., Duraud, J. P., Cazaux, J., Okuzumi, H. Charging Phenomena on Insulating Materials: Mechanisms and Applications *Scanning* 1990:**12**:203-210

Liritzis, I. Surface Dating by Luminescence: An Overview *Geochronometria* 2001:**38(3)**:292-302

Madsen, A.T., Murray, A.S. Optically stimulated luminescence dating of young sediments: A review *Geomorphology* 2009:**109**:3-16

McKeever, S.W.S. *Thermoluminescence of solids* 1985 Cambridge University Press pp 376

McKeever, S.W.S., and Chen, R., Luminescence models *Radiation Measurements* 1997:**27(5/6)**:625-661

McNutt, S. R., Williams, E. R. Volcanic lightning: global observations and constraints on source mechanisms *Bulletin of Volcanology*, 2010:**72(10)**:1153-1167

Melnik, O., Parrot, M. Electrostatic discharge in Martian dust storms, *Journal of Geophysical Research: Space Physics* 1998:**103(A12)**:29107-29117

Mendez Harper, J. S., Dufek, J. The effects of dynamics on the triboelectrification of volcanic ash *Journal of Geophysical Research: Atmospheres* 2016:**121(14)**:8209-8228

Mendez Harper, J. S., McDonalds, G. D., Dufek, J., Malaska, M. J., Burr, D. M., Hayes, A. G., McAdams, J. and Wray, J. J. Electrification of sand on Titan and its influence on sediment transport, *Nature Geoscience* 2017:**10**:260-265

Murray, A. S. Developments in optically stimulated luminescence and phototransferred thermoluminescence dating of young sediments: Application to a 2000-year sequence of flood deposits *Geochimica et Cosmochimica Acta* 1996:**60(4)**:565-576

Murray, A.S., and Olley, J.M. Precision and accuracy in the optically stimulated luminescence dating of sedimentary quartz: A status review *Geochronometria* 2002:**21**:1-16

Murray, A.S., Wintle, A.G., 1999. Isothermal decay of optically stimulated luminescence in quartz. *Radiation Measurements.* 1999: 30; 119,Äì125

Murthy, K. B. S., Sunta, C. M., Khatri, D. T., and Prasad, G. E. Energy measurement of exo-electrons. *Journal of Physics E: Sci. Instrum.* 1985:**18**:350-353

Oster, L., Yaskolko, V., and Haddad, J. Classification of exoelectron emission mechanisms *Phys. Status Solidi.* 1999:**174**:431-439

Pagonis, V., Chen, R., Wintle, A.G., Modelling thermal transfer in optically stimulated luminescence of quartz. *Journal of Physics D: Applied Physics*. 2007:**40**:998-1006

Pagonis, V., Wintle, A.G., Chen, R., Wang, X.L. A theoretical model for a new dating protocol for quartz based on thermally transferred OSL (TT-OSL). *Radiation measurements*. 2008:**43**:704-708

Preusser, F., Chithambo, M. L., Götte, T., Martini, M., Ramseyer, K., Sendezera, E. J., Susino, G. J., Wintle, A. G. Quartz as a natural luminescence dosimeter *Earth-Science Reviews* 2009:**97(1-4)**:184-214

Reimer, L. *Scanning Electron Microscopy (PW Hawkes Ed.)*. Springer, Berlin, 1985

Rocha, F. D. G., Cecatti, S. G. P., and Caldas, L. V. E., Dosimetric characterisation of Brazilian natural stones using the thermally stimulated exoelectron emission technique, *Radiation Protection Dosimetry* 2002:**1-4**:417-420

Singarayer, J. S., and Bailey, R. M. Component-resolved bleaching spectra of quartz optically stimulated luminescence: preliminary results and implications for dating *Radiation Measurements* 2004:**38**:111-118

Smith, L. G., The electric charge of rain drops, *Quarterly Journal of the Royal Meteorological Society* 1955:**81(347)**:23-47

Sohbati, R. 2013, Luminescence, Rock Surfaces. in WJ Rink & J Thompson (eds), Encyclopedia of Scientific Dating Methods. Springer. DOI: 10.1007 978-94-007-6326-5_ 83-4

Stevens, T., Buylaert, J.-P., Thiel, C., Újvári, G., Yi, S., Murray, A.S., Frechen, M., and Lu, H. Ice-volume-forced erosion of the Chinese Loess Plateau global Quaternary stratotype site, *Nature Communications* 2018:**9**:983

Stevens Kalceff, M. A., Thorogood, G. J., and Short, K. T. Charge trapping and defect segregation in quartz *Journal of Applied Physics* 1999:**86(1)**:205-208

Tamura, T., Saito. Y., Nguyen, V.L., Ta, T.K.O., Bateman, M.D., Matsumoto, D. Origin and evolution of interdistributary delta plains; insights

from Mekong River delta, *Geology* 2012:**40(4)**:303-306

Thomsen, K.J., Murray, A.S., Bøtter-Jensen, L. Sources of variability in OSL dose measurements using single grains of quartz. *Radiation Measurements.* 2005:**39(1)**:47-61

Thomsen, K.J., Murray, A.S., Buylaert, J.P., Jain, M., Hansen, J.H., Aubry, T. Testing single-grain quartz OSL methods using sediment samples with independent age control from the Bordes-Fitte rockshelter (Roches d,ÄôAbilly site, Central France) *Quaternary Geochronology* 2016:**31**:77-96

Thomsen, K.J., Murray, A.S., Buylaert, J.P., Jain, M., Hansen, J.H., Aubry, T. Reply to: "A response to some unwarranted criticisms of single-grain dating" by J.K. Feathers *Quaternary Geochronology* 2017:**37**:8-14

Timar, A., Vandenberghe, D., Panaiotu, E. C., Panaiotu, C. G., Necula, C., Cosma, C., Van den Haute, P. Optical datin of Romanian loess using fine-grained quartz *Quaternary Geochronology* 2010:**5**:143-148

Timar-Gabor, A., Wintle, A. G. On natural and laboratory generated dose response curves for quartz of different grain sizes from Romanian loess *Quaternary Geochronology* 2013:**18**:34-40

Tsukamoto, S., Murray, A., Ankjærgaard, C., Jain, M., and Lapp, T. Charge recombination processes in minerals studied using optically stimulated luminescence and time-resolved exo-electrons. *J. Phys. D: Appl. Phys.* 2010:**43**:325502

Turner, J. E. Atoms, *Radiation, and Radiation Protection* 1995. John Wiley & Sons, Inc., New York, NY, USA, 2nd edition. ISBN 0-471-59581-0

Vigouroux, J. P., Duraud J.P., Le Moel A., Le Gressus C., Griscom D.L. Electron trapping in amorphous SiO2 studied by charge buildup under electron bombardment. *Journal of Applied Physics* 1985:**57**:5139

Vigouroux, J. P., Jollet, F., Duraud, J. P, Le Gressus, C. Influence of ion implantation and gas exposure on the charge in silicon oxide created by electronic excitation. *Scanning Electron Microscopy* 1986:**4**:1311-1317

Wolff, P.A., Theory of Electron Multiplication in Silicon and Germanium. *Physical Review* 1954:**95(6)**:1415-1420

Zastawny, A., and Białoń, J. Influence of the mechanical sample treatment on the thermally stimulated exoelectron emission in aspect of the application for sample dating *Applied Radiation and Isotopes* 1998:**50**:673-676

Zimmerman, J. The radiation-induced increase of the 100 °C thermoluminescence sensitivity of fired quartz. *J. Phys. C: Solid St. Phys.* 1971:**4**:3265-3276

# Chapter 2

# The effect of backscattering on the beta dose absorbed by individual quartz grains

Autzen, M.[1], Guérin, G.[2], Murray, A.S.[3], Thomsen, K.J.[1], Buylaert, J.-P.[1,3], and Jain, M.[1]

[1] *Center for Nuclear Technologies, Technical University of Denmark, DTU Risø Campus, Denmark,*
[2] *UMR 5060 CNRS-IRAMAT-CRP2A, Université Bordeaux 3, Maison de l'archéologie, 33607 Pessac Cedex, France,*
[3] *Nordic Laboratory of Luminescence Dating, Department of Geoscience, Aarhus University, Denmark*

Published in *Radiation Measurements*

---

**Abstract:** We describe the effect on dose rates and over-dispersion (OD) of changing the spectrum of energies to which grains of various shapes and volumes are exposed during beta irradiation, either by changing the backscattering medium or attenuating the incident spectrum. Dose rates are found to increase when the atomic number of the backscattering substrate is increased (from 0.038 Gy/s on Al to 0.057 Gy/s on Pb), at the same time the dispersion due to grain shape and volume also increases slightly (9.4% on Al and 12.0% on Pb). By adding attenuators in front of the sample the net spectrum is also altered and the dispersion affected correspondingly. Our model prediction using various grain shapes and volumes are compared

with experimental observations using sieved natural grains and the resulting dose rates are in good agreement, although the dispersions cannot be realistically compared in the absence of grain shape information for the natural material. We find from modelling that dose rates (both to grains in single grain discs and to those placed on the backscattering substrates) are sensitive to changes in shape and volume. A relative range across shapes of between 10 and 21% is observed from modelling on backscattering substrates, and of 7.4% from modelling in single grain discs. We conclude that it appears to be desirable to minimise shape and volume variations in grains if over-dispersion is also to be minimised.

**Keywords:** Attenuation; Backscatter; Beta spectrum; Dose deposition; Geant4; Modelling

---

## 2.1 Introduction

Dose distributions recorded by single sand-sized grains are now widely used in the dating of sediment samples, as a means of identifying and correcting for the effects of incomplete resetting prior to deposition and post-depositional mixing. However, for well-bleached unmixed natural samples the dose dispersion is much larger than that expected from known sources of uncertainty; even grains previously given a uniform dose by $\gamma$-irradiation show such over-dispersion (OD) when the dose is measured using a beta source, with the grains supported on some substrate. The dependence of dose rate on the atomic number of the substrate material has been investigated previously using both experiments (Murray and Wintle, 1979; Ingram et al., 2001) and modelling (Greilich et al, 2008); all 3 studies found that the dose rate increased with an increase in substrate atomic number.

The dose rate also depended on the size of the sample grains; Wintle and Aitken (1977) observed a 25% lower dose rate at 4-11 µm than at ∼100 µm, this was confirmed by Armitage and Bailey (2005) although they found the dose rate difference between that of 4-11 µm and 40 µm grains to be smaller (∼12%). They also found no significant difference in dose rates for grain sizes >40 µm, observing a plateau in effective dose rates in the grain size range from 40-250 µm. Goedicke (2007) reported a sharp decrease in dose rate below a grain size of 40 µm while also observing no significant dependence for grain sizes between 40-130 µm. Above 180 µm the observed

dose rates begin to decrease as the incident beam is attenuated while passing through the grains. Similar results were reported by Mauz and Lang (2005). Fain et al. (1999) used Monte Carlo modelling to investigate the effect of grain shape on absorbed beta doses; they concluded that for grains of 200 µm diameter there is no effect.

As part of our investigation into the importance of low energy beta particles in dosimetry, in this study we consider the effect of the backscattering substrate on the dispersion of dose distributions measured using individual grains, by beta irradiating a monolayer of quartz grains on substrates of different atomic numbers (Z) varying from 13 to 82. The doses absorbed by these grains are then measured in an Al substrate (single grain disc) in the usual manner. We also investigate the effect on the observed OD of changing the incident spectrum shape using attenuators. The dependence of average dose and the contribution from backscatter as a function of Z are compared with modelling predictions based on Geant4, and the expected dispersion due to grain shape effects discussed.

## 2.2 Backscatter

### 2.2.1 Backscatter - Modelling

We have used Geant4 (Agostinelli et al., 2003; Allison et al., 2006) to model beta dose absorption in quartz grains. A short summary of the physics involved is given in SMC2 Section 2.6.1. Similar work has been undertaken by Guérin (2011) and Guérin et al. (2012, 2015). Simulations were run using Geant4 version 10.02 patch 1 on the CentOS 7 distribution, run on a VMWare workstation player 12 virtual machine, with the Penelope physics model (Salvat et al., 2001); this is well suited for the simulation of low energy particles and for electromagnetic interactions. A cut-off of 0.5 µm for the production of secondary particles was used (i.e. no particle is generated if its range is less than 0.5 µm, and the corresponding energy is instead deposited locally). This value was chosen to be less than 10% of the minimum dimension of our dose absorbers (grains).

In the model, primary particles are released individually and the release of the next particle does not occur until tracking of the previous primary and all generated secondary particles is complete. Tracking of a particle ceases when it reaches the boundaries of the world volume (at which point its energy is considered lost from the experiment) or its step size becomes

shorter than the 0.5 µm cut-off. The release of primaries from the active source layer occurs isotropically. Each simulation is run for $10^8$ primary electrons, corresponding to approximately 1/15 of a second of irradiation using a 1.5 GBq $^{90}Sr/^{90}Y$ source; this number of primaries provides us with good counting statistics (events per grain) as well as realistic computation times.

Individual geometrical components (structural, shielding and sample) are placed inside a predefined world volume otherwise filled with air and are given material properties based on user-defined elements and alloys. The irradiation geometry is constructed using the beta-source manufacturer's description (taken from Greilich et al., 2008), the characteristics of the irradiator and source flange (Dalsgaard, 2017 private communication), and a given grain geometry and substrate. The characteristic emission spectrum of the $^{90}Sr/^{90}Y$ active layer is defined as a cumulative probability distribution function (CDF) and given as input to the simulation. Beta particles were emitted with energies randomly sampled according to the Fermi model for beta spectra, modified by Behrens and Szybisz (1976). This spectrum is then modified by the source construction, the 0.125 mm thick Be window, and scattering by the flange, before arriving at the sample position. This part of the simulation is substantially the same as that undertaken by Greilich et al. (2008), and details of the irradiation geometry are given in SMC2 (Figure 2.8).

The backscattering substrates used in the model are made of materials in the range $0 \leq Z \leq 82$. One hundred quartz grains are placed on a 10x10 grid, spaced with 600 µm between adjacent centres (this is similar to the layout of grains in a standard single-grain measurement disc; Bøtter-Jensen et al., (2003) except that in our case the grains are placed on the substrate surface rather than in holes in the substrate). Each quartz grain is uniquely labelled to allow the tracking of events within individual grains. The simulations record both the total energy deposited in each grain and the energy of any electron which enters any grain, the latter with a resolution of 1 keV.

To test the dependence of dose deposition on grain shape and volume, simulations were run for 7 different sizes and shapes of quartz grains: 100 µm or 200 µm diameter spheres, cylinders with a base radius of 150 µm and a height of 5 µm or 300 µm, and a cone of base radius and height of 150 µm. For comparing shape changes, a cylinder with base radius 50 µm and a height of 66 µm, as well as a cone of base radius 50 µm and a height of 200 µm were added. The latter two are chosen to have the same volume

as the 100 µm diameter sphere; any differences in dose absorbed by these three grains types will thus arise because of shape and not volume. In contrast, dose absorption in the two spheres will be affected only by volume. In the two cylinders dose absorption will be affected by both shape and volume. Given that the backscattered spectrum should be softer than the incident spectrum, we expect to see a higher backscatter contribution to the absorbed dose in the short cylinder compared to the tall cylinder (see SMC2 Section 2.6.1,Figure 2.7). Note that all grains fit completely within the grain holes of standard single grain discs.

The simulation records the spectra as follows: the energy of an electron is recorded (1 keV bin width) only if it (a) leaves a volume which is not the backscattering material and then (b) immediately enters the backscattering substrate, i.e. when an electron originating outside the substrate takes a first step in the substrate; secondary electrons generated within the substrate are not recorded. In the case of the incident spectrum (Figure 2.1), there is no absorber (quartz grains) sitting on the substrate, and the substrate is vacuum; this gives the incident spectrum with no backscattered contribution. Backscattered spectra are recorded in a similar manner, except that a separate 200 µm thick air volume is placed directly on the substrate, covering the entire sample surface; all electrons leaving the substrate and then entering the air volume are recorded (Figure 2.1)

The energy distribution of the backscattered electron spectra (Figure 2.1a; for completeness, corresponding backscattered photon spectra and total photon and electron spectra are shown in Figures 2.9a and 2.9b, respectively) does not change substantially from substrate to substrate. In contrast the intensity does change substantially, and at low energies and high substrate Z the backscattered intensity is comparable to that of the incident spectrum. As expected, the backscattered spectrum is softer than the incident spectrum, i.e. it contains a relatively larger low energy component; this can be seen more clearly in the normalized cumulative spectra shown in Figure 2.1b (calculated by progressively summing all lower energy bins and then normalised by dividing by the total sum of all bins). It is clear that the backscattered spectrum tends towards the incident spectrum when the substrate Z increases. The dose rate to quartz grains sitting on a substrate increases with the atomic number of the substrate (Figure 2.2), and there is a pronounced dose rate dependence on grain shape/volume. The dose rates to short and tall cylinders show the most difference, and this difference becomes more pronounced with an increasing substrate Z (although the model predicts slightly lower dose rates on copper (Z=29) than on stainless steel (Z$\sim$26) for all shapes). As the substrate Z increases,

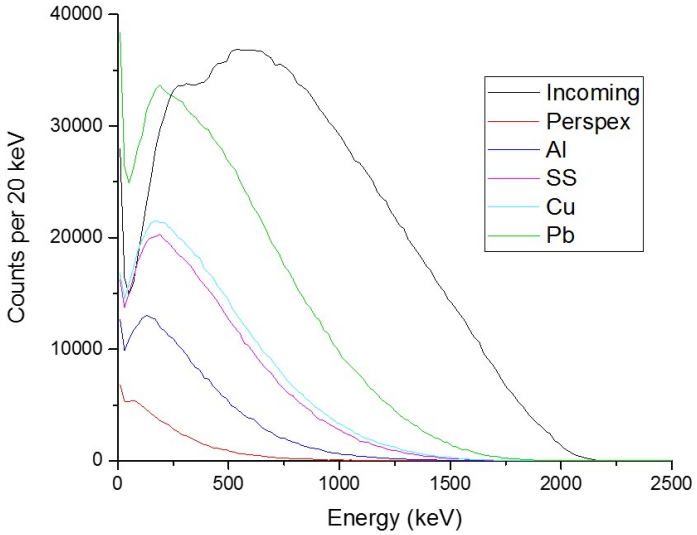


(a)

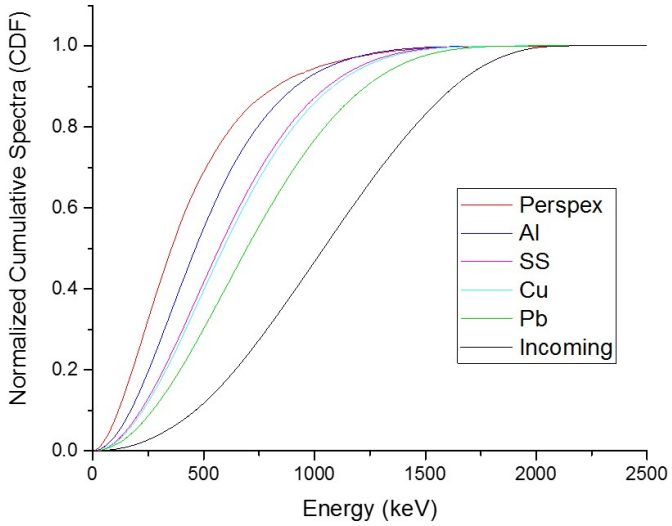


(b)

Figure 2.1: a) Incident beta spectrum on backscattering substrate and backscattered spectra from perspex, aluminium, stainless steel, copper and lead. b) Normalized cumulative distribution function spectra for each of the spectra shown in Figure 2.1a. All spectra are generated using the same number of primaries ($10^8$).

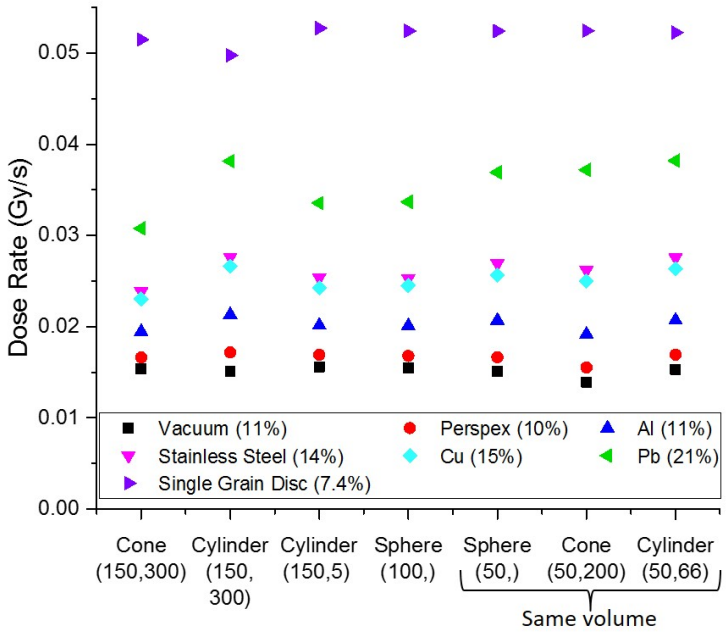


Figure 2.2: Modelled dose rates for various grain sizes and shapes on each of the modelled substrates. In the legend the numbers in parenthesis after each substrate give the relative range. The radius and height of each shape are given for each grain shape in parentheses (r, h). Single grain disc from Section 2.3.1 has been added.

the relative range with respect to the average in dose rates to the various grains shapes and volumes increases, from 11% on Al, 14% on stainless steel, 15% on copper, to 21% on lead (these data are presented graphically in Figure 2.10). Given the inevitable variation in natural grain shape, even for a tightly constrained sieve fraction, this observation suggests that we would expect to see the over-dispersion of experimentally-observed single grain dose distributions increase in a similar way. Rather surprisingly, for shapes of the same volume, the relative dose rate range decreases from 8% to 3% as the substrate Z increases from Al to Pb (see also Figure 2.10 and table 2.3). On vacuum, the largest sphere also has the largest dose rate (102% of that to the smaller sphere), this reduces as the substrate Z increases, to only 91% of the dose rate to the smaller sphere on lead. This seems to support our explanation in SMC2 Section 2.6.1 that the dose derived from the backscattered spectrum contributes more to the total dose of small grains than of large.

### 2.2.2 Backscatter - Experimental

For comparison with model predictions, quartz grains were beta irradiated in a Risø reader (TL/OSL model DA-20) with a single grain attachment. A plastic mount was placed in the reader base-plate directly under the beta-source and cups (6 mm thick, 1mm internal depth, 8 mm internal diameter) of aluminium, 316-stainless steel, copper, and lead were inserted into this support (with the turntable wheel removed) to provide the backscattering medium.

Previously sensitised sieved quartz grains (180 - 212 µm; Hansen et al., 2015) were first heated to 450$^o$C for 1 hour to thermally empty any trapped charge. The absence of apparent dose was confirmed before further exposing to the beta source. A SAR protocol (Murray and Wintle, 2000, 2003) with a 260$^o$C preheat was used for all dose measurements, and the accuracy of our chosen protocol was confirmed using a standard dose recovery experiment using single-grains (measured/given dose ratio 0.973±0.005; n=352). Undosed grains were placed loose in a monolayer in the substrate cup (i.e. without silicone oil, and not in the fixed 10x10 grid of the model), examined under a microscope to ensure a monolayer, and mounted in the reader before exposure to the beta source for 100 seconds. The grains were then loaded into standard single grain discs for measurement of absorbed dose.

The beta source employed was selected to give the smallest available spatial variation in dose rate across the sample area. Nevertheless, such variation is of significance; a contour map of the radiation intensity of our source (measured using GAF radiosensitive film according to Lapp et al., 2012) is shown in Figure 2.11. The standard deviation of source intensity across an 8 mm diameter circle (equivalent to the cup area holding the loose grains) is ∼8%. The variation in dose rate between grains in a single grain disc is ∼6%, based on the grain hole positions. We should thus expect a ∼10% variation in measured dose from grain to grain arising simply from irradiation non-uniformity, unless the correction approach of Lapp et al. (2012) is applied.

### 2.2.3 Backscatter - Experimental results and comparison with model

A total of 6 single grain discs were run for each substrate, corresponding to 600 grains per substrate. After analysis using standard rejection criteria (test dose error <10%, recycling ratio within 10% of unity), 473 grains were accepted for Al, 483 grains for Cu, 507 grains for stainless steel and 515

grains for lead.

Table 2.1: Experimental results for irradiation on various substrates and subsequent measurement in single grain discs. Doses are calculated using average dose rate to the single grain disc derived using Risø calibration quartz (Hansen et al., 2015). Correction for source heterogeneity was carried out following Lapp et al. (2012). Over-dispersion (OD) is calculated using CAM (Galbraith et al., 1999)

| Substrate | No Correction | | Correction | |
|---|---|---|---|---|
| | Measured Avg. Dose (Gy) ± se | Rel. OD (%) ± se | Measured Avg. Dose (Gy) ± se | Rel. OD (%) ± se |
| Al | 3.85±0.03 | 12.5±0.5 | 3.85±0.02 | 9.4±0.5 |
| Stainless Steel | 4.41±0.03 | 13.1±0.5 | 4.42±0.02 | 10.3±0.4 |
| Cu | 4.71±0.03 | 13.7±0.5 | 4.72±0.03 | 11.4±0.5 |
| Pb | 5.77±0.04 | 14.0±0.5 | 5.79±0.03 | 12.0±0.5 |

The grain-to-grain OD in dose rate increases slightly with Z, but any effect is masked by the variation resulting from source non-uniformity (Table 2.1). The component derived from regenerative irradiations in single grain discs (the 6% discussed above) can be removed using the source correction option (Lapp et al., 2012). This should reduce the OD resulting purely from source non-uniformity to about 8% (instead of the expected total of ∼10% if no correction is applied). Because we cannot constrain the exact position of each grain on the existing design of substrate irradiation geometry, further reduction in OD arising from source non-uniformity can only be achieved by making single grain discs of the various substrate materials and holders to ensure the irradiation geometries are beta thick. This is challenging, and the feasibility is now being investigated.

After correcting for source non-uniformity during irradiation in single grain aluminium discs the calculated OD is indeed reduced (Table 2.1) without significantly changing the mean dose rates. On average the effect of correcting for source non-uniformity is to reduce the OD by 7.8% (contributions summed in quadrature); this is consistent with the expected correction from Figure 2.11. The ODs still tend to increase with increasing Z. From Figure 2.3a it can be seen that the ratio of the modelled dose rates on different substrates to those modelled for single grain disc irradiations (see Section 2.3.1) are generally consistent with the corresponding experimental dose rate ratios as the substrate Z increases. For aluminium, the model

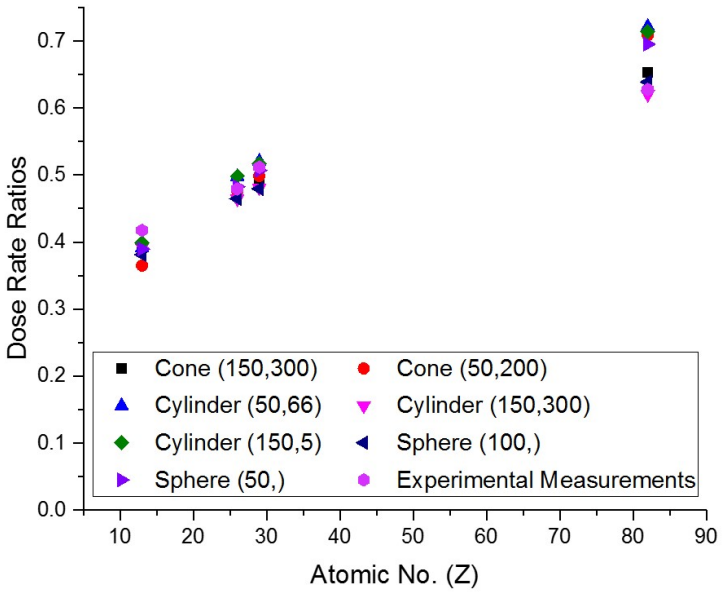


(a)

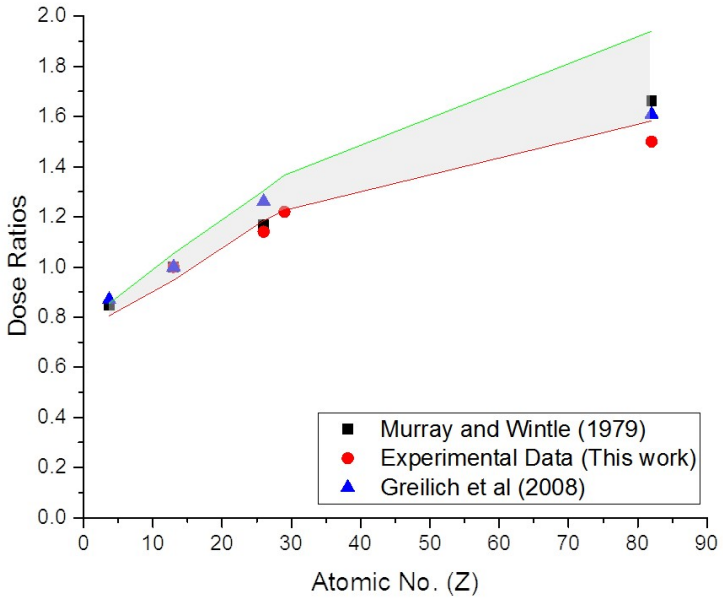


(b)

Figure 2.3: (a) Comparison of modelled dose rate ratio between substrate and single grain disc and the same ratio for experimental data. (b) Model and experimental results compared with other studies. Dose rates normalized to irradiation on aluminium, and plotted against substrate atomic number; the grey band represents the range of our modelled data.

seems to have underestimated the dose rate ratio compared with the experiment while for lead, model and experiments are in agreement. Model and experimental results (normalised to irradiation on an Al substrate) are shown together with the corresponding ratios obtained from Murray and Wintle (1979) and Greilich et al. (2008) in Figure 2.3b. Note that Murray and Wintle's (1979) experiment used 100 µm diameter CaF2 grains (modelled results within 1% of those of quartz) and the Z=27 result is for a 0.5 mm nichrome heater plate, which is not beta-thick. The observations are broadly consistent with the range of the modelled data for different grain shapes (Figure 2.3b).

Interestingly Murray and Wintle's (1979) experimental results appear to be most consistent with the model results, while our experimental data appear to be systematically lower than the model predictions for high Z. Since our data have been normalized to aluminium this can likely be explained by the fact that the dose rate ratio for aluminium was experimentally higher than that predicted by the model (Figure 2.3a). This would lead to ratios being underestimated when comparing experiments and model. The 100 µm diameter CaF2 spheres of Greilich et al.'s model results appear to be consistent with our model results as well as the experimental data of Murray and Wintle (1979).

## 2.3 Attenuation of the incident beta-spectrum

### 2.3.1 Attenuation - Modelling

Another approach to investigating the importance of the spectrum shape is to irradiate on a fixed substrate, but to attenuate the incident spectrum through an absorber and so modify the energy distribution. This also has the advantage of fixing the grain location during all irradiations, and so allowing us to remove the effects of source non-uniformity more completely. In our Geant4 simulation, the attenuator was added immediately below the Be window, and the grains were mounted in a standard Al single-grain disc (Figure 2.12).

It is clearly important that the attenuated dose rate should be large enough to give practical irradiation times, and at the same time the attenuator must be thick enough to significantly change the spectrum shape (the maximum practical attenuator thickness in the reader is 0.5 mm). As a result, our

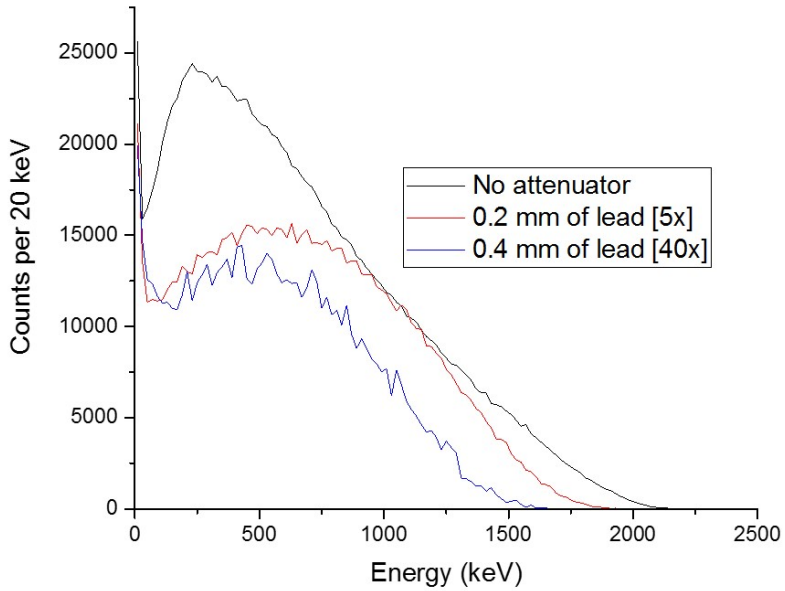


Figure 2.4: Spectrum with no attenuation, attenuation with 0.2 mm of lead and attenuation with 0.4 mm of lead for an Al single grain disc. All spectra were generated using the same number of primaries ($10^8$). Numbers in square brackets indicate the factor by which the entries have been multiplied to achieve the same scale.

simulation used three different attenuators; 0, 0.2 and 0.4 mm of lead; the resulting spectra are summarised in Figure 2.4. These spectra are recorded in a similar manner to those described above (Section 2.2.1) but now all electrons entering the holes in the single grain disc for the first time from all directions are recorded, without any grains present (corresponding photon and total spectra are shown in Figures 2.13a and 2.13b, respectively).

Based on the model predictions, the dose rate attenuations are 0, 87.9±2.5% and 98.9±0.3% for 0, 0.2 mm and 0.4 mm of lead, respectively. As expected, attenuating the beta spectrum with different thicknesses of lead not only varies the intensity but also alters the energy spectrum of particles entering the grains. The normalized cumulative spectra are shown in Figure 2.5, where it can be seen that 0.2 mm of lead hardens the spectrum up to $\sim$ 0.8 MeV after which the spectrum softens compared with the unattenuated spectrum. In contrast, 0.4 mm of lead softens the spectrum across the entire energy range. For comparison, Figure 2.5 also shows the incident spectrum

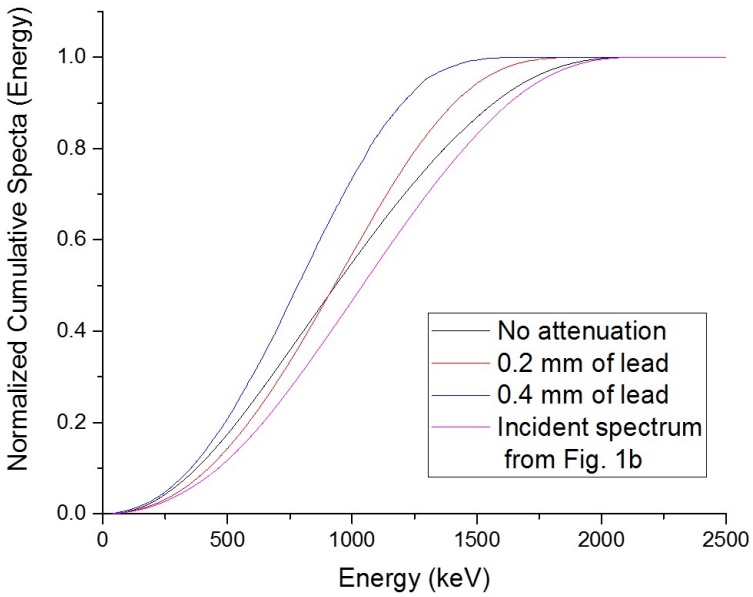


Figure 2.5: Normalized cumulative spectra for each of the spectra shown in Figure 2.4.

from Figure 2.1b; note the difference compared to the unattenuated spectrum, presumably due to presence of the walls of the single grain holes. Figure 2.6 presents the dose rate variation with grain size and shape. The unattenuated spectrum gives rise to a relative range of 7.4% compared to the average dose rate because of variations in grain shape/volume. This relative range increases to 11% when the spectrum is attenuated through 0.2 mm of lead and to 20% when attenuated through 0.4 mm of lead. Considering only the grains with the same volume, the relative range in the dose rates from the unattenuated spectrum is only 1%. This increases slightly to 2% when the spectrum is attenuated through 0.2 mm of lead, and up to 20% when attenuated through 0.4 mm of lead. Thus, a change in shape without a change in volume appears to make the grain significantly more sensitive to the shape of the attenuated spectrum. For the same shape but different volumes, i.e. the spheres, the relative range in dose rates increases from 0.7% for the unattenuated spectrum, to 3.8% for 0.2 mm of lead, and finally to 9.9% for 0.4 mm of lead. Thus, a change in volume but not shape also appears to make the grains significantly more sensitive to a change in spectrum, although not to the extent of the change in shape.

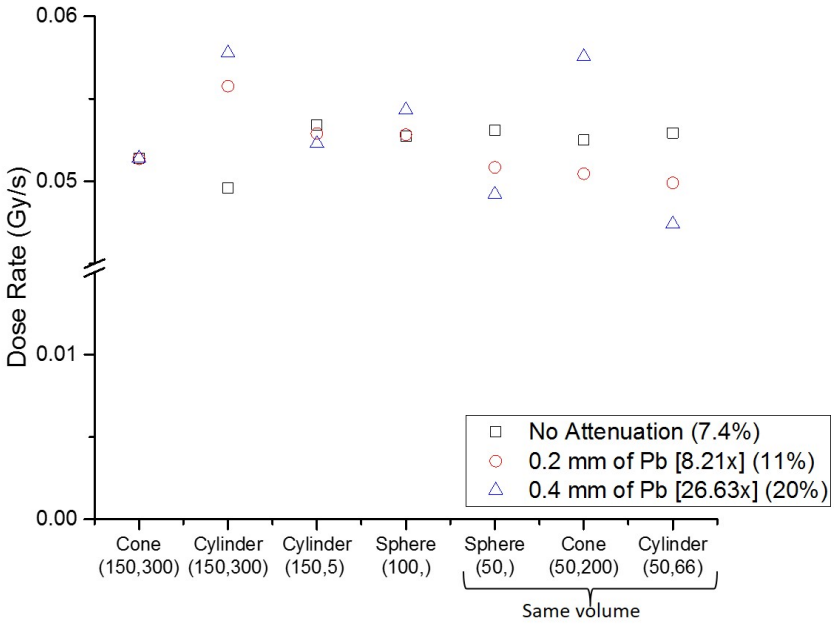


Figure 2.6: Modelled dose rates for no attenuation, 0.2 mm of lead attenuator, 0.4 mm of lead attenuator. Numbers in parenthesis note the relative range, while numbers in square brackets indicate the factor by which each entry has been multiplied.

It is also interesting to compare the 7.4% relative range in dose rates when irradiating grains mounted in holes in the single grain Al disc, with the 11% relative range (Section 2.2.1) when irradiating on Al without grain holes. It appears that the single-grain disc, primarily designed to hold the grains on a regular array, also serves to reduce the range in grain-to-grain variation in dose rates by ∼8% compared to irradiation on a planar surface (dispersion summed in quadrature).

### 2.3.2 Attenuation - Experimental

An experiment was designed to test the above model predictions using annealed grains (180-212 µm) loaded into 4 sets of 6 single grain discs (100 grains per single grain disc) with grains irradiated as follows:

- Gamma irradiation of loose grains before loading into single grain discs, gamma dose 4.81 Gy from a $^{137}$Cs source, with build up to give uniform dose deposition (see Hansen et al. (2015) for details).

- Beta irradiation in single grain disc for 55 s, no attenuation.
- Beta irradiation in single grain disc for 586 s through 0.2 mm of lead.
- Beta irradiation in single grain disc for 5095 s through 0.4 mm of lead.

The thickness of the lead foil used for attenuation (supplied by Goodfellow) is known to within ±10%. The irradiation times for the attenuated spectra were intended to deliver approximately the same dose as the 55 s of unattenuated irradiation but are based on a preliminary version of the model (not presented). Based on the predicted attenuation factors given in the previous section, these attenuated spectra irradiation times actually correspond to ∼71 s and ∼56 s of unattenuated irradiation, respectively.

The doses given by these irradiations were then measured in the usual manner using our standard SAR protocol and the unattenuated spectrum from the beta source.

### 2.3.3 Attenuation - Experimental results and comparison with model

The results of the experimental measurements are summarised in Table 2.2. For gamma irradiated sample 490 grains were accepted, 352 grains were accepted for no beta attenuation, 526 grains for attenuation with 0.2 mm of lead, and 531 grains for attenuation with 0.4 mm of lead, all using the same rejection criteria as for backscatter (Section 2.2.3). A typical single grain gamma dose distribution for this material can be found in Fig. 6b of Hansen et al. (2015). Attenuating the beta spectrum using 0.2 mm of lead gives an attenuation factor of 83±1.8% (c.f. 87.9±2.5% from the model). For the 0.4 mm lead attenuator the measured attenuation is 98.6±1.4% (c.f. 98.9±0.3% from the model). These results are consistent with the model predictions. The ODs resulting from irradiation using the gamma source and unattenuated beta spectrum (9.9±0.4% and 5.8±0.4%, respectively) are similar to values reported before (Thomsen et al., 2005; Hansen et al., 2015) - Thomsen et al. (2005) reported 8.6±0.2% for gamma dose recovery and 5.9±0.1% for beta dose recovery. Despite the relative similarity in the given doses, the OD clearly increases when the spectrum is attenuated; this is consistent with the marked change in spectrum shape towards low energies in the attenuated spectra (Figure 2.5). There is an apparent decrease in OD for 0.4 mm compared to 0.2 mm (10.8±0.4% to 12.1±0.5%); if this is real, it is unexpected, and needs further investigation.

Table 2.2: Experimental results for different thickness of Pb attenuators mounted in front of the beta source. Over-dispersion (OD) is calculated using CAM (Galbraith et al., 1999)

| | Attenuation ± se | Relative OD (%) ± se |
|---|---|---|
| Gamma dose recovery | - | 9.9±0.4 |
| Beta dose recovery | | |
| No attenuation | 0 | 5.8±0.4 |
| 0.2 mm Pb | 83.0±1.8% | 12.6±0.5 |
| 0.4 mm Pb | 98.6±1.4% | 10.8±0.4 |

## 2.4 Discussion

Modelling predicts that the dose deposited in grains should vary significantly with grain size and shape and that this effect should become more pronounced with higher substrate Z; in contrast, when the volume is kept constant across different shapes, an increase in substrate Z reduces the relative range in deposited dose. Nevertheless, the net effect is that the relative range in dose rates increases with substrate Z, from 10% on Al to 21% on lead (Figure 2.2). Our modelling data are in contrast with the modelling results of Fain et al. (1999) who did not observe a significant difference in beta dose absorption between different grain shapes. Not surprisingly, the net dose rate to larger grains is less sensitive to changes in substrate than that to smaller grains (see Section 2.2.1 and Table 2.3 in SMC2), with the largest grains experiencing an increase in dose rate between 100-118% when comparing lead to vacuum, whereas small grains experience an increase in dose rate between 144-167% for the same substrate changes. Experimentally we observe that the dose rate ratios (normalised to Al) for the smaller 90-112 µm CaF2 grains of Murray and Wintle (1979) are consistent with model predictions, both ours and those of Greilich et al. (2008). However our experimental dose rate ratios are systematically lower than model predictions; this is likely to be because our experimental dose rate ratio of aluminium/single grain disc is experimentally higher than model predictions. As each subsequent data point is normalized to this ratio this will lead to a systematic underestimation when comparing experiment and model. In real materials of mixed grain sizes and shapes, this shape/volume dependence should result in higher grain-to-grain dose dispersion, especially when dosing on heavier substrates. Although the OD data (Table 2.1) are

probably dominated by the source non-uniformity, the OD nevertheless increases with substrate Z, supporting the model predictions.

Turning now to the attenuation experiment, as expected, the model predicts a significant softening of the spectrum as it is attenuated; this attenuation and scattering will also effectively smooth out the effects of source non-uniformity (although this has not been explicitly modelled). As a result, we can now be confident that the observed ODs in the attenuation experiments reflect only the effects of the changes in incident spectrum. The OD does increase significantly with the first increase in attenuation (from 0 to 0.2 mm) but we do not see a marked increase in OD for an attenuator thickness of 0.4 mm. This is currently not understood. We hypothesize that this could be connected with softening of the incident spectrum by the 0.4 mm of lead, whereas the 0.2 mm of lead initially hardens the spectrum (Figure 2.5).

Finally, it is interesting to consider the implications of the backscattered modelling results for the well-established difference in OD between gamma and beta dose recovery experiments (e.g. Thomsen et al., 2005). Typical beta dose recovery experiments give ODs in measured/given dose ratios of 6-7%. If we now accept the modelling prediction of a $\sim$8% relative range in beta dose rates arising from grain shape/volume effects, this suggests a gamma OD of about 11%, consistent with experimental observations.

## 2.5 Conclusion

From the modelling of backscattering, we have shown that the OD increases with increased softening of the net spectrum (i.e. increasing substrate Z). Experimental results confirmed this trend. Modelling results also show that the effect of the backscattered material will vary with grain size/shape. The attenuation experiment showed that the OD was generally increased by attenuating the spectrum, with the 0.2 mm of lead leading to the largest OD. Surprisingly, further attenuation using 0.4 mm of lead gives the same or possibly smaller OD. This could be connected with the softening of the incident spectrum by the 0.4 mm of lead, whereas the 0.2 mm of lead initially hardens the spectrum. We conclude that there are good reasons to expect that grain shape and size will contribute significantly to the OD in measured single grain dose distributions, and that we can use Geant4 to simulate this dependence. It appears likely that shape/size variations in quartz or feldspar grains used for measurement should be minimised to

reduce the OD in both dose recovery and natural dose distributions.

**Acknowledgements:**

M.A. and J.-P.B. receive funding from the European Research Council (ERC) under the European Union's Horizon 2020 research and innovation programme ERC-2014-StG 639904 - RELOS. We would also like to thank Louise M. Helsted for help with experiments and samples and Vicki Hansen for providing samples.

## 2.6 Supplementary Material for Chapter 2

### 2.6.1 Theory of backscattering

When electrons impact on a material they can undergo scattering, straggling and absorption. All of these effects can result in the electron depositing energy in the material as kinetic energy is lost, assuming collisions are not purely elastic.
An electron passing near an atomic nucleus with charge $Ze$ and mass $M$, will be subjected to coulomb forces and produce a net deflection $\vartheta$ (any deflection angle between $\pi/2 < \vartheta < 3\pi/2$ is considered backscatter). Rutherford derived the differential cross-section for scattering as:

$$d\sigma = \pi Z^2 \left(\frac{e^2}{m_0 c^2}\right)^2 \left(\frac{1-\beta^2}{\beta^4}\right) \frac{\cos(\vartheta/2)}{\sin^3(\vartheta/2)} d\vartheta \tag{2.1}$$

which is valid when $2Z/137\beta \gg 1$ (i.e. slow moving electrons), where $\beta = v/c$, $Z$ is the atomic number and $e = \sqrt{1.439\text{MeV fm}}$ (Rutherford, 1911; adapted from Evans, 1955). These electrons are scattered into an element of solid angle given by

$$d\omega = 2\pi \sin\vartheta d\vartheta = 4\pi \sin\frac{\vartheta}{2}\cos\frac{\vartheta}{2} d\vartheta \tag{2.2}$$

Thus, we can write the classical differential cross section , $\xi_0(\vartheta)d\omega$ for elastic nuclear scattering of electrons in the solid angle $d\omega$, at a mean angle of $\vartheta$ as

$$\xi_0(\vartheta)d\omega = \frac{Z^2}{4}\left(\frac{e^2}{m_0 c^2}\right)^2 \left(\frac{1-\beta^2}{\beta^4}\right) \frac{1}{\sin^4\left(\frac{\vartheta}{2}\right)} \tag{2.3}$$

If $2Z/137\beta \ll 1$, relativistic effects modify this picture to give the Mott scattering cross-section:

$$\xi_0(\vartheta)d\omega = \xi_0(\vartheta)\left[1 - \beta^2 \sin^2\frac{\vartheta}{2} + \pi\beta\frac{Z}{137}\left(1 - \sin\frac{\vartheta}{2}\right)\sin\frac{\vartheta}{2}\right]d\omega \qquad (2.4)$$

valid for $\beta \approx 1$ when $Z/137 \leq 0.2$ (Mott, 1935; adapted from Evans, 1985). Thus the Rutherford differential cross section, $\xi_0(\vartheta)d\omega$, is substantially correct when the deflection angles $\vartheta$ are small. For larger deflection angles (relevant to the backscatter problem), the Mott scattering cross section will be valid for electrons moving with relativistic speeds when colliding with materials of $Z \leq 27$ (any element up to and including Co). The energy of the electrons emitted by a beta-source is given by the relativistic kinetic energy

$$E_{kin} = m_0c^2\left[\frac{1}{\sqrt{1-\beta^2}} - 1\right] \qquad (2.5)$$

where, $m_0$ is the rest mass of the particle, here we use $m_0 = 0.511\text{MeV}/c^2$ which is the electron rest mass (Einstein, 1907). Using Equation (2.3) it is possible to calculate the $\beta$ parameter for a given electron kinetic energy. This tells us that Equation (2.2) is only valid when the kinetic energy of the electron is $E_{kin} \geqslant 1.12\text{MeV}$ . A $^{90}Sr/^{90}Y$ source has a maximum emission energy of 2.28 MeV, meaning that for modelling a beta source of the type used in a Risø TL/OSL reader, there will be electrons with energies above this threshold value.

Because of these deflections and ionization events within the material, electrons will lose energy as they pass through the material, this can even lead to the generation of secondary electrons which will undergo the same processes.

Therefore, any spectrum of electron energies incident on the material will be attenuated and lose some high energy components when recorded on the opposite side of the material, this is referred to as a softening of the spectrum. As the electrons lose energy through various processes, their cross section will increase, per equation Equation (2.1), because the term $(1-\beta^2)/\beta^4$ will increase inversely proportional to $\beta^4$. Scattering will then be most likely for low energy electrons and decrease as their energy increases. However, backscattering will only be a small percentage of the total number of scattering events due to the factor of $1/\sin^4(\vartheta/2)$ and these electrons will have a lower energy than the incident electrons due to the energy loss in the scattering process.

Because of these effects, larger grains will experience a more spatially varied energy deposition, compared with smaller grains, as there will be more attenuation due to the length of the grain, this non-uniformity in energy deposition means that larger grains will have a smaller amount of deposited energy per unit mass. So we expect that the beta dose rate to grains sitting on a substrate will depend on both substrate material and grain shape/volume. This is illustrated schematically in Figure 2.7 using a thin and thick grain.

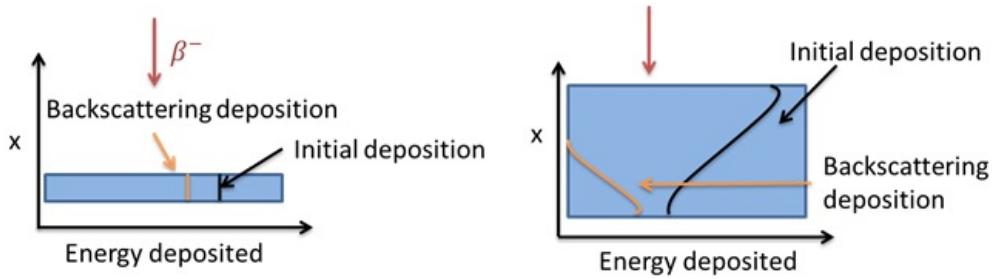


Figure 2.7: Schematic showing the dose distribution resulting from the incident and backscattered spectrum for grains of different thickness

Figure 2.7 shows the initial build-up of energy in a large grain which is attenuated as the electron penetrates deeper and deeper into the grain. Because of this attenuation the backscattered energy deposition is also much less than the initial deposition. In the thin grain there is virtually no attenuation of energy across the grain and as such there is a more uniform deposition of energy; furthermore the backscattered energy deposition is much closer to the initial deposition than for the larger grain.

As there is relatively more attenuation of the incident beam energy and flux in a thick grain compared to a thin grain, there will be a significant difference in deposited dose between the two grains. Specifically, the incident electrons across the sample-substrate interface will on average have significantly lower energy in case of the thick sample than in the thin sample (assuming that their primary input spectra are identical).

Since the scattering cross section increases with decreasing electron energy, there will be a relatively higher ratio of backscattered electron per incident electron at the interface in the case of the thick sample (because of the larger attenuation) compared with the thin sample; hence the relative contribution of the backscattered dose to incident dose closer to the substrate will be greater in case of the thick sample. On the other hand

because of the significantly greater attenuation of incident energy in the thick sample, by the time it reaches the substrate the overall contribution of the backscatter dose will be smaller when compared to the thin sample. Thus we can reasonably expect that the overall laboratory beta dose rates will vary from grain to grain, because of grain size/shape differences, and that the size of these variations will be dependent on sample substrate.

### 2.6.2 Schematic diagrams and results

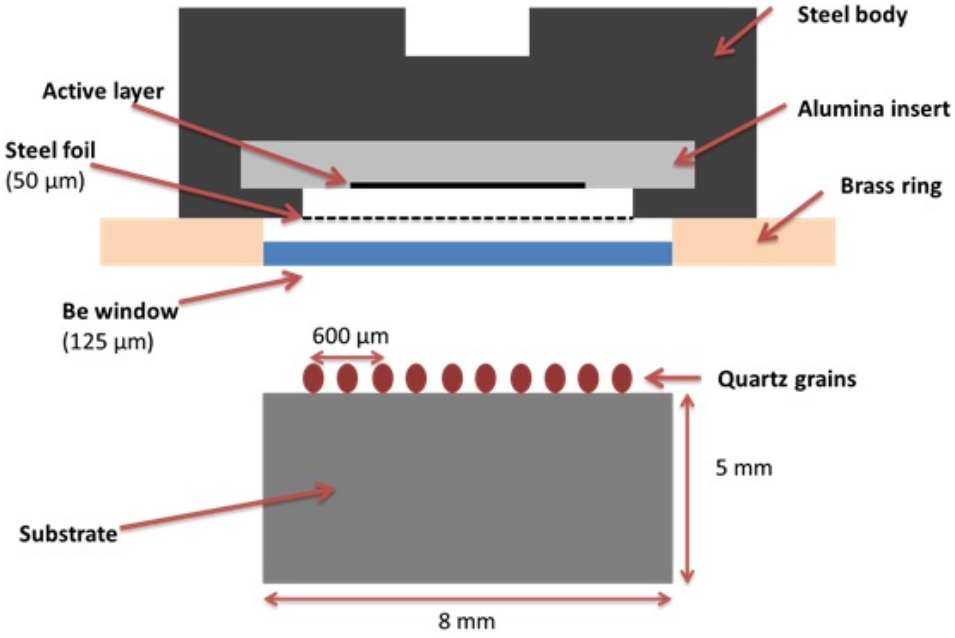


Figure 2.8: Irradiation geometry used for the Geant4 backscatter simulations using different substrate materials (perspex, aluminium, stainless steel, copper and lead).

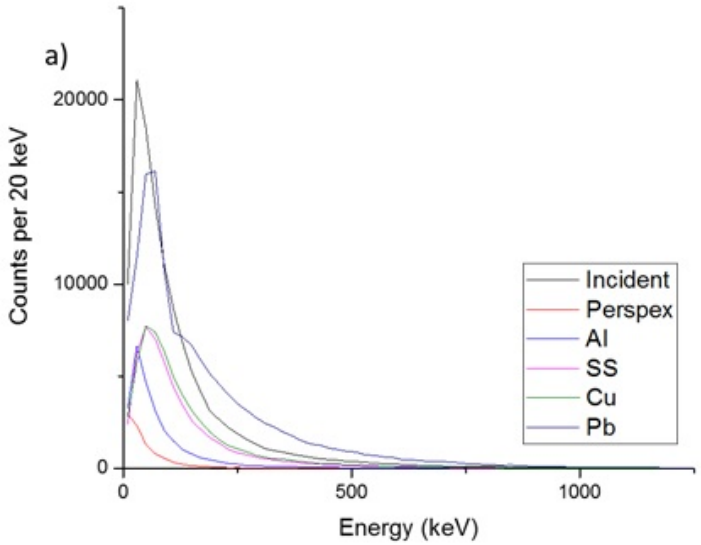


(a)

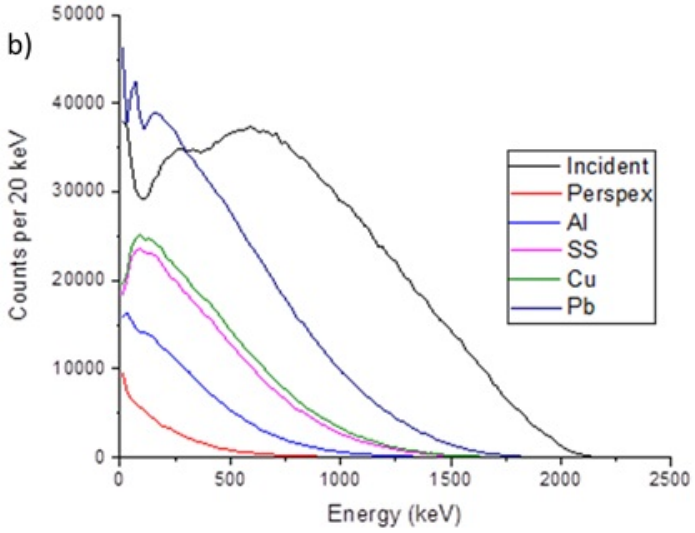


(b)

Figure 2.9: Corresponding backscattered photon spectra (a) and total photon and electron backscattered spectra (b) for the backscattered beta spectra shown in Figure 2.1 in the main text.

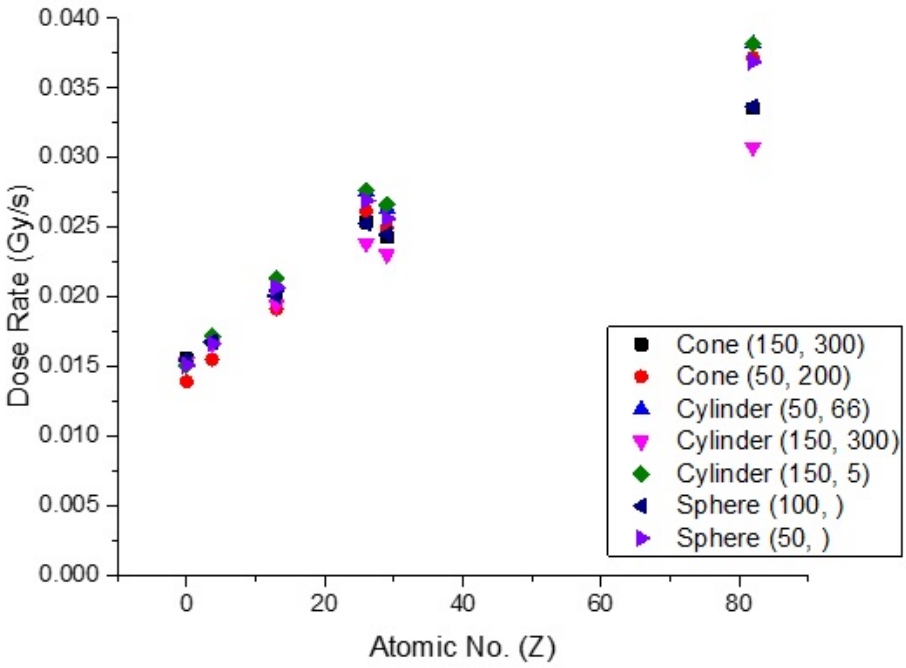


Figure 2.10: Modelled dose rates as a function of substrate Z. Note the drop between stainless steel and copper. There is a marked increase in spread as the Z of the substrate increases. Radius and height of the grain geometries are given as (r,h)

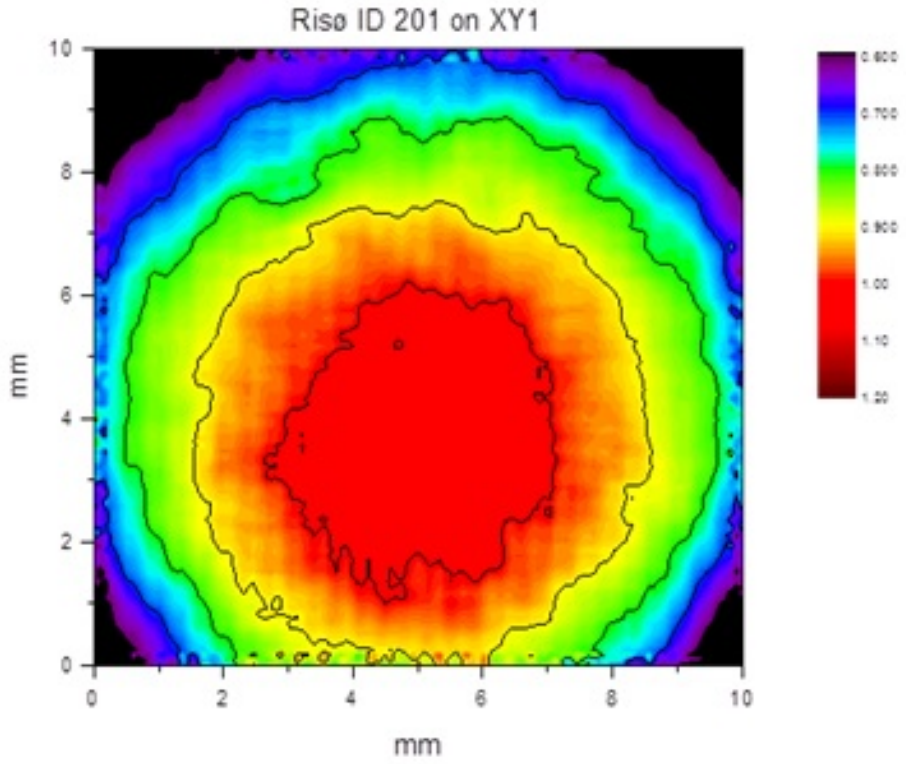


Figure 2.11: Contour map of beta source intensity of source Risø ID 201 used in this study measured using GAF radiosensitive film (Lapp et al., 2012).

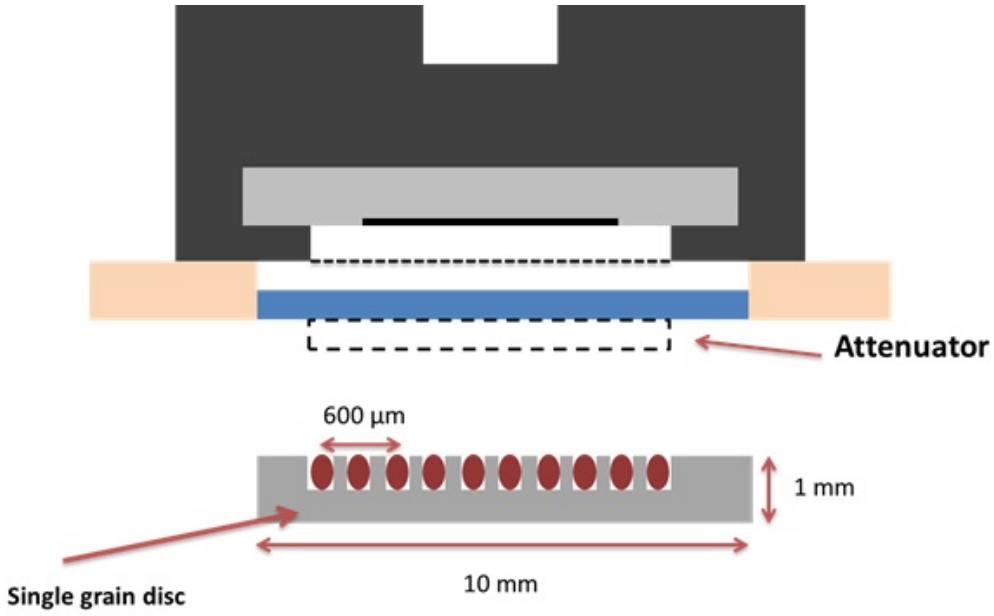


Figure 2.12: Irradiation geometry used in Geant4 simulation of attenuation using Pb attenuators of different thicknesses (0.2 and 0.4 mm). See Figure 2.8 for labeling of the different parts of the beta source unit.

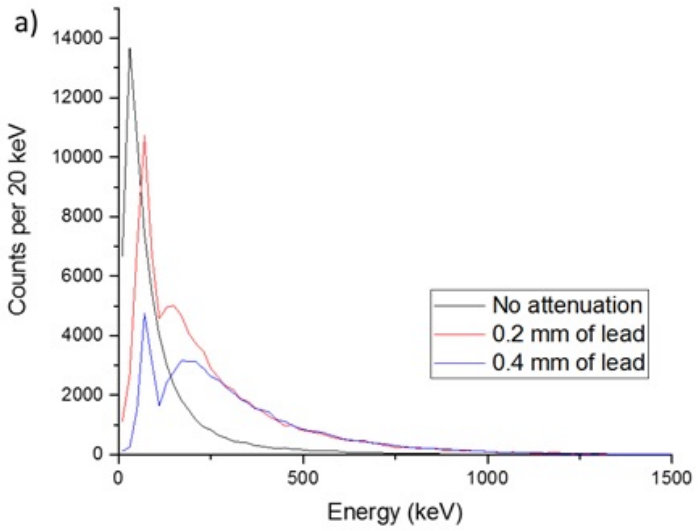


(a)

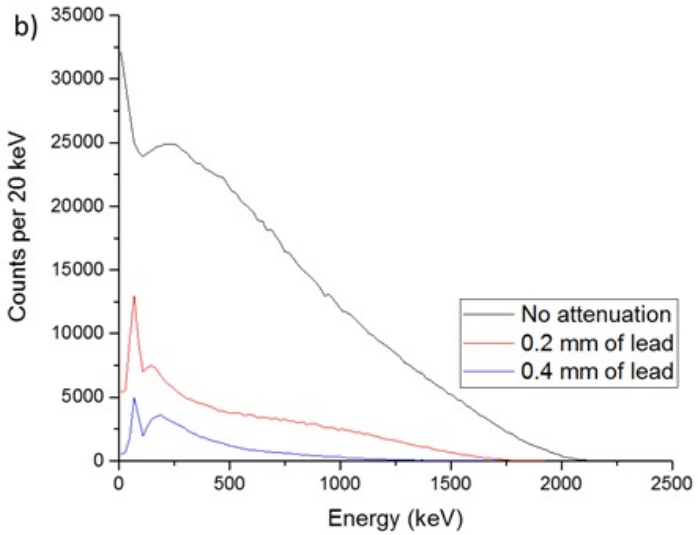


(b)

Figure 2.13: Corresponding attenuated photon spectra (a) and total photon and electron attenuated spectra (b) for the attenuated beta spectra shown in Figure 2.4 in the main text.

Table 2.3: Dose rates and spread for backscatter simulation (see Section 2.2.1 in main text for more details). Shapes marked with an asterix have the same volume

| | Dose rate (Gy/s) | | | | | | | |
|---|---|---|---|---|---|---|---|---|
| | Vacuum | Perspex | Al | Cu | Stainless Steel | Pb | Range | Vacuum Ratio |
| Cone (150,300) | 0.0156 | 0.0169 | 0.02 | 0.025 | 0.024 | 0.033 | 79% | 115% |
| Cone* (50,200) | 0.0139 | 0.0155 | 0.0191 | 0.0261 | 0.0249 | 0.0371 | 102% | 167% |
| Cylinder* (50,66) | 0.0153 | 0.0169 | 0.0207 | 0.0275 | 0.0263 | 0.0382 | 95% | 149% |
| Cylinder (300,300) | 0.0154 | 0.0166 | 0.0194 | 0.0238 | 0.0230 | 0.0307 | 72% | 100% |
| Cylinder (300,5) | 0.0151 | 0.0171 | 0.0213 | 0.0276 | 0.0266 | 0.0381 | 95% | 153% |
| Sphere (100,) | 0.0155 | 0.0167 | 0.0201 | 0.0252 | 0.0245 | 0.0337 | 80% | 118% |
| Sphere* (50,) | 0.0151 | 0.0095 | 0.0207 | 0.0269 | 0.0256 | 0.0369 | 97% | 144% |
| Overall Range | 11% | 10% | 11% | 15% | 14% | 21% | | |
| Range for constant volumes | 10% | 9% | 8% | 5% | 5% | 3% | | |

# References

Agostinelli, S., Allison, J., Amako, K., Apostolakis, J., Araujo, H., Arce, P., et al., (Geant4 Collaboration). Geant4 - a simulation toolkit Nuclear Instruments and Methods in Physics Research Section A. 2003:506(3);250-303

Allison, J., Amako, K., Apostolakis, J., Araujo, H., Arce, P., Asai, M., et al., (Geant4 Collaboration). Geant4 development and applications. IEEE Transactions on Nuclear Science. 2006:53(1);270-278

Armitage, S.J., Bailey, R.M. The measured dependence of laboratory beta dose rates on sample grain size. Radiation Measurements. 2005:39(4);123-127

Behrens, H., L. Szybisz,. Shapes of Beta Spectra, Physics. Physics Data 6-1. Germany, Zentralstelle für Atomkernenergie-Dokumentation (ZAED). 1976

Bøtter-Jensen, L., Andersen, C.E., Duller, G.A.T., Murray, A.S. Developments in radiation, stimulation and observation facilities in luminescence measurements Radiation Measurements. 2003:37(4-5);535-541.

Einstein, A. Über die vom Relativitätsprinzip geforderte Trägheit der Energie. Annalen der Physik. 1907; 328:371-384

Evans, R.D. The Atomic. Nucleus Krieger Publishing Company. 1985. pp. 972

Fain, J., Sumana, S., Montret, M., Miallier, D., Pilleyre, T., Sanzelle, S. Beta-dose attenuation for various grain shapes calculated by a Monte-Carlo method. Quaternary Geochronology.1999:18; 231-234.

Galbraith, R., Roberts, R.G., Laslette, G. Yoshida, Olley, J. Optical dating of single and multiple grain Quartz from Jinmium Rock Shelter, Nothern Australia. Part I, experimental design and statistical models. Archaeometry. 1999:41(2);339-364

Goedike, C. Calibration of a 90Sr/90Y-source for luminescence dating using OSL. Radiation Measurements 2007:42(9);1427-1431

Greilich, S., Murray, A.S., Bøtter-Jensen, L. Simulation electron transport during beta irradiation. Radiation Measurements. 2008:43(2-6);748-751

Guérin, G. Modélisation et simulation des effects dosimétriques dans les sédiment quaternaires : application aux méthodes de datation par luminescence (PhD thesis) Université Bordeaux, 2011

Guérin, G., Mercier, N., Nathan, R., Adamiec, G., Lefrais, Y., 2012. On the use of the infinite matrix assumption and associated concepts: a critical review. Radiation Measurements. 2012:47(9);778-785.

Guérin, G., Jain, M., Thomsen, K.J., Murray, A.S., Mercier, N.,. Modelling dose rate to single grains of quartz in well-sorted sand samples: The dispersion arising from the presence of potassium feldspars and implications for single grain OSL dating. Quaternary Geochronology. 2015:27;52-65

Hansen, V., Murray, A., Buylaert, J.P., Yeo, E.Y., Thomsen, K. A new irradiated quartz for beta source calibration. Radiation Measurements. 2015:81;123-127

Ingram, S., Stokes, S., Bailey, R. Confirmation of backscattered beta dose enhancement rates based on single aliquot regeneration (SAR) analysis of quartz sand and silt. Ancient TL. 2001:19(2);51-54

Lapp, T., Jain, M., Thomsen, K.J., Murray, A.S., Buylaert, J.P. New luminescence measurement facilities in retrospective dosimetry .Radiation Measurements. 2012:47(9);803-808

Mauz, B., Lang, A. The dose rate of beta sources for optical dating applications: A comparison between fine silt and fine sand quartz Ancient TL. 2005:22(2);45-48

Mott, N.F. The Polarisation of Electrons by Double Scattering. Proc. Roy. Soc. 1935;A135:429-458

Murray, A.S, and Wintle, A.G. Beta source calibration. PACT. 1979:3;419-427

Murray A.S. and Wintle A.G. Luminescence dating of quartz using an improved single-aliquot regenerative-dose protocol. Radiation Measurements. 2000:32(1);57-73.

Murray, A., and Wintle, A. The single aliquot regenerative dose protocol: Potential for improvements in reliability. Radiation Measurements. 2003:37(4-5);377-381.

Rutherford, E. The Scattering of alpha and beta rays by Matter and the Structure of the Atom. Philos. Mag. 1935:6;21

Salvat, F., Fernandez-Varea, J.M., Acosta, E., Sempau, J . PENELOPE - A Code System for Monte Carlo Simulation of Electron and Photon Transport. Workshop Proceedings, Issy-les-Moulineaux, France, (November 2001), AEN-NEA.

Thomsen, K.J., Murray, A.S., Bøtter-Jensen, L. Sources of variability in OSL dose measurements using single grains of quartz. Radiation Measurements. 2005:39(1);47-61.

Wintle, A.G. and Aitken, M.J. Absorbed dose from a beta source as shown by thermoluminescence dosimetry. International Journal of Applied Radiation and Isotopes. 1977:28(7);625-627

# Chapter 3

# Towards the origins of over-dispersion in beta source calibration

Vicki Hansen[1], Andrew Murray[1], Kristina Thomsen[2], Mayank Jain[2], Martin Autzen[2], Jan-Pieter Buylaert[1,2]

[1] *Nordic Laboratory of Luminescence Dating, Department of Geoscience, Aarhus University, Denmark,*
[2] *Center for Nuclear Technologies, Technical University of Denmark, DTU Risø Campus, Denmark* Published in *Radiation Measurements*

---

**Abstract:** The ability to deliver accurate and precise calibration doses is a central part of all trapped charge dating methods. Usually, the radiation source (alpha, $\beta$, X-ray) used to deliver these doses is, in turn, calibrated against an absolutely known reference source (usually a $\gamma$ source) and many laboratories make use of Risø calibration quartz for this purpose. We have previously described this material in detail (Hansen et al., 2015) and discussed the over-dispersion (OD) of 3.2±0.3% in calibrated dose rate observed over 16 years. This dispersion highlights the danger of relying on individual calibrations, and is clearly undesirable. Here we continue our investigation into providing reliable calibration materials for trapped electron dating. A comparison of the apparent quartz $\beta$ source dose rates shows that there is no significant dependence on geological source. However the $\beta$ dose rate decreases by 25 % with increasing grain size from about 100 µm

to 1 mm, and backscatter leads to a dose rate increase of ∼1% per unit atomic number of the substrate. It is concluded that, for the multi-grain aliquots used in this study, the contributions to dose rate variability from grain size and substrate variations are likely to be negligible. Nevertheless there may be a practical advantage in using a high Z substrate because of the higher dose rate. Finally we test the measured to given dose (dose recovery) ratio for five heated feldspar samples and use the $pIRIR_{290}$ signal for $\beta$ source calibration; surprisingly this gives an apparent $\beta$ dose rate 15% lower than that to quartz despite their almost identical stopping power and mass absorption characteristics. Our results are discussed in terms of their significance for reproducibility and accuracy of $\beta$ dose-rate estimates.

---

## 3.1 Introduction

Luminescence dating depends on an accurate and precise calibration of dose rate relevant to laboratory irradiations. In most routine analytical procedures for the measurement of natural dose, known laboratory doses are given using a radiation source (usually a $\beta$ source) mounted on the luminescence reader. This local source must then be cross-calibrated against some independently calibrated standard, usually a $\gamma$ source. In practice, the phosphor of interest is first given an accurately known $\gamma$ dose by exposing it to a $\gamma$ source of independently known dose rate (e.g. Bos et al., 2006; Hansen et al., 2015). The luminescence signal (TL or OSL) resulting from this known $\gamma$ dose is then matched with that resulting from a timed irradiation using the $\beta$ source to be calibrated, and the dose rate calculated by proportion, i.e. $D_\gamma \chi_\gamma = t\dot{D}_\beta \chi_\beta$ . Thus

$$\dot{D}_\beta = \frac{D_\gamma \chi_\gamma}{t \chi_\beta} \approx \frac{D_\gamma}{t} \tag{3.1}$$

where $D_\gamma$is the dose absorbed from the $\gamma$ source, and $\chi_\gamma$ and $\chi_\beta$ the luminescence sensitivity to $\gamma$ and $\beta$ radiation, respectively. $\dot{D}_\beta$ is the $\beta$ source dose rate, and t the $\beta$ irradiation time required to match the luminescence produced by the $\gamma$ irradiation. Because $\beta$ particles and $\gamma$ rays are known to deposit energy through similar mechanisms, $\chi_\gamma$ is usually assumed to be indistinguishable from $\chi_\beta$, and so the $\beta$ source dose rate reduces to $D_\gamma/t$.

Irradiated quartz grains suitable for such a calibration procedure (calibration quartz, CQ, Hansen et al., 2015) have been produced in our laboratory for many years, and these have been widely used by the international community since before 1990. Kadereit and Kreutzer (2013) pointed out that the measured dose in our CQ may depend on the parameters chosen in the measurement procedure. Nevertheless, Bos et al. (2006) showed that, using a standard SAR protocol (225 °C preheat for 10 s; 200 °C cut-heat; 125 °C stimulation with blue light) the $\beta$ source calibration derived from our Batch 8 prepared in 2004 was indistinguishable from that derived from an independently prepared and $\gamma$ irradiated quartz sample from their laboratory. However, Porat (p.c., 2015) has since reported an apparent 30% difference in calibration based on Batch 17, compared with that from both 57 and 71. Rhodes (p.c., 2015) reports a single-grain dose-rate difference of 12% between Batch 71 and 98, and Huot (p.c., 2012) up to 21% difference between Batch 17 and 60. Even within our own laboratory apparently systematic batch-to-batch discrepancies of up to 10% have been observed. The reliability of the $\beta$ source calibration is a very serious issue for our community and so we have initiated investigations of the accuracy and precision of our calibrations, both past and present.

Hansen et al. (2015) presented the reproducibility of various batches of CQ over >13 years and we have since extended this data set by three more years (Figure 3.5a) and five additional new batches of calibration quartz. The average standard deviation from an exponential decay (Figure 3.5b, solid line) is 3%, and the ratio of the fitted decay constant to that of $^{90}$Sr is 0.96±0.05. The average dose rates have an over-dispersion of 2.8±0.7% around the fitted line (Figure 3.5b), and the maximum deviations of individual calibration measurements from the fitted line are as large as 10%.

Here we describe further investigations into laboratory parameters that might affect the accuracy and precision of our CQ. We first compare the apparent $\beta$ source dose rates based on quartz derived from different geological sources and then investigate the dose rate dependence on grain size and atomic number of the sample holder used to hold the phosphor grains. After testing the dose recovery ratio for five heated feldspar samples, the $pIRIR_{290}$ signal is also used for $\beta$ source calibration and the resulting apparent dose rate compared with that derived using quartz. This result is then compared with that predicted from Monte Carlo modelling. Finally our observations are discussed in terms of significance for reproducibility and accuracy of laboratory $\beta$ dose rates.

## 3.2 Instrumentation

All luminescence measurements were undertaken using a Risø TL/OSL DA-20 luminescence reader fitted with blue LEDs (470 nm , ∼80 mW cm$^{-2}$) and a $^{90}$Sr/$^{90}$Y $\beta$ source (Bøtter-Jensen et al., 2010). For measurement, a monolayer of quartz grains were mounted on 0.3 mm thick stainless steel discs using silicone oil. OSL signals were derived from the first 0.64 s of stimulations minus the subsequent 0.64 s. Equivalent dose measurements employed a SAR protocol (Murray and Wintle, 2000, 2003) with a 260 °C for 10 s/ 220 °C preheat/cutheat, stimulation at 125 °C and cleanout with stimulation at 280 °C for 40 s. XRF measurement made use of a Risø XRF attachment to the reader (Kook et al., 2012) specifically designed for characterising the composition of quartz and feldspar extract, (e.g. Porat et al., 2015). All XRF feldspar grains were measured as loose grains on Mo cups.

## 3.3 Apparent dose rate dispersion using quartz of different origins

Calibration quartz has been produced in our laboratory for over 40 years and during that time, several different parent sediments have been employed. Although all these came from the west coast of Jutland, sediment in this region can derive from a variety of geological provinces. Accordingly the possible contribution to batch-to-batch variability from different sources of quartz was examined by investigating whether the apparent dose rate depends on the geographical origin of the quartz extracts. To increase the chance of differences in geological provenance, 9 different quartz samples were selected from various widely-separated locations around the world; these were then sensitised by heating to 700 °C for 1 hour. The latter also ensures that the OSL signals are dominated by the fast component. They were then given a 2 kGy $^{60}$Co gamma dose followed by heating to 450 °C for 1 hour to empty the dosimetry trap (Hansen et al., 2015). The suitability of these samples for use as calibration quartz was then confirmed by irradiating aliquots of each sample with a $\beta$ source for a known length of time, and then measuring this given dose in the usual manner. The results of this $\beta$ dose recovery test are summarised in Figure 3.1 (green symbols), and it can be seen that all dose recovery ratios lie well within ±10% of unity; the mean ratio is 1.008±0.013 (n=9). Nevertheless two of the nine results (Namibia, France) are statistically inconsistent with unity. The nine sensitised samples were then placed individually in glass tubes (2.25 mm wall thickness) and

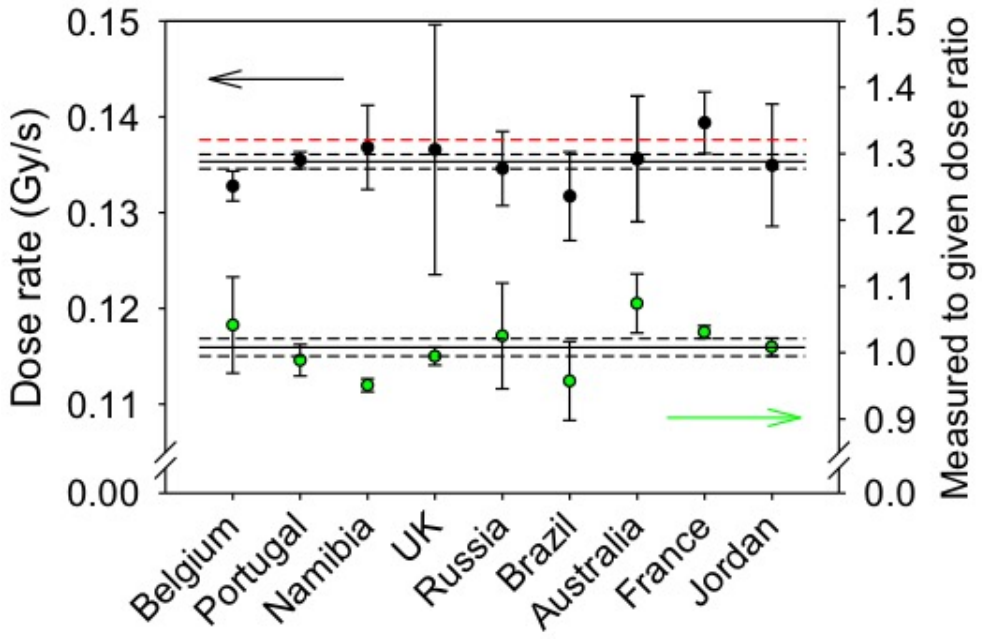


Figure 3.1: Top: $\beta$ source dose rate derived using nine different quartz samples from widely varying locations around the world. Red dashed line represents average beta source dose rate from Batch 90. Bottom: dose recovery ratio for the same samples. All data represents the average of six 8 mm aliquots measured per sample, and error bars represent one standard error.

irradiated at the same time 2.0 m from a calibrated point $^{137}$Cs source in a scatter-free geometry (Hansen et al. 2015), to give an absorbed dose of 4.81±0.07 Gy.

The apparent dose rates derived from these nine samples are summarised in Figure 3.1 (black symbols). All individual calibrations are consistent with a mean dose rate of 0.1353±0.0008 Gy s$^{-1}$ (n=9); this includes the two samples for which the dose recovery ratios were not consistent with unity. For reference, the mean dose rate based on Batch 90 (0.1376±0.0012 Gy s$^{-1}$, n=28) is shown in red (see also Figure 3.5). It is concluded that there is no evidence for a dependence of apparent dose rate on the origin of the quartz extract.

## 3.4 Grain size and substrate dependence

### 3.4.1 Grain size

One possible cause of variation in apparent dose rate from aliquot to aliquot, and from sample to sample, is variation in mean grain size. The dose rate to grains of different sizes will be affected by Z-dependent backscatter (Chapter 2: Autzen et al., 2017) and build up effects (Wintle and Aitken, 1977). In the preparation of standard calibration quartz, all grains are sieved to 180 to 250 µm, but that still allows a possible range in grain diameter of >30% compared to the mean. Because of this, we have revisited and extended earlier investigations of the dependence of the apparent $\beta$ source dose rate on grain size (e.g. Armitage and Bailey, 2005; Mauz and Lang, 2004). Various grain size fractions (see Figure 3.2) were separated from the parent sand H33052 (Rømø Denmark, used since Batch 90), except for the fractions in 300-1000 µm range, which were extracted from sample 178109 (aeolianite from Oitavos, Portugal). All fractions were pretreated and sensitised in the usual manner (Section 3.3). After checking for the absence of a significant feldspar signal, dose recovery experiments were undertaken using each grain size (Figure 3.2a). While most of the dose recovery ratios are within 10% of unity, there is a systematic trend of decreasing ratio with increasing grain size, and for the grain size intervals 500-800 µm and 800-1000 µm, the ratios fall below 0.9. These grain size fractions were then given an accurately known $\gamma$ dose as described above, and the apparent $\beta$ dose rates derived. The unfilled circles in Figure 3.2b show this observed grain-size dependence. The filled circles in Figure 3.2b show these observed dose rates divided by the appropriate dose recovery ratio. This is appropriate here (in contrast to natural doses, for which the evidence is ambiguous) because the two experiments are directly comparable, except that in one experiment both doses are given by a $\beta$ source, and in the other the first by a $\gamma$ source. Thus it is very likely that any systematic difference observed in one experiment will also be present in the other. There is also a further point at 1.0 mm, based on 1 mm thick quartzite rock slices (dose recovery given in Figure 3.2a), and after correction this lies on the smooth curve defined by the smaller grain sizes. The initially flat or slightly rising part of the curve was explained by Wintle and Aitken (1977) as the effect of build-up, where the electron flux (and so the dose rate) increases as the beam passes from air to quartz. The subsequent decrease with grain size is to be expected from the larger average contribution from low energy backscatter to smaller grain sizes (Chapter 2: Autzen et al., 2017) and the greater attenuation of the primary spectrum as the grain size increases. Similar data have been

reported by Armitage and Bailey (2005) and Mauz and Lang (2004). From this curve it can be predicted that the dose rate to 180 µm grains should be ∼1.5% greater than that to 250 µm; this is small compared to the observed range of 10% in apparent $\beta$ dose rate reported above.

### 3.4.2 Substrate

The substrate on which grains are irradiated contributes to the total beta dose rate by scattering incident electrons back into the quartz grains. When calibrating a $\beta$ source, grains are usually presented either loose in a thin metal cup (usually 0.1 mm stainless steel) or adhered to a flat metal disc (0.3 mm stainless steel or aluminium) using silicone oil. The main advantage of the cup is the ability to hold a large sample (up to ∼20 mg) but this is at the cost of significant dependence of the mean dose rate on sample mass, because the backscatter from quartz is different from that from stainless steel. Murray (1981) was the first to investigate this, and he showed that for an infinitely thick substrate (i.e. a substrate thickness very large compared to the range of the incident particles) the apparent $\beta$ dose rate to $CaF_2$ (mean Z=12.7) on aluminium (Z=13) was ∼13% lower than on steel (Z∼26), and Greilich et al. (2008) and Chapter 2 (Autzen et al., 2017) have since modelled these data. Since the effective Z of quartz (Z∼10) is slightly less than that of aluminium, the dose rate to a quartz grain sitting directly on steel will thus be considerably more than that to a grain sitting on other quartz grains. In practice, we do not irradiate on infinitely-thick substrates, and so we have investigated the variation in apparent $\beta$ dose rates to be expected for a monolayer of quartz grains placed in 0.1 mm thick cups made from a variety of substrates (Figure 3.3a).

The variation in dose rate compared to that for grains irradiated on steel is considerable, from ∼0.78 for aluminium, up to ∼1.4 for platinum. These effects are considerably larger than those described earlier, presumably because in thin substrates density effects become important; for a given thickness of metal, there are 40% more atoms per unit area in a steel cup than in one made from aluminium. In addition, the $\beta$ dose rate to 180-250 µm grains in platinum cups is ∼40% higher than in conventional stainless steel cups. This increase offers the possibility of a greater routine beta dose rate in dating applications, but this can only be taking advantage of if the net spectrum to which the grains are exposed during irradiation is at least as suitable as that experienced on steel and aluminium.

Chapter 2 (Autzen et al., 2017) undertook Monte Carlo modelling (using GEANT4) of the incident $\beta$ source spectrum and the backscattered spectra from infinitely thick substrates of various Z. These show that the main effect of changing Z is to change the intensity of the backscattered spectrum,

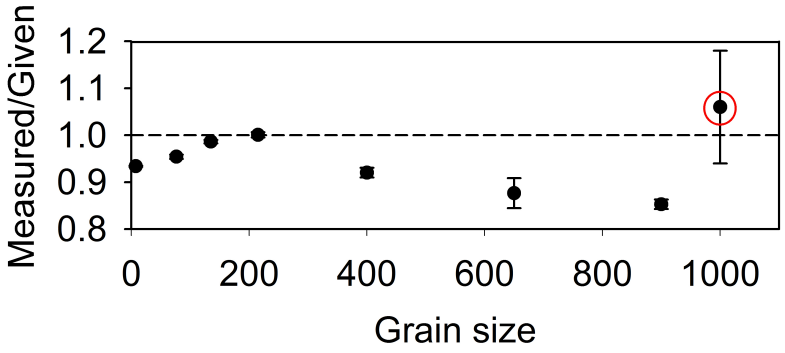


(a)

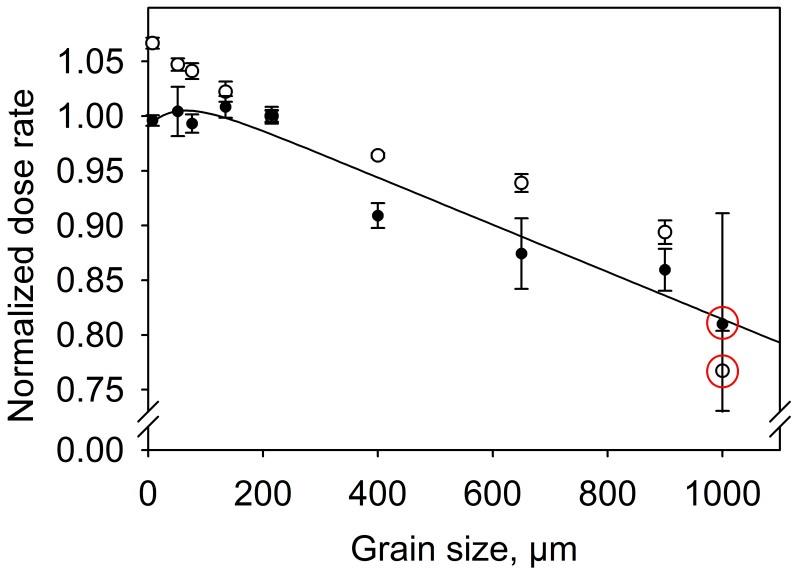


(b)

Figure 3.2: a) Beta dose recovery as a function of grain size (4-11, 40-63, 63-90, 90-180, 180-250, 300-500, 500-800, 800-1000 µm); red circle - 1 mm thick rock slice drilled from quartzite (unknown origin). b) Dose rate dependence on grain size, for grains mounted in stainless steel discs; red circle - 1 mm rock slice.

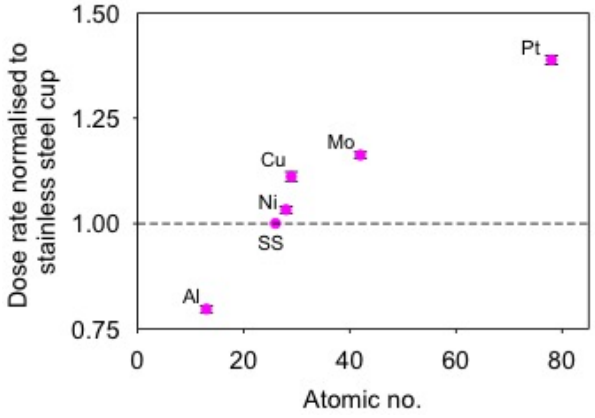


(a)

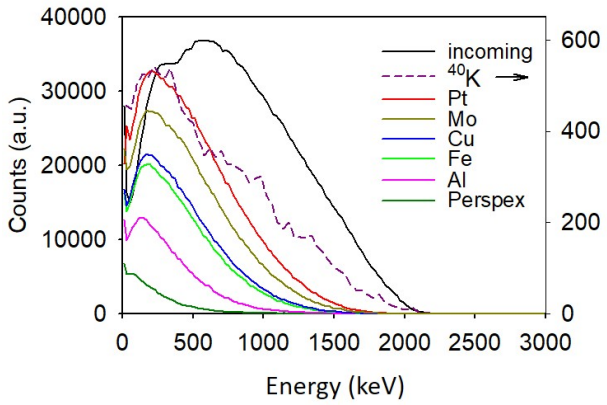


(b)

Figure 3.3: $\beta$ dose rate to quartz in cups as a function of atomic number normalised to that in conventional stainless-steel cups. (SS is derived using Fe) b) Modelled $\beta$ source incident spectrum, and backscattered spectra from various infinitely thick substrates. Later modelling will use finite cup thickness and geometry, but this is expected to primarily reduce the intensities of the spectra.

but that there is a relatively small effect on the energy distribution. In Figure 3.3b, we present the primary $\beta$ spectrum and backscattered spectra using different substrates (all except Pt, Mo are from Chapter 2: Autzen et al., 2017). For comparison, we have also calculated the infinite matrix $\beta$ spectrum from $^{40}$K, as representing a natural spectrum. It appears that a standard total laboratory spectrum (primary + backscattered) derived from irradiation on steel discs is likely to contain many more high-energy electrons than any infinite matrix beta spectrum. It is thus likely that the total spectrum resulting from irradiation on a high Z substrate (e.g. Pt, Z=78, Figure 3.3a) will be closer to the natural spectrum that those on lower Z substrates.

## 3.5 K-Feldspar

To test whether the observed over-dispersion in the quartz calibration time-series (Figure 3.5) is related only to the luminescence characteristics of quartz or to variability in measurement procedures/instrumentation, we have begun to investigate the potential of using feldspar pIRIR signals for calibration. From simple examination of mass absorption coefficients (NISTIR 5632) and stopping powers (NISTIR 4999), we anticipate that the beta dose rate to quartz and feldspar should be indistinguishable. To confirm this, we have used GEANT4 to formally model both the ratio of $\gamma$ dose rates in pure K feldspar and pure quartz (0.993±0.002 (n=5), averaged over a 1 mm thick slice) and the corresponding $\beta$ dose rate ratio (1.0032±0.0008, for a 200 µm thick slice of dosimeter placed on 0.5 mm stainless steel substrate). These data confirm that the $\beta$ dose rate to feldspar should be within 1% of that to quartz.

K-feldspar was extracted ($\rho$ <2.58 g cm$^{-3}$) from the same sediment H33052 (Rømø Denmark) as is used for calibration quartz batch 90 onwards; a typical pIRIR$_{50,290}$ luminescence curve is shown in Figure 3.4a (measured during IR stimulation with the sample held at 290 °C, after first preheating to 320 °C for 60 s and then IR stimulation with the sample held at 50 °C); for reference, the normalised SAR dose response curve is shown in the inset, compared to that of the calibration quartz derived from the same sample.

Before this K-rich feldspar extract can be used for calibration it must be shown to be pure, and we must test whether a laboratory $\beta$ dose can be recovered using our chosen pIRIR$_{50,290}$ protocol. Figure 3.4b shows the results of XRF analysis; the fraction of K-feldspar is >90% for all samples. Figure 3.4c shows the results of the $\beta$ dose recovery test on sample H33052 after first heating to 550 °C for 1 hour; the dose recovery ratio is indistin-

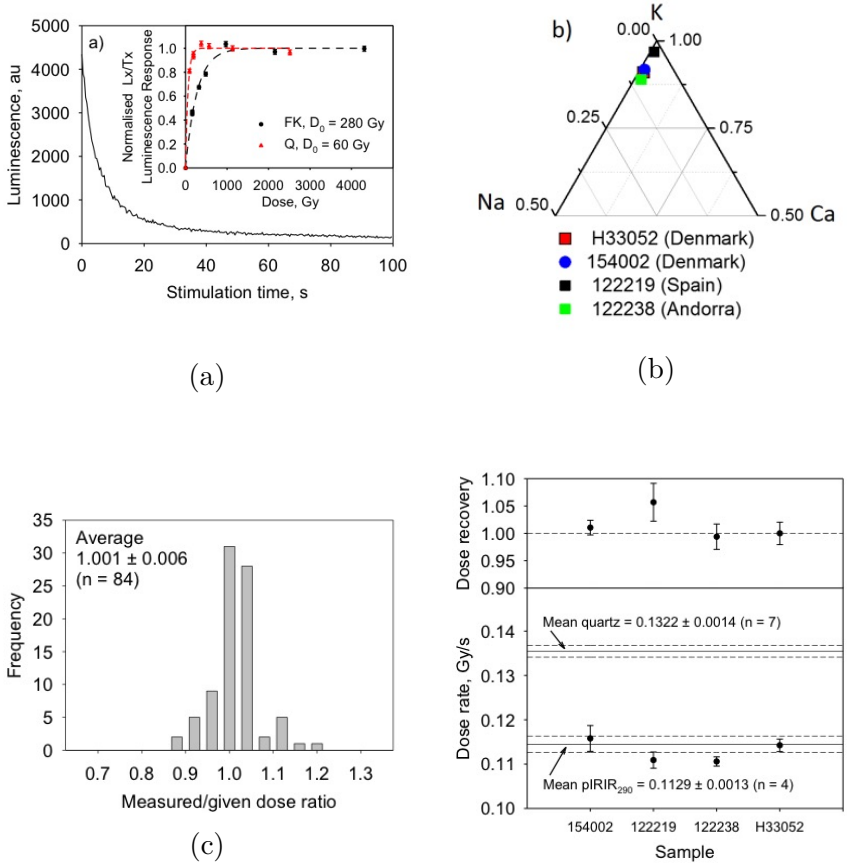


(a) (b)

(c) (d)

Figure 3.4: A $pIRIR_{50,290}$ decay curve from a 2 mm large aliquot of K-feldspar from H33052 given a $\gamma$ dose of 4.81±0.07 Gy. The inset shows the normalised $pIRIR_{50,290}$ (black) and quartz OSL (red) dose response curves. b) Ternary diagram showing results of XRF-analyses of different K-feldspar extracts. c) Beta dose recovery histogram for K-feldspar from H33052 (annealed 550 °C/ 1h). d) Dose recovery and apparent beta source dose rate for different K-feldspar extracts.

guishable from unity and the data have a relative standard deviation of ∼5%.

A portion of this heated extract was then exposed to the $^{137}$Cs gamma source as described above, and the $\beta$ source calibrated in the usual manner, but using the $pIRIR_{50,290}$ signal. Rather disturbingly, the average apparent $\beta$ source dose rate to feldspar is significantly lower (∼15%) than that measured using standard calibration quartz (Figure 3.4d, sample H33052).

As a further test of this unexpected discrepancy, three additional pure K-rich feldspar extracts from different locations (Figure 3.4b) were prepared as above, and irradiated together in the $^{137}$Cs $\gamma$ source. Note that these three K-feldspar extracts also yield dose recovery ratios consistent with unity (Figure 3.4d, top). The weighted mean of all four measurements is $0.1119\pm0.0007\,\mathrm{Gy\,s^{-1}}$ (6 aliquots per sample). The data are not over-dispersed, but this is not surprising since all 24 aliquots were measured in a single sequence; the quartz over-dispersion arises mainly from sequence to sequence. Nevertheless, these dose rates are consistent with an average ratio of $0.854\pm0.013$ to that of quartz (Figure 3.4d, bottom). The implications of this difference are considerable, and this unexpected discrepancy clearly requires further investigation. However, we can confidently rule out instability of the $pIRIR_{50,290}$ signal as a significant contribution, because this would tend to lead to an over-estimate of the $\beta$ source dose rate, rather than an underestimate.

## 3.6 Discussion and Conclusions

It is clear that both the grain-size dependence and the backscatter contribution have the potential to contribute to multi-grain aliquot-to-aliquot over-dispersion during $\beta$ irradiation. Both grain-size dependent attenuation effects on the backscattered and primary spectra, and the possibility of one grain sitting on top of another (and so experiencing a different backscatter contribution from grains sitting directly on the substrate) could lead to unexpected variability. The slope of the grain size dependency in Figure 3.2b is $\sim 7 \times 10^{-4}$ µm$^{-1}$ (for grain sizes $> 100$ µm); the grain size range used here is 180-250 µm, suggesting an upper limit to the range in dose rates of $((250 - 180) \times 7 \times 10^{-4}) = 5\%$, about half of that observed. In practice, no samples will be entirely 180 µm or 250 µm, and so the real range in dose rates arising from grain size variation will be much smaller than this. The variation in dose rate arising from substrate variation is readily eliminated by ensuring a monolayer of grains on the substrate. Thus, we anticipate that, in practice for the multi-grain aliquots used in Figure 3.5, the contri-

butions to dose rate variability from grain size and substrate variations are likely to be negligible.

However, investigations into the effect of substrate variation do lead us to a conclusion of some practical importance. From modelling, we deduced that the net electron spectrum is likely to be closer to that experienced in nature for high Z substrates (although whether that is important is unknown). Thus it is concluded that there are unlikely to be any significant undesirable effects of using high Z substrates such as platinum (Pt) cups in routine irradiations, although it would be very important to ensure grains were presented as a monolayer. In contrast, there is likely to be significant practical benefit in using Pt cups; the average dose rate would be 40% greater than on stainless steel, and 75% greater than on Al.

The original motivation for investigating the $\beta$ dose rate to feldspar was to test whether the poor reproducibility in quartz calibration arises because of instrument variability. At this stage in our investigations, we do not draw any conclusions on this. However, an unexpected difference of 15% in dose rate to quartz and feldspar has been observed. This is surprising because modelling suggests there should be no difference between feldspar and quartz calibrations. It is deduced that this difference must arise from differences in quartz and feldspar luminescence response to $\gamma$ and $\beta$ radiation (i.e. in $\chi_\gamma$ and$\chi_\beta$ for quartz and feldspar in Equation (3.1)). Given the observed reproducibility from sample to sample (in both Q and KF, Figure 3.1 and Figure 3.4d) this difference is likely to be due mainly to crystal structure. Nevertheless, some grain-to-grain variation in dose rate within quartz and feldspar cannot be ruled out because of variations in both attenuation and backscatter.

Nevertheless, if this observation proves reliable, and if it applies to the natural $\beta$ dose rate, then the effect on ages will be relatively small (<5%) because the total beta dose rate component makes up about >70% of the total. But this remains to be tested experimentally.

In summary,

- The average apparent quartz dose rate is independent of the source of the quartz.
- The effect of likely grain size and substrate variations on $\beta$ dose rate reproducibility is probably not significant.
- It may be possible to increase effective $\beta$ source dose rates by ∼40% using platinum instead of stainless steel cups.

- The apparent $\beta$ dose rate to feldspar is $\sim$15% less than that to quartz, independent of origin; whether this translates into a 15% error in age depends on whether the same effect occurs in nature.

**Acknowledgements**
We thank Sébastien Huot, Ed Rhodes and Naomi Porat for reporting their Batch dependence of source calibrations, and Warren Thompson for providing the quartzite rock slices. J.-P. Buylaert and M. Autzen receive funding from the European Research Council (ERC) under the EU Horizon 2020 programme ERC-2014-StG 639904 - RELOS.

## 3.7 Supplementary Material for Chapter 3

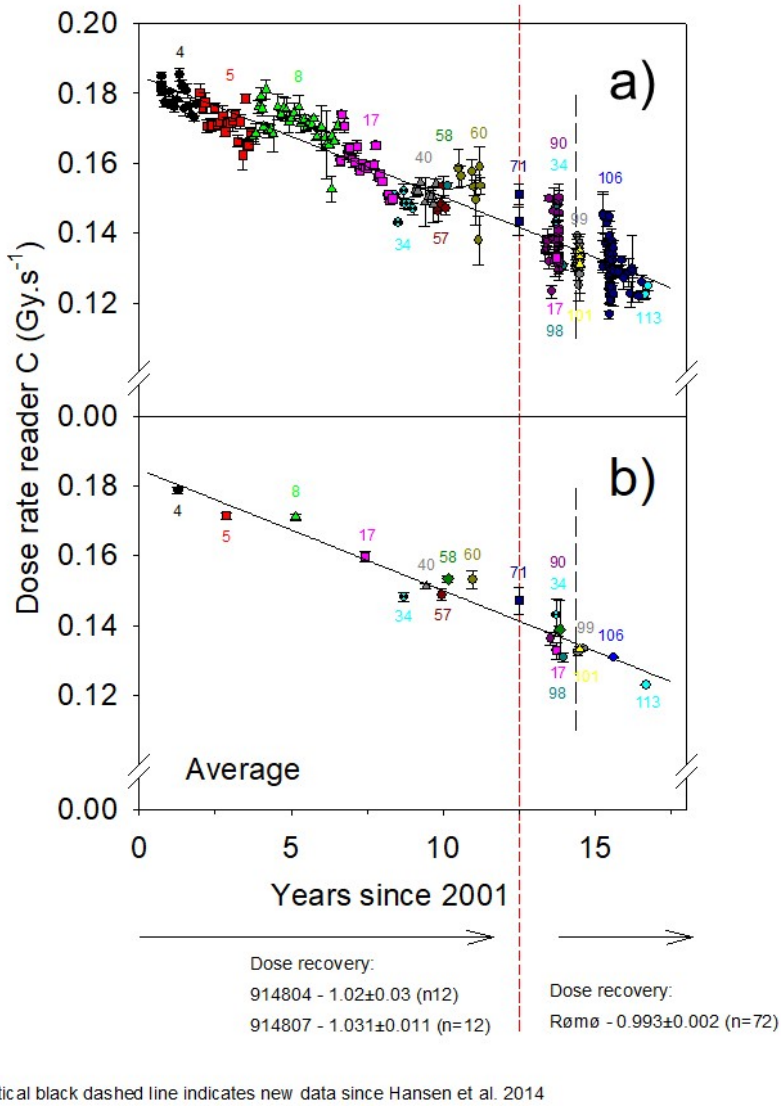


Figure 3.5: a) Dose rate variation with time on reader C, based on Hansen et al. (2015) with additional data (short grey dashed lines at 14.4 years indicate start of new data). Each point represent the average and standard error of 6 aliquots (all 180-250 µm on stainless steel discs, 8 mm aliquots until year 12.5, thereafter 3 mm.) b) Data from a) averaged over each batch and measurement period. The vertical red dashed line at 12.5 years going through both a) and b), indicates the change in source material used to manufacture calibration quartz. Prior to this quartz was extracted from marine sediment cores 914804 and 914807 from northwest Jutland. After this date, quartz was extracted from aeolian dune sand collected from Rømø in 2013. The dose recovery ratios are shown below b) for each sample.

# References

Armitage, S.J. and Bailey, R.M., 2005. The measured dependence of laboratory beta dose rates on sample grain size. Radiation Measurements 39, 123-127.

Autzen, M., Guérin, G., Murray, A.S., Thomsen, K.J., Buylaert, J.-P., Jain, M. 2017. The effect of backscattering on the beta dose absorbed by individual quartz grains. Radiation Measurements 106, 491-497.

Bos, A.J.J., Wallinga, J., Johns, C., Abellon, R.D., Brouwer, J.C., Schaart, D.R., Murray, A.S., 2006. Accurate calibration of a laboratory beta particle dose rate for dating purposes. Radiation Measurements 41, 1020-1025.

Bøtter-Jensen L., Thomsen, K.J., Jain, M. 2010. Review of optically stimulated luminescence (OSL) instrumental developments for retrospective dosimetry. Radiation Measurements 41, 253-257.

Greilich, S., Murray, A.S., Bøtter-Jensen, L. 2008. Simulation of electron transport during beta irradiation. Radiation Measurements 43, 748-751.

Hansen, V., Murray, A.S., Buylaert, J.-P., Yeo, E.-Y., Thomsen, K.J., 2015. A new irradiated quartz for beta source calibration. Radiation Measurements 81, 123-127.

Kadereit, A., Kreutzer, S., 2013. Risø calibration quartz - A challenge for $\beta$-source calibration. An applied study with relevance for luminescence dating measurement. Journal of the International Measurement Confederation 46, 2238-2250.

Kook, M.H., Lapp, T., Murray, A.S., Thiel, C., 2012. A Risø XRF attachment for major element analysis of aliquots of quartz and feldspar separates, 2012. UK Luminescence and ESR Meeting, Aberystwyth, September 2012 (abstract), p. 37.

Murray, A.S. 1981. Environmental radioactivity studies relevant to thermoluminescence dating. Oxford University, unpublished PhD thesis. 404p.

Murray, A.S., Wintle, A.G., 2000. Luminescence dating of quartz using an improved single-aliquot regenerative-dose protocol. Radiation Measure-

ments 32, 57-73.

Murray, A.S., Wintle, A.G., 2003. The single aliquot regenerative dose protocol: potential for improvements in reliability. Radiation Measurements 37, 377-381.

Mauz B. and Lang A. 2004. Removal of the feldspar-derived luminescence component from polymineral fine silt samples for optical dating applications: evaluation of chemical treatment protocols and quality control procedures. Ancient TL 22, 1-8.

NISTIR 4999: https://physics.nist.gov/PhysRefData/Star/Text/method.html

NISTIR 5632: https://www.nist.gov/pml/x-ray-mass-attenuation-coefficients

Porat, N., Faerstein, G., Medialdea, A., Murray, A.S., 2015. Re-examination of common extraction and purification methods of quartz and feldspar for luminescence dating. Ancient TL 33, 1.

Wintle, A.G., Aitken, M.J., 1977. Absorbed dose from a beta source as shown by thermoluminescence dosimetry. The International Journal of Applied Radiation and Isotopes 28, 625-627.

# Chapter 4

# Luminescence dosimetry: does charge imbalance matter?

Autzen, M.[1], Murray, A.S.[2], Guérin, G.[3], Baly, L.[4], Ankjærgaard, C.[1], Bailey, M.[1], Jain, M.[1], and Buylaert, J.-P.[1,2]

[1] *Center for Nuclear Technologies, Technical University of Denmark, DTU Risø Campus, Denmark,*
[2] *Nordic Laboratory of Luminescence Dating, Department of Geoscience, Aarhus University,Denmark*
[3] *UMR 5060 CNRS-IRAMAT-CRP2A, Université Bordeaux 3, Maison de l'archéologie, 33607 Pessac Cedex, France,*
[4] *Centro Aplicacions Tecnológicas y Desarrollo Nuclear (CEADEN), La Habana, Cuba* Published in *Radiation Measurements*

---

**Abstract:** We use both modelling and high dose experiments to investigate the effects of charge imbalance on luminescence. Charge entering and leaving irradiated 50 µm grains is modelled using Geant4 to predict the degree of charge imbalance a grain will experience when exposed to i) the $^{90}$Sr/$^{90}$Y beta source of a Risø TL/OSL reader, ii) a 200 keV electron beam, and iii) the "infinite-matrix" $^{40}$K $\beta$ spectrum. All simulations predict that between 1.4% and 2.9% more electrons enter a grain than leave, resulting in a net negative charge in the grain. The possible effects of this charge imbalance on luminescence production are discussed and experiments designed to test the resulting hypotheses; these involve giving very high doses (hundreds of kGy) to silt-sized quartz grains using low energy electrons

(200 keV). Up to 700 kGy, we observe an increase in both luminescence output resulting from these high doses, and in sensitivity; above 700 kGy, both decrease. These observations, together with a slower luminescence decay during stimulation following higher doses, are consistent with the hypothesis of a decrease in hole population as a result of net accumulation of electrons during irradiation.

**Keywords:** Geant4; Luminescence; OSL; Charge Imbalance

---

## 4.1 Introduction

Luminescence is widely used to estimate the dose absorbed during burial in natural minerals (e.g. quartz and feldspars) because they store separated charge (electrons and holes) for prolonged periods ($>10^8$ years, e.g. Murray and Wintle 1999) when exposed to ionising radiation. The total amount of stored charge can be calibrated in terms of dose, and knowing the dose rate allows the calculation of burial age, i.e. the time elapsed since the trapped charge was last reset to zero, usually by heat or light. The calibration of total trapped charge in terms of dose is usually undertaken by a comparison of the natural luminescence signal with that induced by a laboratory irradiation. It is clearly important that the luminescence response per unit dose is the same in the laboratory and in nature.

Luminescence models (e.g. Bøtter-Jensen et al., 2003; Bailey 2001, 2004; Adamiec et al., 2004, 2006; Pagonis et al., 2007, 2008) commonly used to describe charge trapping and luminescence recombination in the dating of quartz and feldspar are all based on the assumption of charge neutrality during irradiation, i.e. all these models assume that the crystal contains an equal number of trapped electrons ($n_e$) and trapped holes ($n_h$) at any time. This assumption is taken to hold both in nature and in the laboratory. However, the assumption of charge neutrality is known not to apply in other fields. For instance, as the dose to an insulator (e.g. PMMA or samples under a Scanning Electron-Microscope (SEM)) increases, the incident electron beam has been observed to diverge due to the electric field developed as a result of build up of internal charge; this causes a decrease in range of subsequent electrons entering the insulator (e.g. Tanaka et al., 1979; McLaughlin, 1983). This problem has been observed in the SEM analysis of amorphous and crystalline quartz (Vigouroux et al., 1985; Stevens Kalceff et al., 1996) as well as in crystalline $Al_2O_3$ (Cazaux et al.,

2004). A similar problem is observed in medical dosimetry when irradiating PMMA phantoms and monitoring the response with an ionisation chamber (e.g. Galbraith et al., 1984; Rawlinson et al., 1984; Mattson and Svensson, 1984). This accumulation of charge can significantly affect the dose deposition through a block of plastic or glass and even cause breakdown trees (so-called Lichtenberg trees) if the charged block is tapped with a grounded needle or if the block is stressed mechanically (e.g. Gross, 1957, 1958; Zheng et al., 2008). Discharge of electrical insulators in the space industry is also recognised (Frederickson, 1996) and is known to have caused radiation-induced discharges in semi-conductor devices in satellites, leading to severe failures (Lam et al., 2012).

The charge state of a grain can also be changed by the emission of electrons from grain surfaces (exo-electron emission). This emission has been observed during stimulation with heat (thermally stimulated exo-electrons, TSEE) or light (optically stimulated exo-electrons, OSE) in both quartz and feldspar grains extracted from natural sediments (Ankjærgaard et al., 2006, 2008, 2009; Tsukamoto et al., 2010). The OSE signal appeared to originate from the same trap(s) as the OSL signal (same fast component characteristics) and the OSE signal strength was observed to increase with dose; these observations are evidence that a grain changes its net charge during stimulation. However, exo-electron emission will only be able to affect a fraction of the accumulated net charge; it is a surface phenomenon, involving the outer 1 nm, and thus presumably cannot affect the bulk charge.

In a matrix large compared to the range of the relevant ionising radiation (here termed an "infinite matrix") there must be overall charge neutrality or charge conservation would be violated. However, there is no such requirement for charge neutrality on the scale of an individual grain. Thus, the number of electrons entering a grain (primary electrons) is not necessarily balanced by the number of electrons leaving the grain (primary and secondary electrons) (Figure 4.1) and this charge imbalance may lead to the accumulation of net positive or negative charge in the crystal. In Figure 4.1a, the grain remains neutral as the number of electrons entering and leaving the grain are the same. Even if an electron from an electron-hole pair generated inside the grain escapes it is balanced by one entering from the outside. In Figure 4.1b and Figure 4.1c, the number of electrons entering the grain is not the same as the number of electrons leaving the grain. In Figure 4.1b, there will be more electrons in the grain than holes and the grain will become increasingly negatively charged. Conversely, in Figure 4.1c, there will be more holes than electrons and the grain will become positively charged. In such asymmetric irradiations, the trapped hole population ($n_h$) will not be the same as that of the trapped electrons ($n_e$),

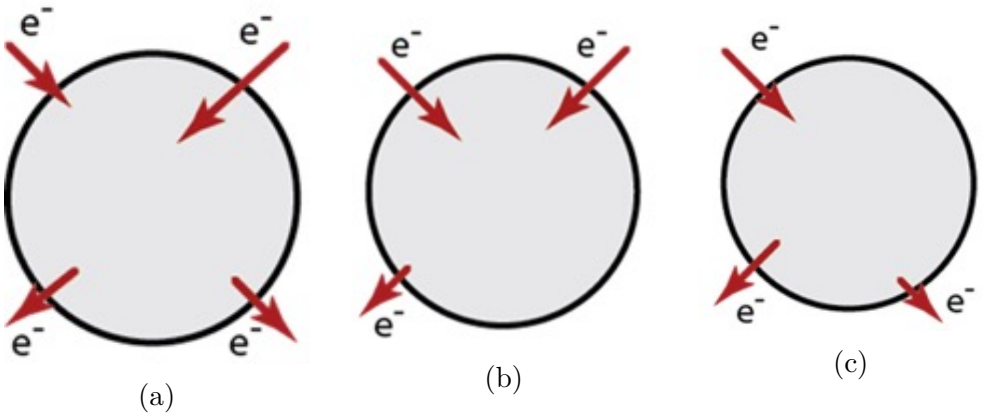


Figure 4.1: a) A charge neutral grain. Each electron, which enters the grain, is balanced by an electron leaving. b) A negatively charged grain. There are more electrons entering the grain than leaving. c) A positively charged grain. There are more electrons leaving the grain than entering

i.e. the ratio $\frac{n_e}{n_h} \neq 1$. At least in principle, the limiting condition is the complete elimination of either trapped electrons or holes.

If the ratio of the number of trapped electrons to holes changes, recombination probabilities and thus luminescence are likely to be affected, either through a changed competition between recombination centres or between retrapping sites. In this paper, we first propose a mechanism for the generation of charge imbalance and consider its possible effects on luminescence production (Section 4.2); Geant4 modelling is then used to quantify some of these effects (Section 4.3). Predictions from modelling are used to design an experiment to test whether charge imbalance (Section 4.4) occurs in practice, and experimental results are presented (Section 4.5). Finally, the implications of this model and our experimental results for accurate dosimetry are discussed.

## 4.2 Charge imbalance: mechanism and possible effect on luminescence production

When ionizing radiation interacts with matter, it deposits energy in several ways, including the generation of free electrons. On average, it takes ∼4 times the band gap to generate a free electron (Wolff, 1954); the electron will then leave behind a relatively less mobile positive charge (hole). In suitable

materials, these free electrons and their corresponding holes can accumulate in electron and hole traps, respectively, and in trapped charge dating the luminescence generated by these trapped charges is used to determine the absorbed dose.

In the rate equations describing luminescence production, the crystal is assumed to remain charge neutral; this implies that for every trapped electron there must also be a trapped hole. This can only be true if an equal number of electrons enters and leaves the grain. For instance, in the luminescence model developed specifically for quartz (Bailey, 2001, 2004; Adamiec et al., 2004, 2006; Pagonis et al., 2007, 2008), the rate of change in concentration of the electrons in the conduction and valence bands is determined by the ionisation rate, i.e. the number of free electron-hole pairs generated per unit energy deposited during ionisation. The ionisation rate determines both the number of electrons and of holes deposited in the crystal. This implicitly assumes charge neutrality - if all trapped electrons are released, they will recombine with all trapped holes, leaving both electron and hole traps empty.

However, it is trivial to imagine situations where this is not the case; for instance, a beta emitting grain in a non-radioactive matrix (where electrons leaving the grain are not matched by electrons entering), or irradiation of a (low-radioactivity) quartz grain by an external low-energy electron spectrum, such that most electrons entering the grain are stopped within the grain. In such circumstances, the degree to which the assumption of charge neutrality fails will depend on the size and shape of the grain as well as the energy spectrum to which the grain is exposed; the net charge remaining in or on the grain can be positive or negative.

### 4.2.1 Negative net charge

When more electrons enter the grain than leave (Figure 4.1b), some of these electrons must thermalise in the interior of the grain, and so be available for trapping. Then electron traps will fill at a faster rate than hole traps. Assuming for simplicity that the electron traps are stable on the timescale of interest, the trapped electron population will eventually saturate, and electron trapping will cease. Given that in practice some electron traps are more stable than others, there will be a tendency for the excess electrons to accumulate in the deeper traps (assuming that recombination is the only way to permanently remove trapped charge). Once all electron traps are saturated, any additional extra electrons must combine with holes in either the valence band or in a hole trap, progressively reducing the net hole population without any corresponding reduction in the trapped electron population. In this scenario, the trapped hole population will eventually

decrease to zero; thereafter excess (untrapped) electrons entering the grain presumably either migrate to the surface of the grain and escape, or remain in the grain, with corresponding further increase in internal stress. Reports from the gemstone industry indicate that if this process is allowed to continue, these stresses can be sufficient to crack or explode the silicate mineral undergoing irradiation (e.g. topaz, as described in Nassau, 1985).

Qualitatively this mechanism leads to testable predictions concerning luminescence production. In low-energy electron irradiation, it is expected that, at very high doses, the trapped hole population would decrease, leading to fewer recombination sites. During subsequent optical stimulation, this would in turn lead to a decrease in the recombination rate with dose, and an increase in the rate of electron retrapping. The reduction in recombination rate would lead to a decrease of both absolute luminescence output and probably also of the subsequent luminescence sensitivity. The increase in retrapping rate would result in a corresponding slower decay of the OSL curve with stimulation time when comparing the shapes before and after a large dose.

### 4.2.2 Positive net charge

In the case of internal radioactivity, each $\beta^-$ decay with sufficient electron energy to leave the grain will leave behind a positively charged atom due to charge conservation. The mean $^{40}$K beta energy is 0.51 MeV, corresponding to a range of $\sim$800 µm in quartz; thus, most electrons generated by $^{40}$K decay will leave a sand-sized grain. For widely separated (i.e. low concentration) K-feldspar grains contained in a low activity matrix (e.g. quartz sand), where the internal $^{40}$K beta decay dominates the feldspar grain dose rate, there will only be a very small flux of scattered electrons entering the grain. Then the flux of electrons leaving the grain will not be balanced by electrons entering the grain, resulting in a net positively charged ($n_e < n_h$) grain.

The accumulation of excess holes will eventually saturate all hole traps, and lead to a concentration of holes in the valence band. These may then recombine directly with trapped electrons (normally an extremely low probability event) decreasing the absolute luminescence intensity as the trapped electron population decreases. However, in contrast to the situation with an excess of electrons, an excess of holes could lead to either increased or decreased luminescence sensitivity, as measured after stimulation of the electrons remaining after the acquisition of a very large dose. The number of trapped holes available for recombination with the electrons from a test dose would be very large, but the probability of a recombination leading to photon production would depend on the ratio at saturation of the lu-

minescent and non-luminescent hole populations. In the case of electron irradiation, it is possible to imagine mechanisms by which charge may leak from the conduction band to the grain surface, and so to the surrounding environment; this requires that the electron has at least enough energy to overcome the electron affinity (approx. 1 eV). Such processes must take a significant period of time (otherwise the observations of beam deflection and gemstone fragmentation discussed above would not be possible), and it seems reasonable that electrons could be trapped in this time. In this article, we are concerned with the behaviour of electrons after they have been trapped.

In the following sections, we test the qualitative predictions made above under the conditions of net negative charge, using a radiation transport model (Geant4) to quantify the electron population predictions. These predictions are then compared with the result of experiments.

## 4.3 Radiation transport modelling

### 4.3.1 Modelling setup

To simulate dose rates in nature and charge imbalance in individual grains, we use Geant4 (Agostinelli et al., 2003; Allison et al., 2006). This has previously been used to model dose rates to sand-sized grains in nature (Guérin, 2011; Guérin et al., 2012, 2015) and in the laboratory (Greilich et al., 2008; Chapter 2: Autzen et al., 2017) as well as to model electron-hole pair generation (Kovalev et al., 2015). Here, we use the Penelope physics model for electromagnetic interactions and a 40 eV production and tracking cut-off (corresponding to a range of $\ll$ 1 µm in quartz); at this energy the particle is considered stopped and its energy is deposited locally. It is recognised that even this cut-off is well above the 1 eV electron affinity of quartz, suggesting that, at least in principle, an electron with the cut-off energy would still have enough energy to escape from the conduction band to the grain surface. However, the range of even a 10 keV electron in quartz is $\sim$1 µm; such electrons would be unable to reach the grain surface from more than 88% of the volume of a 50 µm diameter grain; given the very much shorter range of an electron reaching the cut-off energy of 40 eV, we presume that effectively all such electrons would thermalise to the bottom of the conduction band and be unable to reach the grain surface.

During these simulations, for every 100,000 particles emitted by the source, we record

(i) the energy deposited in the grain

(ii) the number of electrons entering the grain

(iii) the number of electrons leaving the grain

(iv) the number of electrons generated inside the grain by ionisation.

(i) is needed to determine the dose and dose rate that the grain experiences under different conditions; we use these values to compare our simulation results with published infinite matrix dose rates (Guérin et al., 2012) and measured laboratory dose rates. The difference between (ii) and (iii) gives the net charge in the grain. The number of electron-hole pairs generated (iv) can be compared with the ionisation rate used by Bailey (2001, 2004) and Pagonis et al. (2007, 2008). See Figure 4.2 for additional information on the individual irradiation geometries.

Modelling the response of a 50 µm diameter spherical quartz grain with no internal radioactivity was undertaken for several geometries: (i) in a quartz matrix (emitters: $^{40}$K, see Figure 4.2a), (ii) quartz grains mounted on a stainless-steel disc or in an aluminium single grain disc irradiated by a $^{90}$Sr/$^{90}$Y beta source (Figure 4.2b and Figure 4.2c, respectively), and (iii) quartz grains on a stainless-steel disc irradiated by an electron beam (Figure 4.2d). Each of the simulation geometries are described in detail in the SMC4.

### 4.3.2 Modelling Results and Discussion

The results are presented in Table 4.1. The ratios of dose rate in Table 4.1 show that the relevant simulated dose rates are all very similar (Table 4.1, row 1) to those from direct calibration of the reader and those from infinite matrix dose rates (Guérin et al., 2012). The electron-hole pair generation rates per Gy (Table 4.1, row 2) are also very similar for the different irradiation geometries. However, the most interesting result of the modelling is that, in all geometries, more electrons enter the grain than leave (Table 4.1, row 3) i.e. the ratio $\frac{n_e}{n_h} > 1$ and so the grain acquires a net negative charge. While the extra electrons only contribute between 1.4-2.9% of the total number of electrons deposited per Gy, these electrons have no corresponding holes and thus presumably accumulate with dose/time.

Using trap concentrations from Bailey (2004), it is estimated that it will require $\sim$ 130 kGy to fill all of the electron traps and $\sim$5 MGy to recombine and so eliminate all the trapped holes. We would thus expect the population of trapped electrons to initially increase with dose and subsequently saturate when all the traps have been filled. The presence of extra electrons means that the hole population will always be a few % smaller than the electron population. Once the electron traps have all been filled, the trapped hole

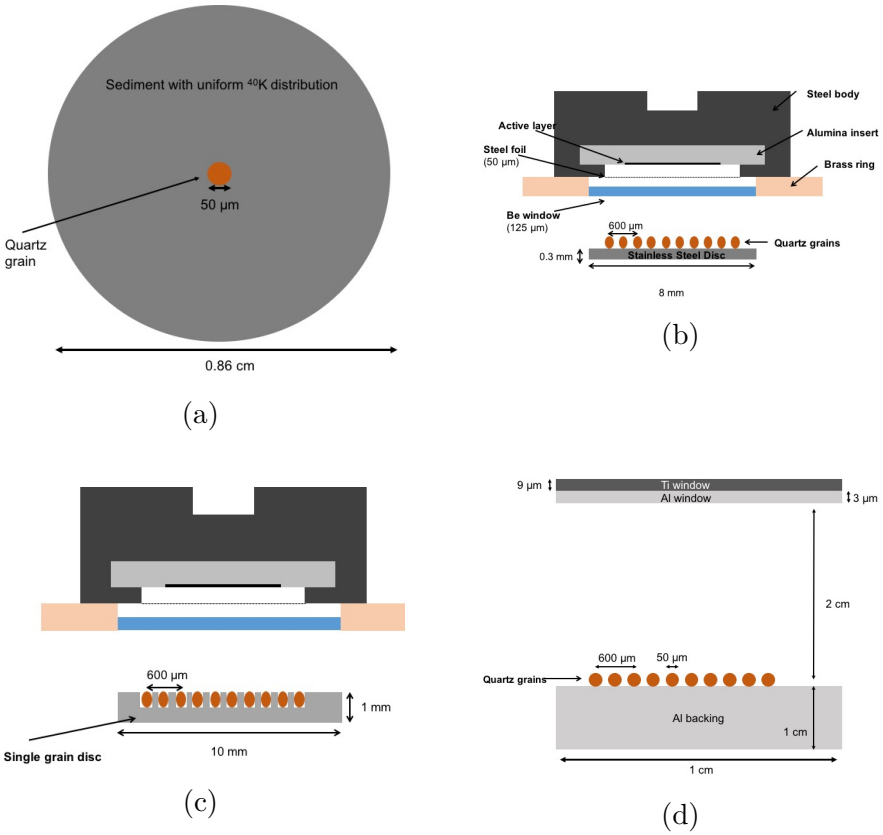


Figure 4.2: a) Irradiation of a 50 µm quartz sphere sitting in sediment matrix with uniformly distributed $^{40}$K emitters. b) Irradiation of 50 µm quartz spheres on a stainless steel disc in the Risø TL/OSL reader. c) Irradiation of 50 µm quartz spheres in a single grain disc. d) Irradiation of 50 µm quartz spheres in the electron beam.

population should then decrease linearly as extra electrons continue to be added to the grain. This model prediction is illustrated in Figure 4.3. In practice, other effects, such as charge repulsion, presumably become significant as the grain accumulates more and more net negative charge, and so the prediction of a linear decrease is likely to be simplistic.

Accumulated doses of this order can be achieved over geological timescales. For example, in a granite with a dose rate of 5 Gy ka$^{-1}$ it would take $2.6\times10^{7}$ years and $10^{9}$ years to give 130 kGy and 5 MGy to a quartz grain, respectively. Doses of several tens to hundreds of kGy are not practical using our beta or gamma sources but they can be achieved using an electron beam. The model comparison between a 1.48 GBq beta source and a 200 keV electron beam is shown in Table 4.1. The total number of electron-hole pairs

Table 4.1: Predictions of GEANT4 modelling of irradiations. Note: a) Ratio to calibrated dose rate using calibration quartz (Hansen et al., 2015) b) Ratio to simulated dose rates in Guérin et al. (2012)

| | TL/OSL Reader Source: 1.48 GBq | | $^{40}$K 600 Bq/kg | Electron Beam 200 keV |
|---|---|---|---|---|
| | Stainless Steel disc | Single Grain disc | Sediment | |
| Ratio of dose rates (Model to Experiments) | $1.03 \pm 0.03^a$ | $0.971 \pm 0.009^a$ | $1.02 \pm 0.02^b$ | |
| Electron/Hole pairs generated $[Gy^{-1}]$ | $(81.1 \pm 0.5) \times 10^3$ | $(81.3 \pm 0.4) \times 10^3$ | $(82.3 \pm 1.2) \times 10^3$ | $(84.0 \pm 1.3) \times 10^3$ |
| Excess electrons $[Gy^{-1}]$ | $(2.37 \pm 0.05) \times 10^3$ | $(1.53 \pm 0.04) \times 10^3$ | $(2.16 \pm 0.13) \times 10^3$ | $(2.53 \pm 0.1) \times 10^3$ |
| Fraction of total electrons | $2.49 \pm 0.17\%$ | $1.41 \pm 0.16\%$ | $2.63 \pm 0.14\%$ | $2.93 \pm 0.14\%$ |

generated per unit dose delivered by the electron beam are similar to that calculated for the beta source. but because the range of the electrons in quartz (80 µm) is comparable to the grain size (50 µm) the extra electrons (net charge) make up a larger fraction of the total.

In the next sections the model prediction shown in Figure 4.3 is tested experimentally.

## 4.4 Materials and Methods

### 4.4.1 Instrumentation

Irradiations were carried out using:

- Risø TL/OSL DA-20 readers each fitted with a $^{90}$Sr/$^{90}$Y beta source ($\bar{E} = 523$ keV) of activity either 1.48 GBq or 3 GBq. Prior to irradiation, grains were mounted as a mono-layer on 0.3 mm thick stainless-steel discs using silicone oil.

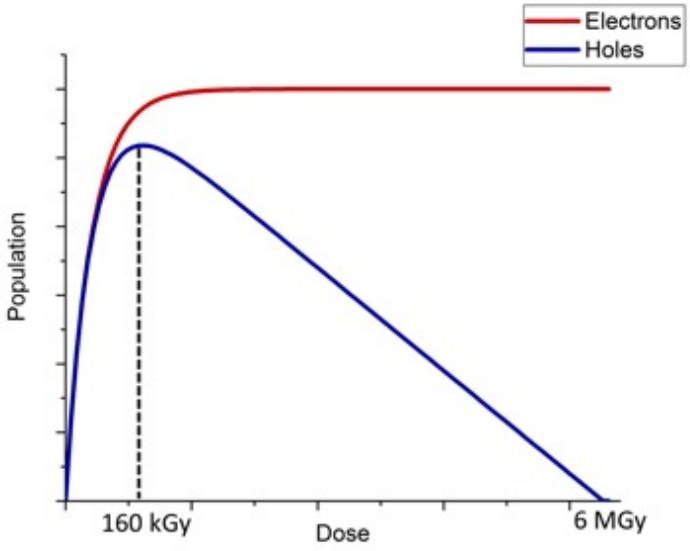


Figure 4.3: Model prediction of the trapped electron population (red curve) and hole population (blue curve) in quartz when considering charge imbalance with excess electrons.

- A Comet EBLab-200 electron beam. Mono-energetic 200 keV electrons (range $\sim 80\,\mu m$ in quartz) are emitted from a hot wire through titanium and aluminium windows to give very large dose rates at the sample position; here we have used 50 kGy $s^{-1}$. The stainless-steel discs containing the grains were placed on a tray which moved through the electron beam under a constant air flow to minimise temperature increase.

The dose rate delivered by the electron beam is $\sim 10^4$ times larger than that of the normal $^{90}Sr/^{90}Y$ beta source, and so dose rate effects (Chen and Leung, 2001) may play role in the luminescence response. On the other hand, the beta source dose rate is $\sim 10^{10}$ times larger than typical natural dose rates and yet it is still possible to measure ages to within at least 10% accuracy using OSL signals. It thus seems reasonable to assume that dose rate effects in comparing a beta source irradiation with electron beam irradiation are unlikely to be large.

### 4.4.2 Samples

Quartz extracts from two loess deposits were used to test model predictions; (i) a Chinese loess sample (sample H28112) from Stevens et al. (2016) and

(ii) a composite sample of different portions of Serbian loess from a site on the Titel Loess Plateau (Marković et al., 2015). Based on initial modelling of the electron beam, a target grain size of 50 µm was chosen because this allows full penetration of the grain by 200 keV electrons while still stopping a majority of lower energy electrons. Extracts were sieved to $40 - 63$µm before treatment with hydrochloric acid (HCl, 10 %), hydrogen peroxide ($H_2O_2$, conc.) to remove any carbonates and organic matter and etching with 40% HF to remove any feldspars. Finally, the samples were sieved again to $> 40$ µm to ensure a controlled grain size fraction.

The Chinese loess sample was pre split into two batches of which one was sensitised as described in Hansen et al. (2015), resulting in three samples for the experiment, namely Chinese loess, sensitised Chinese loess and Serbian loess. A total of 120 aliquots of each sample were prepared and the stability of the sample sensitivity after several $L_x/T_x$ cycles was checked (Figure 4.6) using the SAR protocol listed in Table 4.2a. The stabilised OSL sensitivity (Tx) of each aliquot to a beta test dose of 3 Gy was measured before electron beam irradiation.

Aliquots were arranged in 10 groups of 12 aliquots per sample. Each group was split equally between two aluminium trays, one sitting on a Perspex backing to preventing electrical grounding and another sitting on top of an aluminium backing and so connected to earth. The aliquots were each given a dose of 100 kGy per irradiation and 24 aliquots of each sample (12 per substrate) were removed after cumulative doses of 100 kGy, 300 kGy, 700 kGy, 1.9 MGy, and 5 MGy. Note that all of these doses are presumed to be sufficient to completely saturate the OSL trap(s). The aliquots were stored in the dark at $-18$ °C until all irradiations were complete.

The OSL measurements following the electron beam irradiation (Table 4.2b) were carried out on the same TL/OSL DA-20 readers as had been used prior to the electron beam to avoid introduction of extra uncertainties. To ensure that as much of the signal as possible was recorded and there were no more exponentially decaying components, the response to the electron beam ($OSL_1$ and $OSL_2$) was stimulated for 100 seconds. For all OSL records the channel width was kept constant. OSL signals were integrated from 1 to 98 s minus a background of 98 to 100 s (response to electron beam, $OSL_1$ and $OSL_2$) and 1 to 38 s minus a background of 38 to 40 s (response to beta test dose, $OSL_3$).

Table 4.2: Luminescence measurement sequences

(a) Luminescence measurement sequence prior to e-beam irradiation

| Step | Treatment | Observation |
|---|---|---|
| 1 | Dose, 6 Gy | |
| 2 | Preheat: 260 °C for 10s | |
| 3 | OSL at 125 °C, 40 s | $L_x$ |
| 4 | Test dose, 3 Gy | |
| 5 | TL to 220 °C | |
| 6 | OSL at 125 °C, 40 s | $T_x$ |
| 7 | OSL at 280 °C, 40 s | |
| 8 | Return to 1 | |

(b) Luminescence measurement sequence after to e-beam irradiation

| Step | Treatment | Observation |
|---|---|---|
| 1 | TL to 150 °C | |
| 2 | OSL at 125 °C, 100 s | $OSL_1$ |
| 3 | TL to 150 °C | |
| 4 | OSL at 125 °C, 100 s | $OSL_2$ |
| 5 | Test dose, 3 Gy | |
| 6 | TL to 150 °C or220 °C | |
| 7 | OSL at 125 °C, 40 s | $OSL_3$ |

## 4.5 Experimental results

No difference could be detected between results obtained using the aluminium and Perspex substrates during electron beam irradiations and so the results have been combined (see Figure 4.7 for a comparison of signals from irradiations on Al and Perspex). The results are summarised in Figure 4.4a, where the net OSL counts ($OSL_1$ in Table 4.2) are shown, averaged over all 24 aliquots at each dose point. The OSL signal increases for each of the three samples until a given dose of between 300 and 700 kGy, after which the signal decreases with dose. The peak in response occurs at a slightly lower dose (∼300 kGy) in the Serbian loess extract, whereas the response of both the natural and sensitised Chinese loess extracts peaks at ∼700 kGy.

The OSL response to the electron beam irradiation was measured twice ($OSL_1$ and $OSL_2$) to ensure that the subsequent $OSL_3$ (response from the

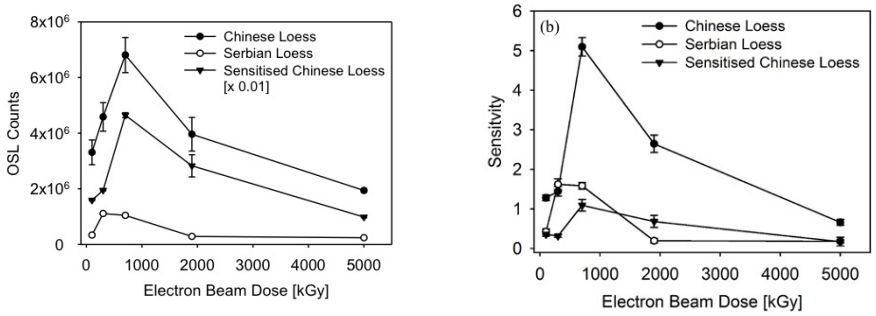


Figure 4.4: a) Average background corrected total OSL signal ($OSL_1$) as a function of electron beam dose. b) Ratio of test dose sensitivity before and after electron beam irradiation (ratio of $T_x/OSL_3$) as a function of electron beam dose. Error bars represent one s.e.

test dose) was unaffected by any residual from the preceding large dose (Table 4.2b). Figure 4.4b shows the change in test-dose response (ratio $T_x$ to $OSL_3$) as a result of the electron beam irradiation and subsequent OSL measurements. The shape of this OSL sensitivity change is similar to that of the response to the electron beam irradiation. Figure 4.5a presents the normalised average OSL response to the 3 Gy beta dose for all the Serbian loess aliquots before ($L_x$) and after ($OSL_1$) being given 100 kGy (the smallest dose) in the electron beam. Figure 4.5b summarises similar data, but for the aliquots given 5 MGy (the largest dose) in the electron beam. A normalised decay curve of standard calibration quartz (Hansen et al., 2015) is also shown for comparison.

In Figure 4.5a, the decay rates of the response before and after the 100 kGy dose are similar for the first 0.5 s of simulation; after 0.5 s the post 100 kGy signal appears to be decay more slowly. For the 5 MGy dose, the decay rate is always slower than the pre-5 MGy signal. If the hole population has indeed decreased significantly as a result of charge imbalance within the grains at high doses, then competition between recombination and retrapping would become more important. As retrapping probability increases, it is expected that the decay rate of the OSL stimulation curve decreases.

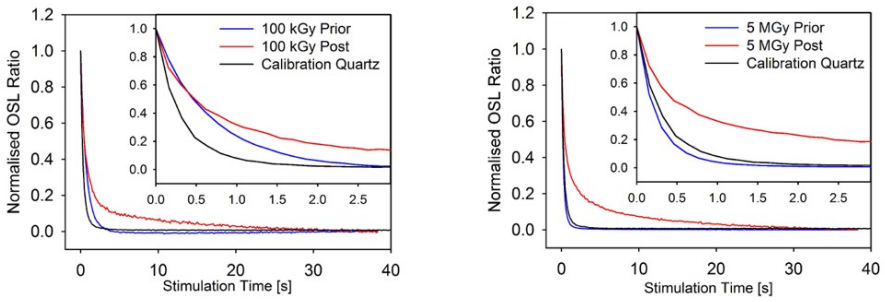


(a) (b)

Figure 4.5: a) Normalised background corrected OSL decay curve for Serbian loess for 100 kGy electron beam dose. Inset magnifies the first 2.5 s of the decay. b) Normalised background corrected OSL decay curve for Serbian loess for 5 MGy electron beam dose. Inset magnifies the first 2.5 s of the decay. Each signal is normalised to the first point. A normalised calibration quartz decay curve is shown for comparison.

## 4.6 Discussion

Using modelling we have shown that during irradiation of quartz grains either in natural sediments or in the laboratory there is very likely to be a net excess of electrons entering the grain. As a result, we suggest that the net charge in the grain would become increasingly negative, and in extreme cases (very large doses, where all electron traps are saturated) the trapped hole population would begin to decrease. Figure 4.3 qualitatively illustrates the expected behaviour of trapped electrons and holes separately, whereas the experimental data presented in Figure 4.4 only reflect the radiative recombination probability(s). In these experiments, even the smallest electron beam irradiation (100 kGy) is presumed to saturate the OSL traps. Both Figures 4.4a and 4.4b are thus interpreted as reflecting, in practice, sensitivity change, i.e. the OSL response to a constant number of electrons in the OSL trap. Figure 4.4a shows the response when the OSL trap is saturated (following the large electron beam dose; presumably the number of electrons required to saturate the trap remains constant), and Figure 4.4b the response when the OSL trap contains only a small (but presumably fixed) number of electrons following the test dose. In this interpretation, the change in sensitivity shown in both figures arises from a change in hole population (the OSL recombination is presumed to recombine only a small fraction of the total hole population). This initially increases towards some saturation value as the total trapped electron population increases; when

the trapped electron population saturates, the hole population decreases as excess electrons resulting from the electron beam irradiations recombine with trapped holes, as predicted by the model (Figure 4.3).

While competition effects between luminescent and non-luminescent centres might also contribute to the decrease in sensitivity with dose, this mechanism does not explain the significant decrease in decay rate which occurs as the dose is increased (Figures 4.5a and 4.5b). This decrease is interpreted as resulting from an increase in retrapping in the electron traps, as the hole population decreases. Further measurements using exo-electron emission are planned to test this, as the exo-electron signal will not be affected by recombination pathways but only by the rate at which charge can be evicted from the conduction band.

Trap concentrations based on the model by Bailey (2004) were used to estimate the doses needed to fill all the electron traps and empty all the hole traps. From Bailey's trap concentrations and the rate at which electrons are entering the conduction band during irradiation (derived using our Geant4 modelling results) we would expect the peak in our data to be located around 130 kGy. In fact, we observe the peak between $300 - 700$ kGy which is within a factor $\sim 2 - 5$ of what was expected from Bailey's (2004) model. We consider this to be encouraging given that Bailey's (2004) trap concentrations resulted from simulation optimisation and do not necessarily reflect the actual trap concentrations; these may also vary considerably between samples. Nevertheless, we do observe that the OSL sensitivity, both at saturation and at low dose, follows the shape of that expected from modelling the hole population changes with dose.

We do not regard our experiments as conclusive evidence that excess electrons modify luminescence behaviour; we have not, for instance, considered the possible effects of trap creation, and dose dependent changes in ionisation rates. Nevertheless, we note that our results are broadly consistent with model predictions. In future work we will combine Geant4 results with luminescence models to quantitatively predict the impact of charge imbalance on luminescence response at small and moderate doses.

## 4.7 Conclusion

Using modelling we have demonstrated that the assumption of charge neutrality is not justified at the scale of sand-sized grains of quartz, either in nature or in the laboratory. The luminescence implications of this charge transport modelling were tested using a low energy electron beam in order to maximise any charge imbalance; the effect on luminescence production

were investigated with OSL. Our data suggests that charge imbalance does exist and affects luminescence production at high doses. Although it may be possible to explain the behaviour of the luminescence response by competition between non-luminescent and luminescent centres (although this has not been shown), such an explanation does not explain the apparent slower OSL decay rates at higher doses.

**Acknowledgements:** M. Autzen, and J.P. Buylaert receive funding from the European Research Council (ERC) under the European Union's Horizon 2020 research and innovation programme ERC-2014-StG 639904-RELOS. The authors would also like to thank Louise M. Helsted, Vicki Hansen, Gabor Ujvari and Warren Thompson for help in preparing samples as well as Arne Miller for lending us the electron beam

## 4.8 Supplementary Material for Chapter 4

### 4.8.1 Modelling Setup

#### $^{40}$K irradiation

Modelling of natural dose and charge deposition due to $\beta^-$ decay from $^{40}$K was carried out using a 0.86 cm diameter sphere containing quartz and a density of 1.8 g cm$^{-3}$ to account for the loose packing of grains. In the centre of the sediment sphere, a 50 µm diameter quartz sphere is placed which is used as the detector, and as a proxy for quartz grains in a natural environment. The energy deposited in the quartz grain as well as the electrons crossing the grain boundary in either direction and the electrons generated inside the grain due to ionisation are all recorded separately for 100,000 decays in the surrounding sediment. $^{40}$K decays are simulated by releasing an electron from a uniformly distributed random position in the sediment, outside the grain, and sampling the $^{40}$K beta spectrum for an energy. Electrons released in this way are then given a momentum vector, which uniformly samples the entire $4\pi$ geometry to account for any potential backscattering of electrons. The sediment radius is equal to the maximum range of the electrons from the potassium beta spectrum.

#### Risø TL/OSL Reader irradiations

This simulation has been described previously in Chapter 2 (Autzen et al., 2017). The geometry is modelled after the Risø TL/OSL flange (Dalsgaard, private communication) with grains located in a 10x10 grid spaced with a 300 µm centre-to-centre distance. The grains are located either sitting on top of a 0.3 mm thick stainless steel disc (Figure 4.2b) or sitting at the bottom of cylindrical holes in an aluminium disc (diameter/height: 300 µm, i.e. Risø single-grain disc; Figure 4.2c). These holes are located at the centre of each point on the 10x10 grid. The grains are all 50 µm diameter quartz spheres. The particles are released in the same manner as the previous simulation but are confined to the source disc illustrated in Figure 4.2b and Figure 4.2c. In these two simulations, the combined beta spectrum for the $^{90}$Sr/$^{90}$Y beta source is used to sample the energy of the emitted particles.

#### Electron Beam irradiations

The electron beam is simplified for this model. It is approximated as a cylinder (Radius: 1 cm, Height: 2.0012 cm) with a 3 µm thick Al window (Radius: 1 cm) ending at 2 cm above the substrate holding the grains.

Above this Al window sits a 9 µm thick Ti window (Radius: 1 cm) which fills the gap between the top of the model and the Al window. Two cm below the bottom of the Al window is a 1 cm thick Al substrate on top of which the 50 µm diameter grains sit in the same 10 x 10 grid used in the Risø TL/OSL reader simulations. The electrons are released with a set energy of 200 keV and only a z-component to their momentum. This simplification can be justified by the fact that the actual electron beam is several times larger than the distance from the release to the sample.

### 4.8.2 Experimental Details

A single 8 mm aliquot of each sample was tested using a SAR protocol (Murray and Wintle, 2003) for stability and purity. Aliquots were preheated to 260 °C for 10 s and stimulated at 125 °C for 40 s for the natural and $L_x$ measurements (using a 6 Gy dose). $T_x$ measurements were completed using a 3 Gy dose, followed by TL to 220 °C and stimulated at 125 °C for 40 s before a 280 °C blue-light bleach. This was repeated 21 times. On cycles 2,4,6,10,14, and 18, IR stimulation at 60 °C for 100 s preceded the 125 °C stimulation with blue LEDs to derive an OSL IR depletion ratio (Duller, 2003). From Figure 4.6 it can be seen that the samples do not contain a significant IR sensitive component, (i.e. no significant drops in $L_x/T_x$ ratio on cycles 2,4,6,10,14, and 18) and stability in the luminescence response was achieved.

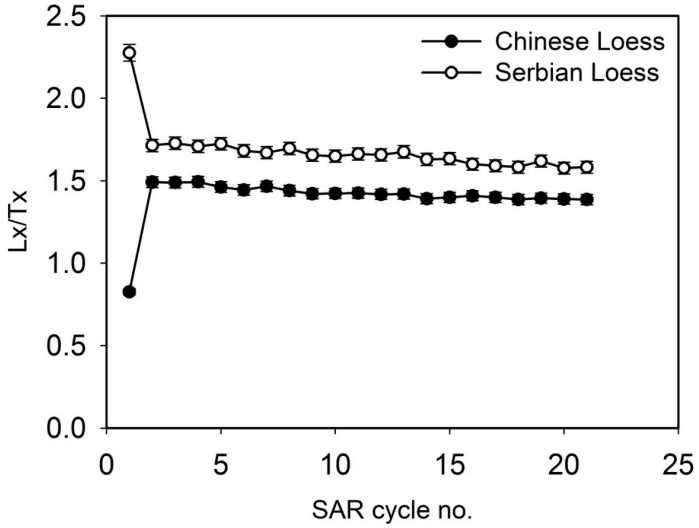


Figure 4.6: Stability and purity check of samples used in the experiments

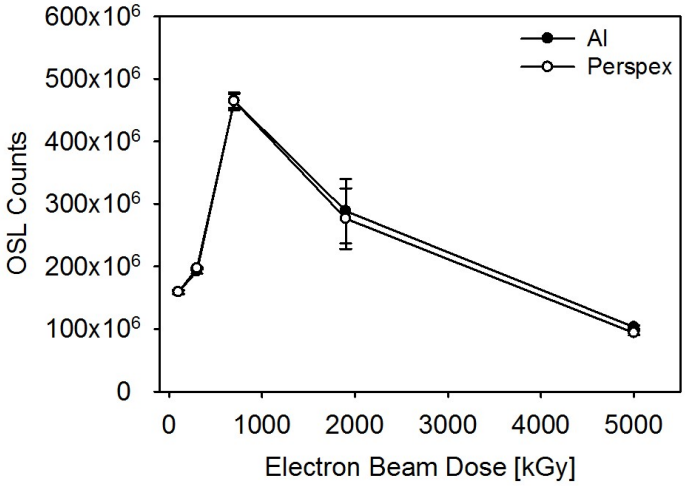


Figure 4.7: Post electron beam total OSL response ($OSL_1$) for the Sensitised Chinese Loess. The closed circles show the response from the aliquots irradiated on a grounded Al plate, the open circles show the response from the aliquots irradiated on a Perspex plate.

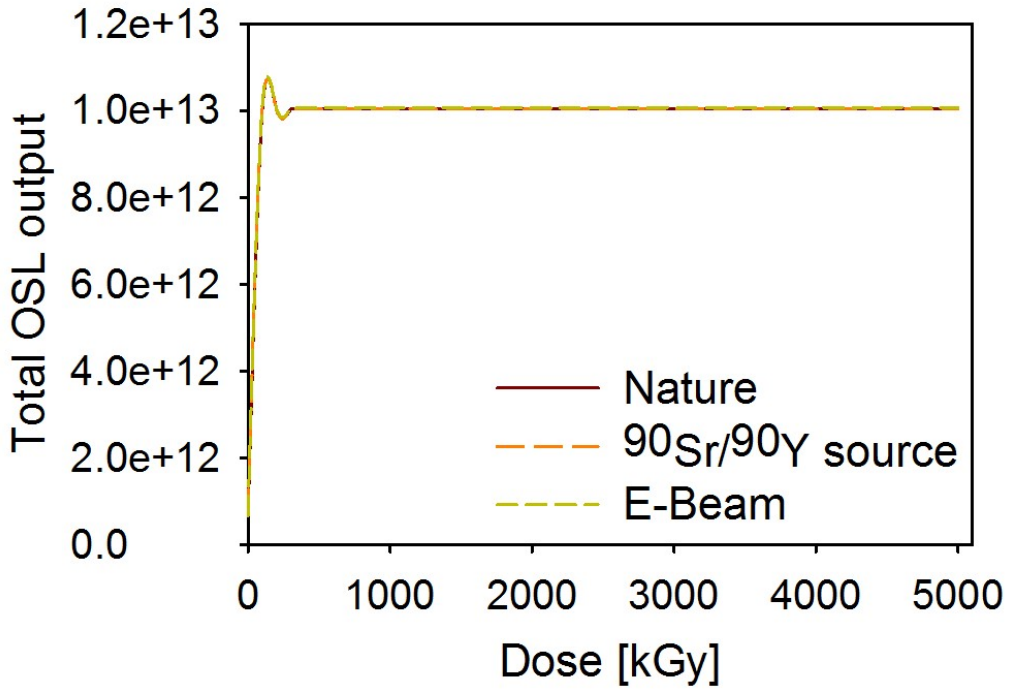


Figure 4.8: OSL output from the electron beam with charge neutrality modelled using luminescence production equations (Bailey, 2004; Pagonis, 2007) for natural irradiation (1 Gy/ka), $^{90}$Sr/$^{90}$Y beta source irradiation (0.1 Gy/s) and the Comet EBLab-200 electron beam (50 kGy/s). No difference is observed for the different dose rates.

# References

Adamiec, G., Garcia-Talavera, M., Bailey, R.M., Iniguez de la Torre, P., Application of a genetic algorithm to finding parameter values for numerical simulations of quartz luminescence. *Geochronometria.* 2004:**23**:9-14

Adamiec, G., Bluszcz, A., Bailey, R., Garcia-Talavera, M. Finding model parameters: genetic algorithms and the numerical modelling of quartz luminescence. *Radiation Measurements.* 2006:**41**:897-902

Agostinelli, S., Allison, J., Amako, K., Apostolakis, J., Araujo, H., Arce, P., et al., (Geant4 Collaboration). Geant4 ,Äì a simulation toolkit *Nuclear Instruments and Methods in Physics Research Section A.* 2003:**506(3)**;250-303

Allison, J., Amako, K., Apostolakis, J., Araujo, H., Arce, P., Asai, M., et al., (Geant4 Collaboration). Geant4 development and applications. *IEEE Transactions on Nuclear Science.* 2006:**53(1)**;270-278

Ankjærgaard C., Murray A.S., Denby P.M., Bøtter-Jensen L. Measurement of optically and thermally stimulated electron emission from natural minerals. *Radiation Measurements.* 2006;**41(Sp. Iss.)**:780-786

Ankjærgaard C., Denby P.M., Murray A.S., Jain M. Charge movement in grains of quartz studied using exo-electron emission. *Radiation Measurements.* 2008;**43(2-6)**:273-277

Ankjærgaard C., Murray A.S., Denby P.M., Jain M. Using optically stimulated electrons from quartz for the estimation of natural doses. *Radiation Measurements.* 2009;**44(3)**:232-238

Autzen M., Guérin G., Murray A. S., Thomsen K. J., Buylaert J.-P., Jain, M. The effect of backscattering on the beta dose absorbed by individual quartz grains. *Radiation Measurements.* 2017:**106**:491-497

Bailey, R.M. Towards a general kinetic model for optically and thermally stimulated luminescence of quartz. *Radiation Measurements.* 2001:**33**:17-45

Bailey, R.M. Paper I - simulation of dose absorption in quartz over ge-

ological timescales and its implications for the precision and accuracy of optical dating. *Radiation Measurements.* 2004:**38**;299-310

Bøtter-Jensen, L., McKeever, S.W.S, Wintle, A.G. Optically Stimulated Luminescence Dosimetry. 2003. (Amsterdam: Elsevier) Chapter 2

Cazaux J. Scenario for time evolution of insulator charging under various focused electron irradiations. *Journal of Applied Physics.* 2004:**95**:731

Chen, R., Leung, P.L. Nonlinear dose dependence and dose-rate dependence of optically stimulated luminescence and Thermoluminescence. *Radiation Measurements.* 2001:**33**:475-481

Dalsgaard, S. Private communication. 2017

Duller, G.A.T. Distinguishing quartz and feldspar in single grain luminescence measurements. *Radiation Measurements.* 2003:**37(2)**:161-165

Frederickson, A. R. Upsets Related to Spacecraft Charging. *IEEE Trans. Nucl. Sci.* 1996:**43(2)**:426-441

Galbraith, D. M., Rawlinson, J. A., Munro, P. Dose errors due to charge storage in electron irradiated plastic phantoms. *Med. Phys.* 1984:**11(2)**:197-203

Greilich, S., Murray, A.S., Bøtter-Jensen, L. Simulation electron transport during beta irradiation. *Radiation Measurements.* 2008:**43(2-6)**;748-751

Gross, B. Irradiation Effects in Borosilicate Glass. *Physical Review.* 1957:**107(2)**:368-373

Gross, B. Irradiation Effects in Plexiglas. *Journal of Polymer Science.* 1958:**27**:135-143

Guérin, G. Modélisation et simulation des effects dosimétriques dans les sédiment quaternaires : application aux méthodes de datation par luminescence (PhD thesis) Université Bordeaux, 2011

Guérin, G., Mercier, N., Nathan, R., Adamiec, G., Lefrais, Y., 2012. On the use of the infinite matrix assumption and associated concepts: a critical review. *Radiation Measurements.* 2012:**47(9)**;778-785.

Guérin, G., Jain, M., Thomsen, K.J., Murray, A.S., Mercier, N., Modelling dose rate to single grains of quartz in well-sorted sand samples: The dispersion arising from the presence of potassium feldspars and implications for single grain OSL dating. *Quaternary Geochronology.* 2015:**27**;52-65

Hansen, V., Murray, A., Buylaert, J.P., Yeo, E.Y., Thomsen, K. A new irradiated quartz for beta source calibration. *Radiation Measurements.* 2015:**81**;123-127

Kovalev, I. V., Electron-hole pairs generation rate estimation irradiated by isotope Nickel-63 in silicone using Geant4. *IOP Conf. Ser.:Mater.Sci.Eng.* 2015:**94**:012024

Lam, H.-L., Boteler, D. H., Burlton, B., Evans, J. Anik-E1 and E2 satellite failures of January 1994 revisited. *Space Weather.* 2012:**10**:S1003

Marković, S.B., Stevens, T., Kukla, G. J., Hambach, U., Fitzsimmons, K. E., Gibbard, P., Buggle, B., Zech, M., Guo, Z. , Qingzhen, H., Haibin, W., Dhand, O. K., Smalley, I. J., Gábor, U., Sümegi, P., Timar-Gabor, A., Veres, D., Sirocko, F., Vasiljević, D. A., Jary, Z., Svensson, A., Jović, V., Lehmkuhl, F., Kovács, J., Svirčev, Z. Danube loess stratigraphy - Towards a pan-European loess stratigraphic model. *Earth Science Reviews* 2015:**148**; 228-258

Mattsson, L. O., Svensson, H. Charge build-up effects in insulating phantom materials. *Acta Radiologica Oncology.* 1984:**23**:393-399

McLaughlin, W. L. Radiation Processing Dosimetry. *Radiat. Phys. Chem.* 1983:**21(4)**:359-366

Murray, A.S., Wintle, A.G., 1999. Isothermal decay of optically stimulated luminescence in quartz.*Radiation Measurements.* 1999:**30**;119-125.

Murray, A., and Wintle, A. The single aliquot regenerative dose protocol: Potential for improvements in reliability. *Radiation Measurements.* 2003:**37(4-5)**;377-381.

Nassau, K. Altering the Color of Topaz, *Gems and Gemology.* 21, No. 1, 26 (1985)

Pagonis, V., Chen, R., Wintle, A.G., Modelling thermal transfer in optically stimulated luminescence of quartz. *Journal of Physics D: Applied Physics*. 2007:**40**:998-1006

Pagonis, V., Wintle, A.G., Chen, R., Wang, X.L. A theoretical model for a new dating protocol for quartz based on thermally transferred OSL (TT-OSL). *Radiation measurements*. 2008:**43**:704-708

Rawlinson, J. A., Bielajew, A. F., Munro, P., Galbraith, D. M. Theoretical and experimental investigation of dose enhancement due to charge storage in electron-irradiated phantoms. *Med. Phys.* 1984:**11(6)**:814-821

Stevens, T., Buylaert, J.-P., Lu, H., Thiel, C., Murray, A., Frechen, M., Yi, S., Zeng, L. Mass accumulation rate and monsoon records from Xifeng, Chinese Loess Plateau, based on a luminescence age model. *Journal of Quaternary Science*. 2016:**31**:391-405.

Stevens Kalceff M.A., Phillips M.R., Moon A.R. Electron irradiation-induced changes in the surface topology of silicon dioxide. *Journal of Applied Physics*. 1996:**80**:4308.

Tanaka, R., Sunaga, H., Tamura, N. The effect of accumulated charge on depth dose profile in poly(methylmethacrylate) irradiated with fast electron beam. *IEEE Trans. Nucl. Sci.* 1979:**NS-26(4)**:4670-4675

Tsukamoto S., Murray A.S., Ankjærgaard C., Jain M., Lapp T. Charge recombination processes in minerals studied using optically stimulated luminescence and time-resolved exo-electrons. *Journal of Physics D: Applied Physics*. 2010;**43(32)**:325502

Vigouroux, J.P., Duraud J.P., Le Moel A., Le Gressus C., Griscom D.L. Electron trapping in amorphous SiO2 studied by charge buildup under electron bombardment. *Journal of Applied Physics*. 1985;**57**:5139

Wolff, P.A., Theory of Electron Multiplication in Silicon and Germanium. *Physical Review*. 1954:**95(6)**:1415-1420

Zheng, F., Zhang, Y., Xiao, C., Xia, J., An, Z. Effect of Applied Mechanical Stress On Space Charge Breakdown in Electron Beam Irradiated Polymethyl Methacrylate. *IEEE Trans. Dielect. Elect. Insul.* 2008:**15(4)**:965-973

# Chapter 5

# The history of charge deposition in quartz and its effect on luminescence production

---

**Abstract:** We use both modelling and high dose experiments to investigate the effects of charge imbalance on luminescence by expanding on our previous work. Modelling predicts that that excess charge varies as a function of grain size in both natural and laboratory irradiations. Small grains ($\sim 5\,\mu m$) appear to have a largest excess of electrons and as the grain size increases this excess appears to plateau around 2%. For small grains, this charge excess is not identical in natural and laboratory irradiations. Furthermore, it is predicted that irradiating 100 µm quartz sheets with a $^{137}Cs$ source results in a no significant excess charge. These modelling results are for the first time used as input to luminescence production models. These models shows that while the trapped electron populations are not significantly affected by excess electrons, the trapped hole populations decrease linearly with dose once all the electron traps have been saturated. These effects are tested by irradiating quartz aliquots to high doses (hundreds of kGy to MGy) with a high dose resolution and different electron energies (100 and 200 keV). We find that the luminescence output and sensitivity decreases with dose, however, the decrease is not linear and shows an energy dependence. We hypothesise that this non-linear decrease is the result of the excess electrons populations becoming sufficient to repel the incoming electrons at high doses and effectively stop the dosing completely.

## 5.1 Introduction

Luminescence is widely used to estimate the dose absorbed during burial in natural minerals (e.g. quartz and feldspars) because they store separated charge (electrons and holes) when exposed to ionising radiation. The recombination of these charges can then be used to estimate the absorbed dose by comparison with exposure to a source of known dose rate. However, this comparison requires that the total number of charges deposited in the dosimetry trap per unit dose is identical in the initial exposure geometry and during the subsequent controlled irradiation. In a previous paper (Autzen et al, 2018; Chapter 4) we pointed out that sand-sized grains do not, in fact, remain charge neutral during exposure to particle radiation, as is commonly assumed in luminescence production models. If net charge builds up in traps there may no longer be a simple relationship between trap filling and dose deposited. We pointed to two separate scenarios, excess electrons and excess holes; in both cases, the symmetry between conduction and valence band filling is lost and should be reflected in the trapped charge populations even in the presence of direct conduction band charge leakage to and from the valence band. In the limit, it may then be possible for grains to have completely saturated electron (or hole) traps and have no trapped holes (or electrons), as well as any intermediate state.

There is considerable evidence in the literature of charge build up during the irradiation of non-conductors with electrons, from the fields of scanning electron microscopy (SEM), Auger electron microscopy (AEM), electron probe microanalysis (EPMA), electron spectroscopy chemical analysis (ESCA), secondary ion mass spectrometry (SIMS) and other analytical methods depending on particle irradiation (Le Gressus et al., 1990). One of the first studies of excess charge as a result of irradiation with charged particles was made by Gross (1957). He studied the build up of charge on borosilicate glass following irradiation with 2 MeV electrons and observed a change in the colour of the glass, corresponding to the creation of colour centres, which extended to a depth of 0.4 cm, equal to the penetration depth of the incoming electrons. Furthermore, electrical breakdown could be initiated after irradiation by touching the sample with a pointed (metal) conductor; this was accompanied by a flash of light and the creation of

a characteristic discharge pattern in a well-defined planar volume parallel to the irradiated surface centred on the point of contact. He also observed that such breakdown could be initiated several months after irradiation suggesting that the excess charge was stable on that timescale; nevertheless it could be removed by annealing to high temperatures. It was also suggested that the stored negative charge gave rise to a compensation charge at the unirradiated sample surface. These observations were further expanded by Gross and Wright (1959) who observed charge deposition curves in Plexiglass following irradiation by 3 MeV electrons. These experimental curves confirmed the existence of a charged layer in the dielectric, of thickness equal to the penetration depth of the incident electrons. It is even possible for the electrostatic potential of the implanted charge to increase during irradiation until the local field produced is sufficient to divert (or even stop) the incoming particles, producing a defocusing or bending of the beam by the sample (Reimer, 1985; Vigouroux et al., 1986).

While, from first principles, there seems little doubt that charge imbalance during particle (and possibly photon) irradiation must be commonplace, there is almost no information concerning the possible long-term accumulation of such charge imbalance in traps or of its effects, if any, on luminescence production. To our knowledge, Chapter 4 was the first study to address this explicitly, and there these issues were only discussed qualitatively. Here we expand on this previous pilot study by investigating the predicted charge imbalance under a variety of irradiation geometries, grain sizes and energies using Geant4. The output of this modelling is then used as input to the luminescence production equations of Bailey (2004; see also Pagonis, 2007, 2008) to investigate the effect the energy and charge deposition predictions might have on luminescence production. New experimental results are also provided; these expand on previous results by investigating the effects of irradiation with 100 keV and 200 keV electron beams on the luminescence production in quartz grains. Finally we discuss these observations in the light of the modelling predictions.

## 5.2 Modelling of dose deposition, charge imbalance and luminescence response

The modelling carried out for this paper is presented in three sections. The first two sections deal with dose deposition and charge imbalance under different conditions as predicted by the Geant4 toolkit (Agostinelli et al., 2003). We discuss the effects of grain size and spectrum on the dose de-

position and charge imbalance for external irradiations (beta irradiation in a Risø TL/OSL reader, electron beam irradiation, natural beta irradiation and irradiation in a calibration gamma source). In the third section, these results are used as input to a luminescence production model (Bailey, 2004; Pagonis, 2007, 2008) to model the effects of these irradiations on trapped charge populations for relevant experimental geometries and to predict the luminescence behaviour with dose.

### 5.2.1 External irradiation

External irradiations are of particular importance for quartz grains since quartz contains very low amounts of internal radioactivity, and thus beta dose and charge deposition are, during burial, dependent almost entirely on the secondary electron spectrum of the surrounding sediment, and in the laboratory, on the spectrum of the beta or gamma source used to provide the reference dose.

#### Natural beta irradiation

In nature, almost all dose originates with the decay of $^{40}$K, the $^{232}$Th series and the $^{238}$U series. This dose is deposited following $\gamma$-emission, electron emission ($\beta^-$ decay) or $\alpha$-emission. We focus primarily on $\beta^-$ decay; although $\alpha$-particles carry twice the charge of an electron (with opposite sign), their range is short and quartz grains are usually etched before use with the intention of removing the part of the grain exposed to this component.

The $\beta^-$ spectrum for $^{40}$K has a mean energy $\bar{E} = 560\,\text{keV}$ and a maximum energy $E_{max} = 1.311\,\text{MeV}$, resulting in a mean range greater than 0.8 mm in quartz. The mean energy for the U and Th series is much smaller, $\bar{E}$ ~180-240 keV corresponding to a mean range of 200 and 300 µm respectively. However, the maximum energy for both ($E_{max}$ ~3.3 MeV) is much greater; this gives a maximum range of ~7.3 mm in quartz.

The geometry used to simulate a quartz grain surrounded by radioactive sediment is shown in SMC5 Figure 5.16a. In this case, a 100 µm diameter spherical grain of quartz placed at the centre of a 86 mm diameter sediment sphere. Here the "sediment" is composed of quartz with a density of $1.78\,\text{g cm}^{-3}$ (to account for a typical packing density of spherical grains). A $\beta^-$ $^{40}$K spectrum is emitted uniformly throughout the sediment. In an identical simulation a combined U-Th $\beta^-$ spectrum, mixed in a 1:1 ratio, is also uniformly emitted. For both simulations, the spectrum of electrons entering the quartz grain is recorded and these spectra are then combined in a 15:1 ratio, corresponding to K:U:Th relative activities of $600{:}40{:}40\,\text{Bq kg}^{-1}$ (i.e. typical natural ratios). Inevitably many electrons and delta rays emitted in

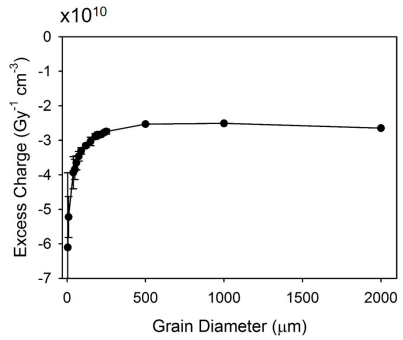


(a)

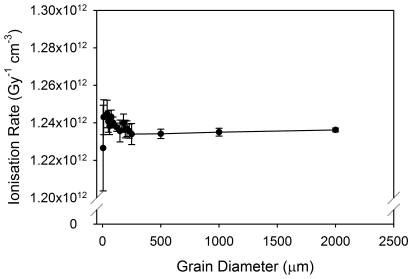


(b)

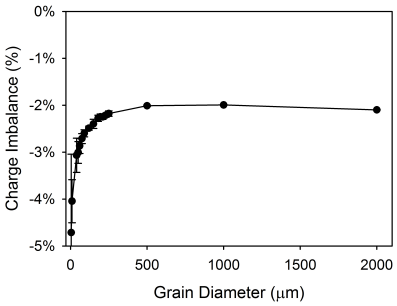


(c)

Figure 5.1: a) Excess charge resulting from irradiation with a mixed infinite matrix spectrum, this increases with increasing grain size. b) Ionisation rate, this increase initially with grain size but stabilises after ∼40 µm. c) Charge imbalance resulting from irradiation with a mixed infinite matrix $\beta^-$ spectrum. The grains approach -2% as the grain size is increased.

the "sediment" do not intersect the target grain, and so these calculations do not contribute to the spectrum of interest; as a result the calculation must be prolonged to provide an acceptably well known spectrum at the grain surface.

For further calculations, the combined spectrum entering the target grain is then emitted in a similar geometry to that shown in SMC5 Figure 5.16b, in which the sediment is replaced by vacuum to prevent further attenuation of the spectrum. This approach allows the target quartz grain to be varied (e.g. in size) without having to run the model in full; good counting statistics can then be obtained within a reasonable timeframe. It is recognised that the true secondary electron spectrum entering a non-radioactive grain will be affected by the grain size. However, this effect

does not seem to be significant, a comparison of the simulated spectrum obtained using a 100 µm and a 2 mm grain is shown in SMC5 Figure 5.17 where it can be seen that the spectra are virtually indistinguishable. The effect at smaller grain sizes should be even less.

Figure 5.1a shows the absolute amount of excess charge density per unit dose as a function of grain size, when the grain is irradiated with the mixed infinite matrix beta spectrum discussed above. At very small grain diameters almost all electrons entering the grain pass through, however, the dose is deposited by the very low energy component of the spectrum and these do not have sufficient energy to escape the grain, resulting in a large negative charge density. Figure 5.1b shows that at the same time the ionisation rate decreases with increasing with grain size. If we express charge imbalance as the net positive or negative charge as a fraction of the total number of electron/hole pairs (Figure 5.1c), the resulting negative charge imbalance decreases from about -4.5% at 5 µm diameter to approaching a constant -2% for larger grains.

### $^{90}$Sr/$^{90}$Y beta source on a Risø TL/OSL reader

We have previously simulated the irradiation of grains in the Risø TL/OSL reader (Chapters 2, 3, and 4) but here we investigate the charge imbalance as a function of grain size. Figure 5.2 shows the results of a beta irradiation using the source module of the Risø TL/OSL reader for irradiation of closely packed spherical quartz grains sitting on a stainless steel disc (as shown in SMC5, Figure 5.18a). Quartzite and feldspar rock slices (9.8 mm diameter, 1 mm thickness) are also modelled, these do not have a backscattering medium as they would be placed on the wheel.

Figure 5.2a shows that when grains are irradiated in the Risø TL/OSL reader they acquire a net negative density of excess electrons which decreases with grain size. This is consistent with the behaviour seen from simulating the natural beta irradiation (Figure 5.1a), however it increases more rapidly than when exposed to the infinite matrix spectrum. However, a quartzite slice (red triangle) appears to have a slightly smaller excess charge density than a corresponding feldspar slice (green triangle) per unit dose. The ionisation rate, Figure 5.2b, increases with increasing grain size as opposed to decreasing, see Figure 5.1b, but there is again a difference between quartzite and feldspar. Feldspar appears to have a smaller ionisation rate which might explain some of the dose rate difference observed in Chapter 3. Finally, the charge imbalance, Figure 5.2c, is similar to that for natural irradiations (Figure 5.1c), although it rises faster to a more or less constant -2% than when exposed to the infinite matrix spectrum.

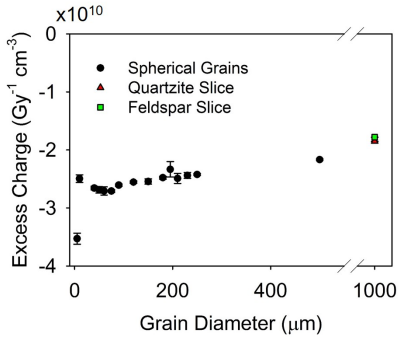


(a)

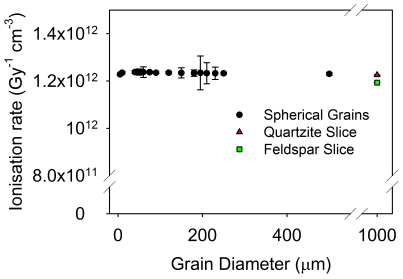


(b)

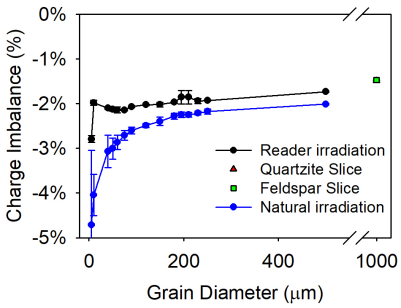


(c)

Figure 5.2: Irradiation of grains on a stainless steel disc using the $^{90}$Sr/$^{90}$Y beta source mounted in a reader beta source module. a) The excess charge density per unit dose decreases with increasing grain size. Quartzite and feldspar slice get a different amount of excess charge b) Ionisation rate during the irradiation. There is once again a difference between quartzite and feldspar c) The charge imbalance is similar to that seen in Figure 5.1c, although smaller grains do not have the same degree of imbalance as when exposed to the infinite matrix spectrum. The charge imbalance during irradiation of quartzite and feldspar rock slices is indistinguishable.

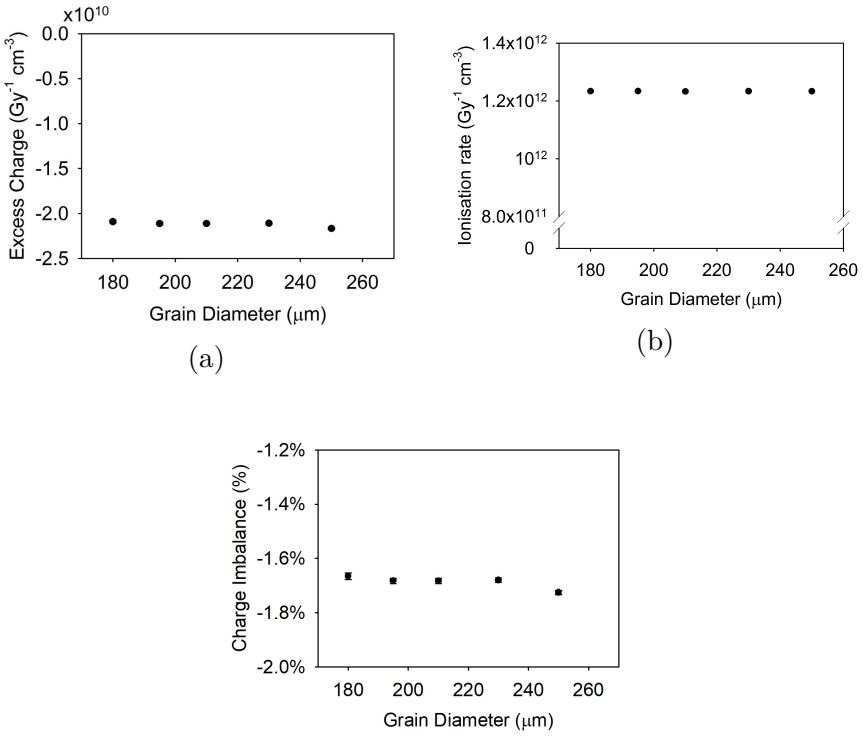


Figure 5.3: Irradiation of quartz grains in a single- grain disc using the reader $^{90}$Sr/$^{90}$Y beta source. a) The excess charge density per unit dose does not change across the grain sizes. This is true for the ionisation rate (b) and charge imbalance (c) in this irradiation geometry.

For the single grain disc geometry, Figure 5.18b in SMC5, both the excess charge density (Figure 5.3a), and ionisation rate (Figure 5.3b), do not change significantly across the grain sizes commonly used for single grain studies (180 - 250 µm). The same is true for the charge imbalance (Figure 5.3c). We conclude that grains in this widely-used size range, when irradiated under typical laboratory conditions either as multi-grain aliquots or single grains, do not show significant variation in charge imbalance.

### Electron beam

Next, we use an electron beam to test modelling predictions, by deliberately implanting a relatively large and predictable charge imbalance. The advantage of using an electron beam (rather than, say, the beta source mounted on the reader) is that it is monoenergetic and can deliver much higher dose

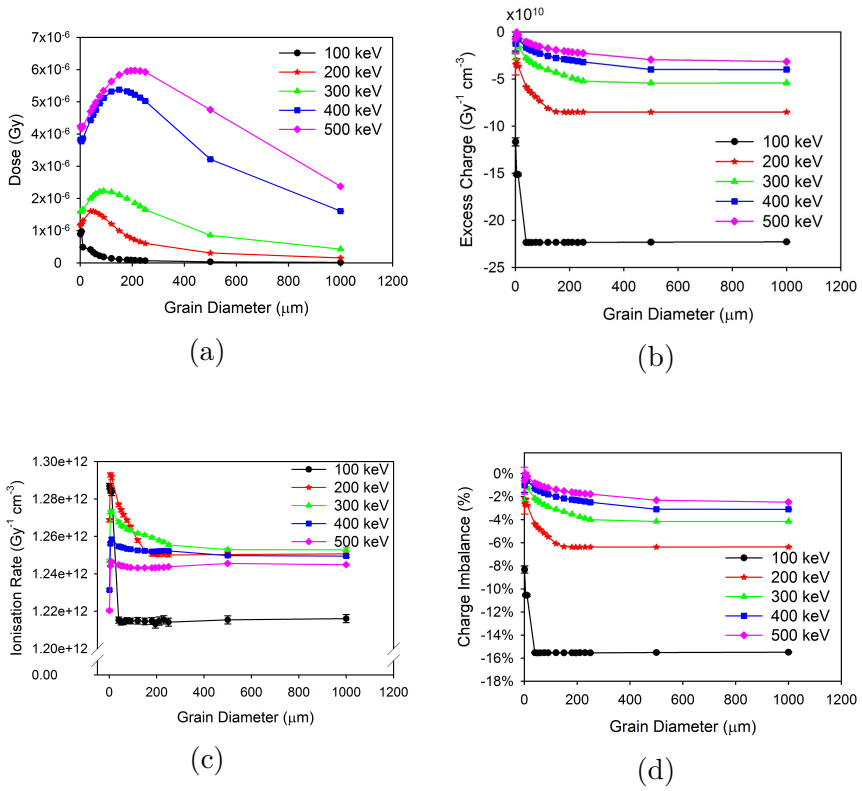


Figure 5.4: Irradiation using the electron beam. a) Dose deposition at different energies for different thicknesses of absorber. This is consistent with the expected behaviour. b) Excess charge density per unit dose. Low energy electrons result in a larger charge excess and this decreases with increasing electron energy. c) The ionisation rate decreases with increasing absorber thickness and there is a clear energy dependence on the ionisation rate as well. d) The degree of charge imbalance is strongly dependent on the incoming electron energy.

rates. The predicted dose deposition as a function of absorber thickness is presented in Figure 5.4a, based on the irradiation geometry described in Figure 5.19 in SMC5.

From Figure 5.4a we can see that for a given energy the deposited dose increases with absorber (detector) thickness before reaching a maximum and then decreasing. The build-up region corresponds to the range of the primary electrons (i.e. the most energetic electrons) and thus the thickness at which all electrons are absorbed and no further energy is deposited. The decrease results from the continued increase in detector volume/mass without an increase in energy deposition. As the energy of the electrons

increase, they can penetrate further and further into the grain and the peak shifts deeper into the absorber.

Figure 5.4b shows that charge imbalance varies with the incoming energy, lower energies result in greater relative negative charge - presumably because lower energy electrons have shorter range and are thus more likely to be stopped in the detector. All the curves eventually become constant when the detector thickness is greater than the range of the incoming electrons. At this stage ($>\sim$200 µm), there is no change in either the number of excess electrons in the detector, or in the number of electron/hole pairs, as the detector increases in thickness. Most surprisingly is the energy dependence of the ionisation rate, which not only changes with absorber thickness but also with the incoming electron energy (Figure 5.4c). However, monoenergetic sources are not found in nature or most laboratory settings, but it is an interesting observation. Finally, as the absorber thickness is increased, so is the charge imbalance ,Figure 5.4d, but again, there is an energy dependence with higher energies resulting in a decreased charge imbalance.

#### $^{137}$Cs point source irradiation

So far, we have shown that external irradiation with electrons leads to a net excess negative charge in the irradiated grains. Gamma sources, however, are often designed to have build-up material in front of the sample in order to avoid charge gradients across the irradiated volume.

In luminescence dosimetry, beta sources are often calibrated by comparing the luminescence signal induced by a beta source irradiation with that induced by a known gamma dose. Grains irradiated by a gamma source (with appropriate build up material) can be expected to be much closer to charge balance than grains irradiated with electrons. Here we model the $^{137}$Cs point source used to irradiate calibration quartz (Hansen et al., 2015) in a scatter free geometry. This geometry is shown in Figure 5.20 in SMC5.

Figure 5 shows the charge imbalance as a function of depth in 100 µm thick quartz sheets (10 x 10 cm sides); these simulate both the glass holder and the sample. In Hansen et al. (2015) the 1.1 mm thick sample space extends from 1.85 to 2.95 mm and in this range we observe no significant charge imbalance. This means that when beta sources are calibrated against a gamma source, we are comparing a dose given under conditions of net excess electrons with a dose given under charge neutral conditions.

### 5.2.2 Luminescence modelling

Having established that modelling predicts charge imbalance at some level in quartz exposed to ionising radiation in nature and in the laboratory, the

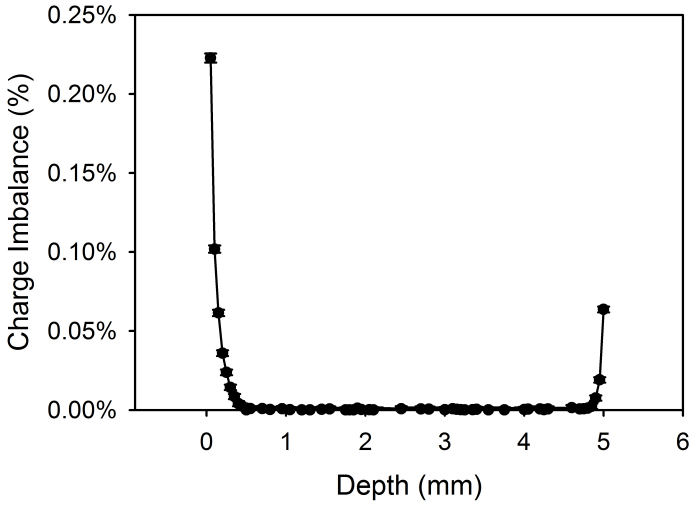


Figure 5.5: Charge imbalance as a function of depth in a stack of 100 µm quartz sheets irradiated by a $^{137}$Cs point source. There is no significant charge imbalance between 0.5 mm and 4.5 mm.

next step is to investigate how this might affect luminescence production, if at all. We have previously published data which suggested that an excess electron population during irradiation resulted in a reduction in optically stimulated luminescence (OSL) output at saturation and in response to a small test dose (Chapter 4); we hypothesised that this was due to a reduction in the hole population, but did not present any quantitative support for this hypothesis. Here the luminescence production model of Bailey (2004), as refined by Pagonis (2007, 2008) is used to model the trap population and luminescence behaviour with and without charge imbalance. For this purpose, we have introduced slight modifications to the equations:

$$\frac{dn_i}{dt} = n_c \left(N_i - n_i\right) A_i - n_i P_i \sigma_i e^{-\frac{E_i^{th}}{k_B T}} - n_i s_i e^{-\frac{E_i}{k_B T}} \tag{5.1}$$

$$\frac{m_j}{dt} = n_v \left(M_j - m_j\right) A_j - m_j s_j e^{-\frac{E_j}{k_B T}} - n_c n_j B_j \tag{5.2}$$

$$\frac{n_c}{dt} = c_e \cdot X \cdot \dot{D} - \sum_{i=1}^{i} \frac{dn_i}{dt} - \sum_{j=1}^{j} n_c n_j B_j \tag{5.3}$$

$$\frac{n_v}{dt} = c_h \cdot X \cdot \dot{D} - \sum_{j=1}^{j} \frac{dm_j}{dt} - \sum_{j=1}^{j} n_c n_j B_j \tag{5.4}$$

where $n_i$ is the concentration of trapped electrons in trap $i$ (cm$^{-3}$), $N_i$ is

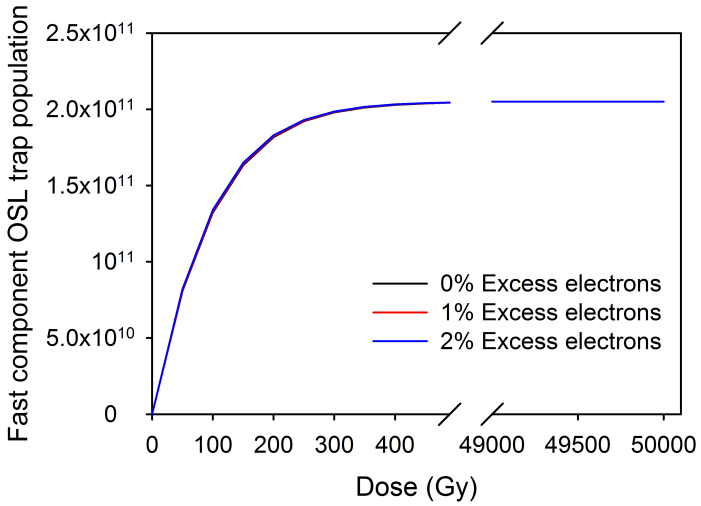


Figure 5.6: The variation of OSL trap population with dose derived using equations (1) to (4), with parameter values taken from Bailey (2004) and $c_h = 1$, $c_e$ =1 , 1.01, and 1.02 (0, 1 and 2% excess electrons, respectively).

the total concentration of available electron traps $i$ ($\mathrm{cm}^{-3}$), $m_j$ is the concentration of trapped holes in trap $j$ ($\mathrm{cm}^{-3}$), $N_J$ is the total concentration of available hole traps $j$ ($\mathrm{cm}^{-3}$), $n_c$ and $n_v$ are the conduction and valence band concentrations ($\mathrm{cm}^{-3}$) respectively, $A_{i,j}$ is the transition probability of trapping from a de-localised band to trap $i$ or $j$ ($\mathrm{cm}^{-3}\,\mathrm{s}^{-1}$), $B_j$ is the transition probability for recombination from the conduction band to hole trap $j$ ($\mathrm{cm}^{-3}\,\mathrm{s}^{-1}$), $k_B$ is Boltzmann's constant ($\sim 8.615 \cdot 10^{-5}\mathrm{eV\,K}^{-1}$), $T$ is the absolute temperature, $P$ is the photon flux ($\mathrm{s}^{-1}\,\mathrm{cm}^{-2}$), $\sigma_i$ is the photoionisation cross-section for electron trap $i$ ($\mathrm{cm}^2$, $E_{i,j}$ is the trap depth in eV of trap $i$ or $j$ from nearest band edge, $s_i$ is the "frequency factor" ($\mathrm{s}^{-1}$), $\dot{D}$ is the dose rate $\mathrm{Gy\,s}^{-1}$, $X$ is the ionisation rate (electron/hole pairs generated, $\mathrm{cm}^{-3}\,\mathrm{Gy}^{-1}$), $c_e$ is the degree of excess electrons, and $c_h$ is the degree of excess holes.

Equations (5.1) and (5.2) remain unmodified, but in Equations (5.3) and (5.4) we introduce the dimensionless constants $c_e$ and $c_h$, to allow the number of electrons produced per unit volume per unit dose ($c_e \cdot X$) to vary independent of the number of holes produced per unit volume per unit dose ($c_h \cdot X$). If an irradiation is charge neutral, these factors are unity and Equations (5.3) and (5.4) are identical to those of Bailey (2004) and Pagonis (2007, 2008). The two constants, $c_e$ and $c_h$, can be varied independently to allow for asymmetric filling of the conduction and valence bands.

Using the equations listed above, we start from a completely empty

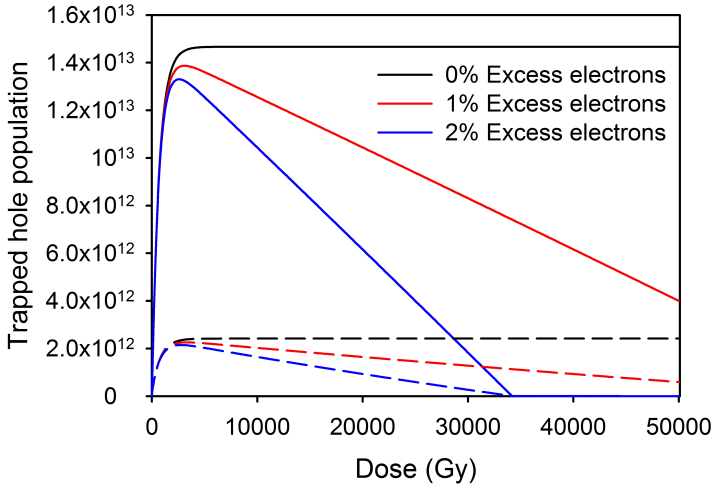


Figure 5.7: Variation in trapped hole populations with dose during the irradiations of Figure 5.6. The solid curves show the luminescence centre population and the dashed curves shows the sum of non-luminescence centres.

crystal, i.e. no trapped charge, and then expose it to a dose of 50 kGy at a dose rate of $1\,\mathrm{Gy\,ka^{-1}}$ as specified by Bailey (2004). Figure 5.6 illustrates the resulting electron population trapped in the 'fast-component' dosimetric OSL trap (trap 3 of Bailey, 2004) during both charge neutral irradiations, and those without charge balance.

The introduction of charge imbalance slightly affects the initial filling rate of the electron traps, as there are more electrons available for trapping, but not surprisingly there is no decrease in the trapped electron population at any point during irradiation.

This conclusion does not apply to the hole centre populations. In Figure 5.7 we can see that during charge neutral irradiation, the hole traps continue to fill to much higher doses (as the electron traps other than the OSL trap continue to fill) before they eventually stop filling. This occurs when all the various electron traps are completely filled. Once the electron traps have filled it is no longer possible to trap further holes. This makes intuitive sense; any new electron-hole pair generated once the electron traps are full must recombine, because any electrons introduced by further irradiations must recombine to maintain charge balance. However, the introduction of charge imbalance means that the hole population does not reach the same level as the electron population; these excess electrons are not generated in the crystal and so lack a hole which can be trapped.

Any such excess electrons are then able to recombine with trapped holes, reducing the trapped hole population. This reduction may be irreversible as long as there is an excess of electrons during irradiation.

## 5.3 Experimentals

Here we describe experiments intended to test the model predictions described above. Sensitised quartz grains were irradiated using 200 or 100 keV electron beams, and OSL response investigated.

### 5.3.1 Sample preparation

Quartz extracts from a Chinese loess (sample H28112) from Stevens et al. (2016) was used for the experiments. The extract was sieved to 40-63 µm before treatment with hydrochloric acid (HCl, 10%) and hydrogen peroxide (H2O2, conc.) to remove any carbonates and organic matter, and etching with 40% HF to remove any feldspars. Finally, the sample was sieved again to >40 µm to ensure a controlled grain size fraction. The sample was then heated to 700 °C for 1 hour before receiving a 2 kGy (5 kGy) gamma dose using a $^{60}$Co source for the 200 keV (100 keV) experiment. Following the gamma dose, the sample was heated to 450 °C for 1 hour, see Hansen et al. (2015). The 100 keV and 200 keV experiments used the same sample material but different batches, as the one used of the 200 keV experiment was not sufficient to make enough aliquots for a second round of experiments. TL and OSL measurements were carried out on a Risø TL/OSL reader. The protocol used for the measurements is shown in Table 5.1. All quartz TL/OSL measurements were carried on the same reader with the same wheel to minimise variability arising from variations in instrumental sensitivity.

For the 200 keV electron beam irradiation, a total of 228 aliquots were used, in 19 groups of 12 aliquots each. Each group received a different electron beam dose. For the 100 eV electron beam irradiation, this was increased to a total of 300 aliquots, in 24 groups of 12 aliquots each, with a repeated point at 300 kGy using 12 aliquots. In order to determine whether the observed change in luminescence output and sensitivity seen in our previous work (Chapter 4) could be attributed to opacity changes as a result of irradiation, six 1 mm thick quartzite slices were also given a dose of 50, 200, 700, 1500, 3500 and 5000 kGy using the 200 keV beam. These had their absorption spectra from 200 nm to 900 nm measured before and after irradiation with 200 keV electrons using a Shimadzu UV-2700 UV-VIS spectrophotometer. We did not see any difference in the absorption spectra

Table 5.1: Protocol for measurement of OSL before and after both 100 and 200 keV electron beam irradiations. Note: $L_{x-i}$ and $T_{x-i}$ indicate test dose response before and after electron beam irradiation respectively.

(a) Luminescence measurement sequence prior to e-beam irradiation

| Step | Treatment | Observation |
|---|---|---|
| 1 | Test Dose, 6 Gy | |
| 2 | TL to 160 °C | |
| 3 | OSL at 125 °C, 100 s | $L_{x-1}$ and $L_{x-3}$ |
| 4 | Test dose, 6 Gy | |
| 5 | TL to 160 °C | |
| 6 | OSL at 125 °C, 100 s | $L_{x-2}$ and $L_{x-4}$ |
| 7 | Repeat 1-6 once more | |
| 8 | 0 Gy | |
| 9 | TL to 160 °C | |
| 10 | OSL at 125 °C, 100 s | $L_{x-5}$ |

(b) Luminescence measurement sequence after e-beam irradiation

| Step | Treatment | Observation |
|---|---|---|
| 1 | TL to 160 °C | |
| 2 | OSL at 125 °C, 100 s | L |
| 3 | TL to 160 °C | |
| 4 | OSL at 125 °C, 100 s | $L_{TT}$ |
| 5 | Test Dose, 6 Gy | |
| 6 | TL to 160 °C | |
| 7 | OSL at 125 °C, 100 s | $T_{x-1}$ and $T_{x-3}$ |
| 8 | Test dose, 6 Gy | |
| 9 | TL to 160 °C | |
| 10 | OSL at 125 °C, 100 s | $T_{x-2}$ and $T_{x-4}$ |
| 11 | Repeat 5-10 once more | |

in the dose range up to 5 MGy; these data are shown in SMC5 Figures 5.21 and 5.22.

## 5.4 Results

The experimental results are presented in the following sections. An average of the four $L_{x-i}$ ($\bar{L_x}$)was calculated for each of the aliquots, the same calculations were run for the four $T_{x-i}$ after electron beam irradiation to give ($\bar{T_x}$). Since we have hundreds of aliquots, it is possible that there will be inter-aliquot variation in luminescence response due to intrinsic factors (recombination probabilities, trap concentrations, trapping probabilities) as well as extrinsic factors (aliquot mass/size, grain size). Here all $L_x$ responses (see Table 5.1a) prior to any electron beam irradiation have been normalised to that of the first aliquot. Then any remaining aliquot to aliquot variability arises from differential response to the treatment sequence, rather than any absolute variation. The signals were all normalised using the fast component OSL signal, as calculated using the signal observed during the initial 0.4 s of the signal less that in the following 0.4 s. The summed signal is taken as the sum of the entire OSL decay curve minus a background averaged over the last 20 channels. L in Table 5.1b gives the luminescence response to the electron beam irradiations, and the relative sensitivities are calculated as

$$Sensitivity = \frac{\bar{T_x}}{\bar{L_x}} \tag{5.5}$$

For this calculation, normalisation is, of course, not required. For all doses, the data is an average of the responses of 12 aliquots.

### 5.4.1 200 keV

The 200 keV irradiations were carried out over a single day with 10 minute breaks between each irradiation to allow the generator to cool, and to allow any free charge recombine, i.e. to allow the conduction and valence bands to equilibrate.

The fast component signal, derived from observation L in Table 5.1b and shown in Figure 5.8a, decreases monotonically with given dose. This is not surprising; the smallest dose increment is 50 kGy, and the fast component is known to saturate at much less than 1 kGy (Wintle and Murray, 2006 and references therein). The sensitivity of the fast component decreases in a similar manner (Figure 5.8b). A decrease in luminescence and sensitivity was expected as the hole population started to decrease (Figure 5.7),

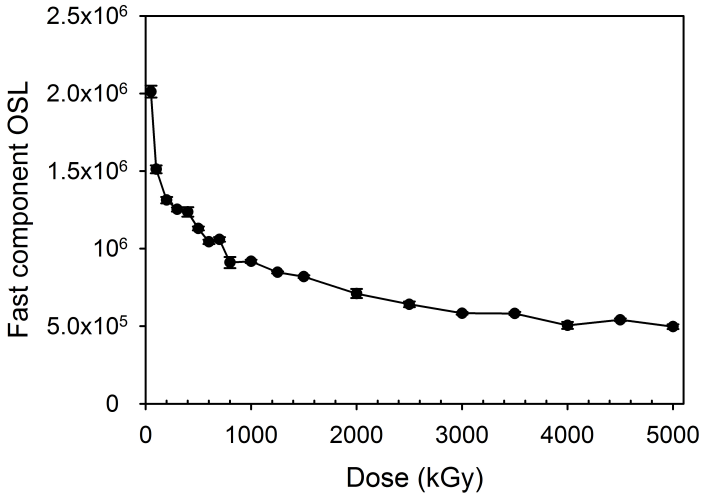


(a)

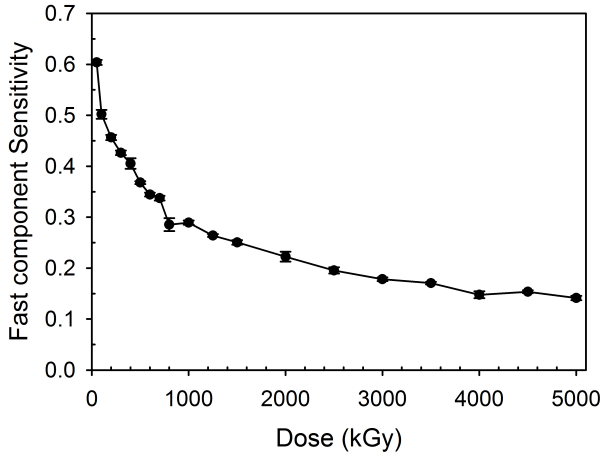


(b)

Figure 5.8: a) Fast component OSL following electron beam irradiation with 200 keV electrons (L in Table 5.1b) and b) Fast component sensitivity after irradiation with 200 keV electrons (Equation (5.5))

although the non-linear form of the decrease is unexpected; modelling predicts a linear decrease in hole population after saturation of electron traps. In contrast, at high doses (>4 MGy) both the fast component OSL and sensitivity stabilise, suggesting no further reduction in the luminescence efficiency.

The luminescence response seen in Figure 5.9a is consistent with that seen for the same sample by Autzen et al. (2018) (Chapter 4); the greater resolution of doses employed in this work, however, makes the response at higher doses clearer. Instead of a linear decrease, the response becomes almost constant >4 MGy. At low electron beam doses (<500 kGy), the sensitivity of the OSL sum, Figure 5.9b, increases from an initial ∼5 times to ∼8 times its sensitivity before irradiation. Unlike the sum OSL signal following electron beam irradiation, the sensitivity of the summed OSL signal may not have completely stopped decreasing following the maximum 5 MGy dose reached in this experiment.

Figure 5.10 shows the electron beam response divided by the sensitivity, in other words; it is the response at saturation divided by the response at the beginning of the growth curve. Here we have normalised to the first dose point (50 kGy). The ratio decreases by between 15% (fast component) and 25% (summed signal) at between 150 and 200 kGy, before increasing again and returning to the original ratio at 5 MGy. This indicates that there is no significant change in shape of the growth curve during the experiment, which suggests that there is also no defect creation as a result of irradiation. This set of experiments has served as an expansion of our previous work (Chapter 4) as we use the same sample and electron beam energy. Importantly, the higher dose resolution allows us to be confident that the total OSL output does not decrease linearly, as expected from modelling, but appears to asymptote to some finite value with dose. One explanation for this is electrostatic repulsion of the incoming beam by the build up of excess negative charge in the grain. This would tend to prevent further deposition of energy (or charge), because incoming electrons would enter the grain with less energy, if indeed they were able to enter the grain at all. In this case the dose axis is no longer an indication of absorbed dose but rather expected dose for a neutral target. From the modelling predictions shown in section 5.2, we would expect a lower incident electron energy to significantly increase the charge imbalance for a given dose. As a result, the asymptote in OSL response to a finite value at high doses would be observed at a lower dose (and a higher OSL signal); the lower energy incident electrons would require less net charge to repel them and so the decrease in OSL would not be as marked as that of the 200 keV experiment. It would require ∼3.4 MGy to achieve complete reflection of a 200 keV electron when

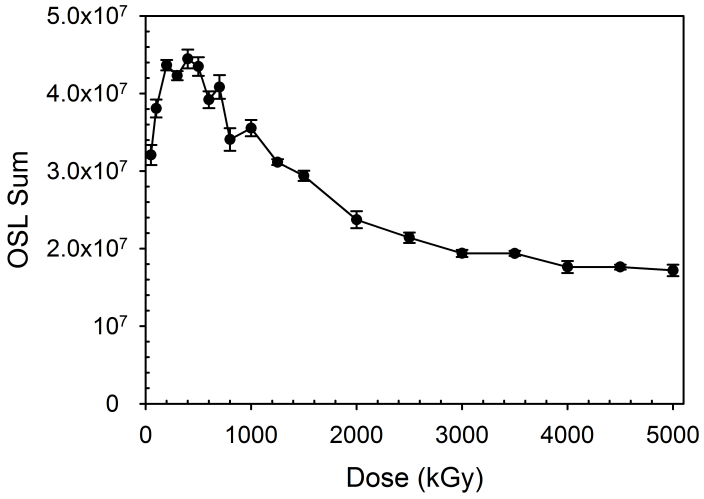


(a)

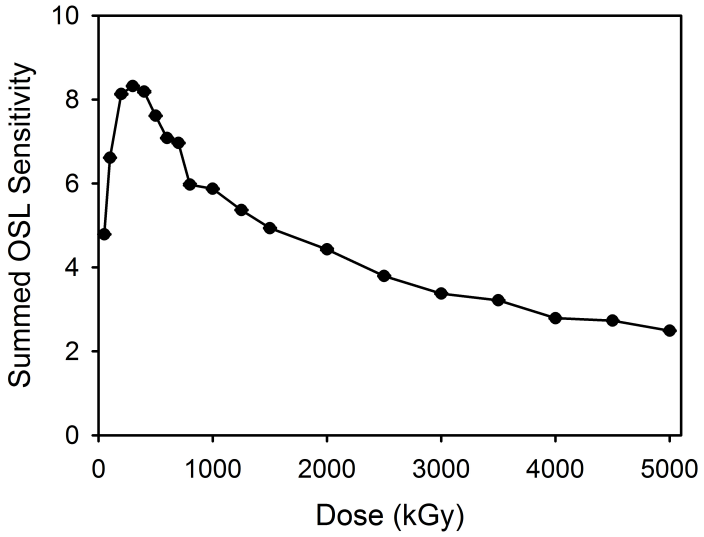


(b)

Figure 5.9: a) Summed OSL response (L in Table 5.1b) as a function of irradiation with 200 keV electrons and b) Sensitivity for the summed OSL signal (Equation (5.5)) following electron beam irradiation with 200 keV electrons.

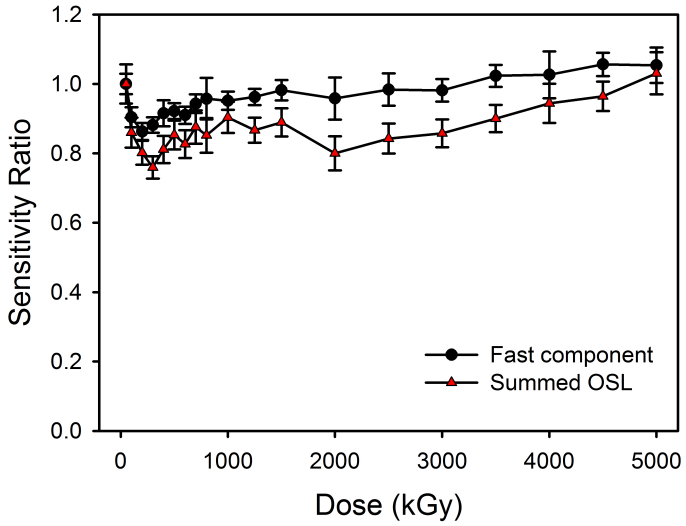


Figure 5.10: Electron beam signal (L, step 2 in Table 5.1b) divided by corresponding sensitivity for irradiation with 200 keV electrons ($L/(\bar{T}/\bar{L})$

irradiating a 50 µm quartz sphere, if we assume that until this dose the incoming electrons are not repelled or slowed down. Since the charge buildup will continuously slow down incoming electrons this dose estimate is merely a minimum dose required to achieve complete reflection, in fact we observe experimentally that this happens at ∼4 MGy. For a 100 keV electron we would expect complete reflection to happen at ∼475 kGy.

### 5.4.2 100 keV

To test the above prediction, that the response to a lower energy electron beam would stop decreasing at a lower dose than observed with the 200 keV beam, we repeated the electron irradiation experiment using a 100 keV beam. The 100 keV irradiations were carried out using the same protocol as the 200 keV irradiations, but with three differences. 1) The lowest dose is now 5 kGy (instead of 50 kGy) to investigate the behaviour at lower doses. 2) In order to have better resolution around the peak, the dose point at 4.5 MGy has been replaced with one at 900 kGy. 3) Finally, the dose point at 300 kGy was duplicated, but administered over 72 hours in 6 irradiations instead of over 2 hours in 9 irradiations. This was done to test whether the relaxation time of 10 minutes was indeed sufficient for charge recombination to occur, and the conduction band to empty even if all traps were full.

The fast component OSL, shown in Figure 5.11a, increases for doses

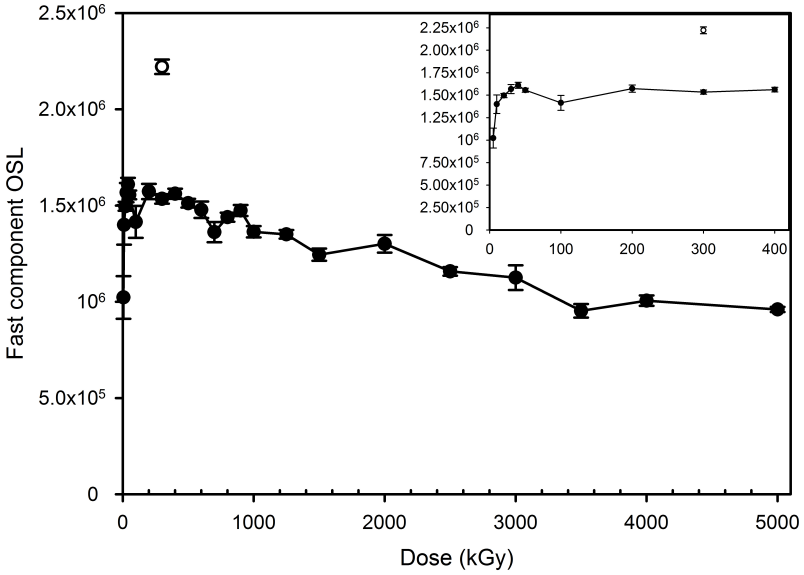


(a)

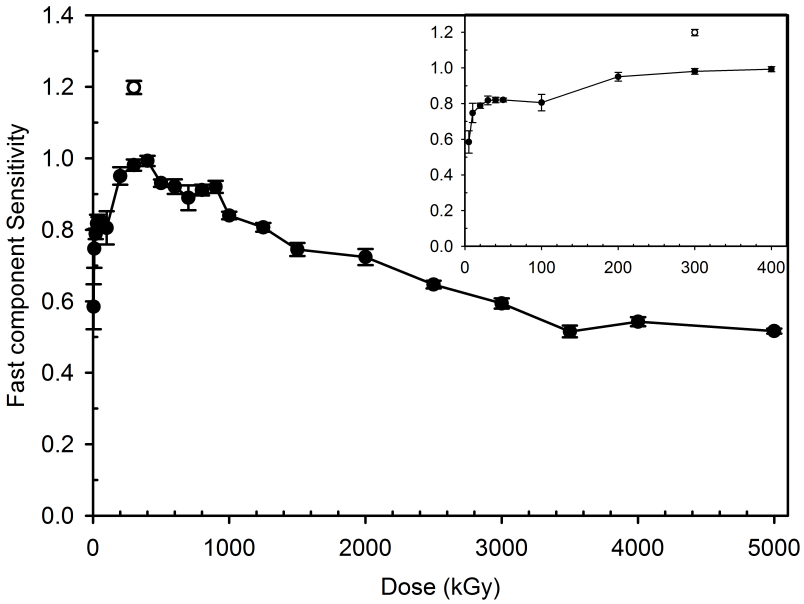


(b)

Figure 5.11: a) Fast component OSL response (L in Table 5.1b) following electron beam irradiation with 100 keV electrons. Inset shows the response from 0 to 400 kGy. The unfilled circle is the repeated point. b) Fast component sensitivity after irradiation with 100 keV electrons (Equation (5.5)). Inset shows the response from 0 to 400 kGy. The unfilled circle is the repeated point.

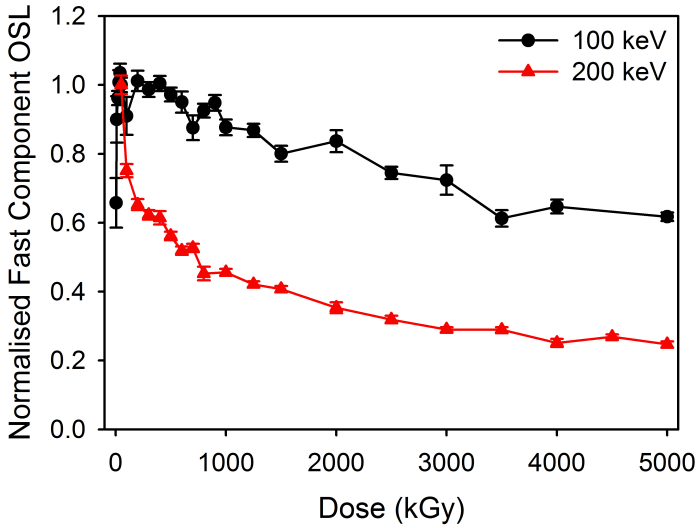


Figure 5.12: Fast component OSL response for 100 and 200 keV irradiations normalised to the 50 kGy dose points

below 40 kGy and then plateaus at ∼400 kGy (see the inset) after which it slowly decreases. The sensitivity (Figure 5.11b) shows the same behaviour but with a much clearer decrease. This is to be contrasted with Figures 5.8a and 5.8b where the fast component for 200 keV showed a very rapid decrease from 50 kGy and only became constant above 4 MGy. Giving a 300 kGy dose over 72 hours results in a higher luminescence response as well as a higher sensitivity for the fast component, although the effect on sensitivity may be smaller.

Figure 5.12 summarises the fast component data from both the 100 and 200 keV experiments, normalized to the 50 kGy point; these data clearly show the smaller decrease in luminescence output for 100 keV irradiations. For 200 keV, the fast component response drops by almost 80% from 50 kGy to 5 MGy, while for the same dose range the luminescence output of the 100 keV aliquots drops by only around 30%. This observation is consistent with the presence of an electric field due to charge excess, but it also suggests that the two dose axes are not comparable in terms of absorbed dose, but only apparent dose calculated from exposure time.

The summed OSL signal (Figure 5.13a) and summed sensitivity (Figure 5.13b) following 100 keV irradiations behave similarly to those following 200 keV electron irradiations (Figures 5.9a and 5.9b). Similar to the fast component behaviour, the summed OSL signal asymptotes to a constant at lower doses following the 100 keV electrons irradiation than following

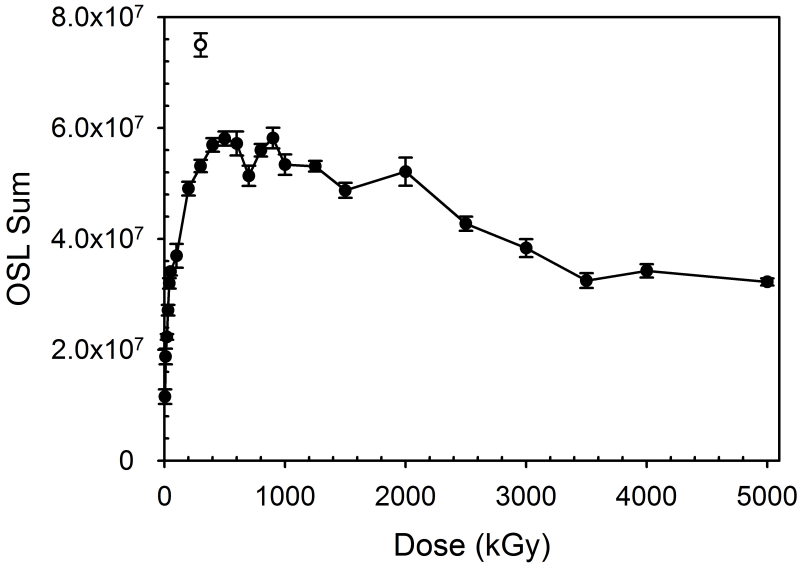


(a)

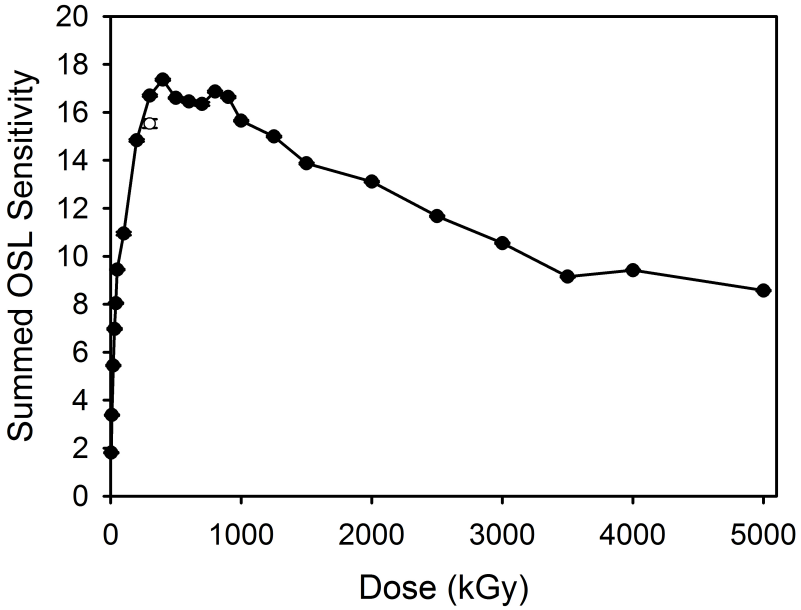


(b)

Figure 5.13: a) Summed OSL response as a function of dose following irradiation with a 100 keV electron beam. Unfilled circle is the repeated point. b) Summed OSL signal sensitivity (Equation (5.5)) following 100 keV electron beam irradiation. Unfilled circle is the repeated point.

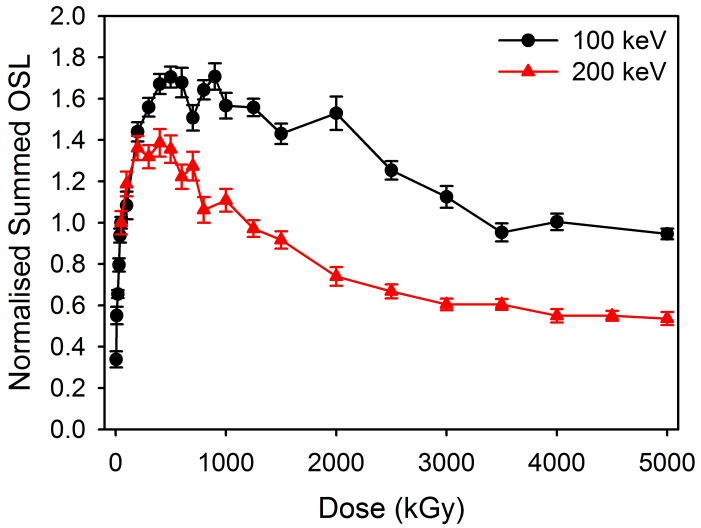


Figure 5.14: Summed OSL response for 100 and 200 keV irradiations normalised to the 50 kGy dose points

the 200 keV irradiations, and the signal does not decrease as much with dose. The differences in behaviour of the summed signal following 100 and 200 keV irradiations can be seen more readily in Figure 5.14, where the summed OSL signal for both electron energies have been normalised to the light output at 50 kGy.

The 200 keV irradiations decrease around 40% from 50 kGy to 5 MGy (57% compared to the peak intensity at 400 kGy), while the luminescence response to 100 keV electrons at 5 MGy equals that at 50 kGy (or decreases by 37% compared to the peak intensity at 400 kGy). The behaviour of both the fast component and summed OSL signals from 100 keV electrons are consistent with a decrease in dose deposition due to a greater charge excess and easier repulsion of the incoming electron beam at lower energies. The luminescence response continues to decrease, however, until 3.5 MGy, much larger than we predicted from modelling. This could be the result of the electrons being continuously slowed down as the charge on the grain increases and this causes the shift to larger doses. For the summed OSL signal we see, once again, that the luminescence response to 300 kGy is larger when the dose was administered over 72 hours. However, the sensitivity is the same as for the short irradiation time (Figure 5.13b). This leads us to believe that the difference is due to charge deposition rather than charge recombination. The luminescence response could be affected by excess charge that is stable on the timescale of a few hours whereas the

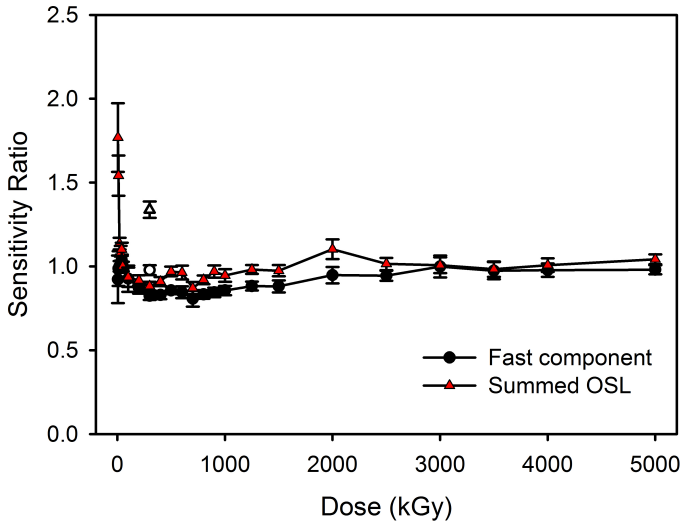


Figure 5.15: Electron beam response divided by corresponding sensitivity, normalised to 50 kGy for the 100 keV irradiations.

sensitivity would only be affected by excess charge remaining after optical stimulation and stable on a timescale of days. This difference in sensitivity behaviour compared to initial luminescence response was less pronounced in the 200 keV experiment (Figure 5.14), perhaps because the charge was deposited more uniformly in the target grains.

The ratio of the luminescence response to the electron beam irradiations, to the following sensitivity is shown in Figure 5.15; this is very similar to the data for 200 keV (Figure 5.10), where this ratio also remains close to unity from 50 kGy upwards, indicating no major change in the growth curve shape as a result of high dose irradiation. However, there is some significant deviation from unity at doses lower than 50 kGy, especially for the fast component signal.

## 5.5 Discussion

Charge transport modelling using GEANT4 has shown that charge imbalance occurs in many of the irradiation geometries relevant to trapped electron dosimetry, and in particular, to luminescence dating. This modelling strongly suggests that such charge imbalance is not only dependent on the energy of the incoming electron spectrum but also on the grain size of the absorbing medium. For the first time, the results of charge transport

modelling have been used as the input to luminescence production models to allow the prediction of the effects of changes in energy and irradiation geometry on charge imbalance, and so on trapped charge populations and the resulting luminescence output. The results of this modelling, summarised in Figures 5.6 and 5.7, show that the introduction of excess electrons during irradiation would lead to a decrease in the trapped hole populations once all the electron traps have been filled. This prediction is supported by our new experimental data and by data presented in Autzen et al. (2018) (Chapter 4). However, the greater dose resolution used in the new experiments allows us to distinguish behaviour undetected in the previous study, namely that the OSL signals resulting from large electron beam doses do not decrease linearly at high dose but rather seem to asymptote to a steady-state at an apparent dose of around 4 MGy (for the 200 keV electron beam); above this dose range no further depression of the OSL signal or subsequent sensitivity is observed. The results from 100 keV electron irradiations shows a smaller depression of both OSL response to electron beam dose and sensitivity. We propose that this is due to build up of sufficient excess charge, such that, before entering the target grain the incoming electrons lose energy to the surrounding electric field induced by the excess charge and may even be completely stopped. Because they no longer enter the grain, or only enter it with a reduced initial energy, the absorbed dose rate is significantly lower than that predicted, resulting in unexpectedly smaller cumulative absorbed doses. Related observations have been reported by Reimer (1985) and Vigouroux et al. (1986) both of whom observed that the external potential surrounding a target and arising from a build up of excess charge during irradiation could increase until it eventually equalled the accelerating voltage of the beam and so result in the full reflection of the incoming electrons.

According to our modelling, and assuming any excess charge is stable with time, then a similar situation can develop during natural irradiations. Although the natural secondary electron spectra include energies very much higher than 200 keV, approximately 23% of the total energy carried by the infinite matrix secondary electron spectrum derived from beta emission is carried by electrons with energies <200 keV. Thus, although complete reflection may not be likely in nature, it is very possible that grains could build up enough charge to repel the low energy part of the incoming spectra. This would alter the effective dose rate for grains which have a very long irradiation history, and thus a large accumulated dose.

## 5.6 Conclusion

We have presented modelling results which show that charge imbalance occurs across all common irradiation geometries used in luminescence dating and that this is both spectrum and grain size dependent. The predictions of these charge transport models have been used as input to luminescence production equations and the results support our initial hypothesis that excess electrons can lead to a decreased hole population. We have used electron beam irradiations to give a high dose resolution resulting from two incident energies. From the observation of the resulting OSL signals, and of OSL sensitivity measurements made before and after electron irradiations, it is clear that the OSL does not decrease linearly at large doses, as modelling predicts. This is most likely to be due to repulsion of the incoming electrons by the electric fields surrounding the target grains resulting from the accumulated excess charge. This argument is supported by the different behaviours of 100 and 200 keV electron irradiations and cannot be explained by charge-neutral luminescence modelling, or by opacity changes resulting from irradiation. We have not yet investigated the effects of these charge imbalances on luminescence production at low doses (below electron trap saturation). Nevertheless one can realistically speculate that electric fields resulting from internal excess charge are likely to vary considerably from grain to grain, because of both grain history and the immediate surroundings of the grain. This would in turn give rise to variations in effective dose rate both in the laboratory and in nature. Such a mechanism has the potential to give rise to previously unforeseen micro-dosimetric variability at the single grain level.

## 5.7 Supplementary Material for Chapter 5

## 5.8 Irradiation Geometries

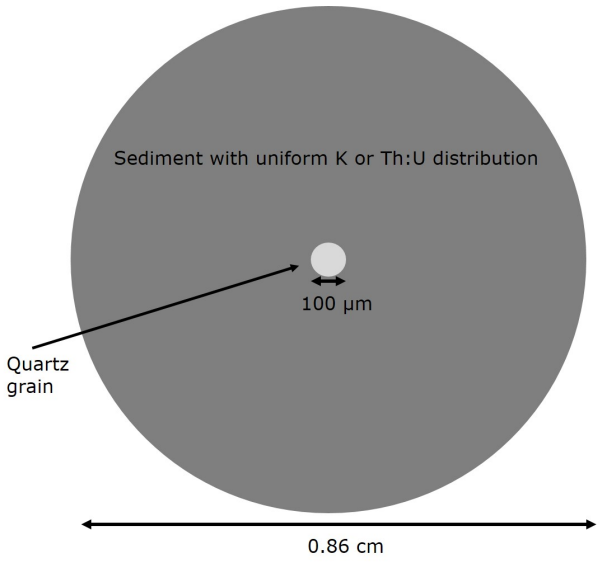


(a)

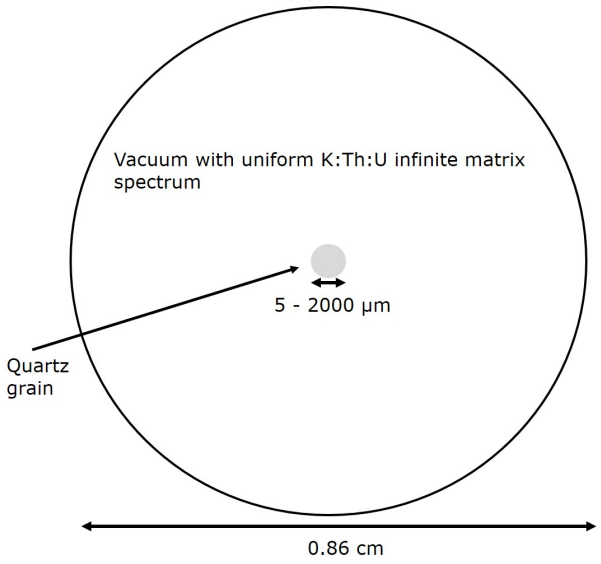


(b)

Figure 5.16: The irradiation geometry used for obtaining the infinite matrix spectra entering a 100 µm spherical quartz grain at the centre. b) The irradiation geometry used for modelling the dose and charge imbalance for various grain sizes. The emitted spectrum is shown in Figure 5.17. This geometry is identical to the one shown in a) with the exception of the vacuum replacing the sediment.

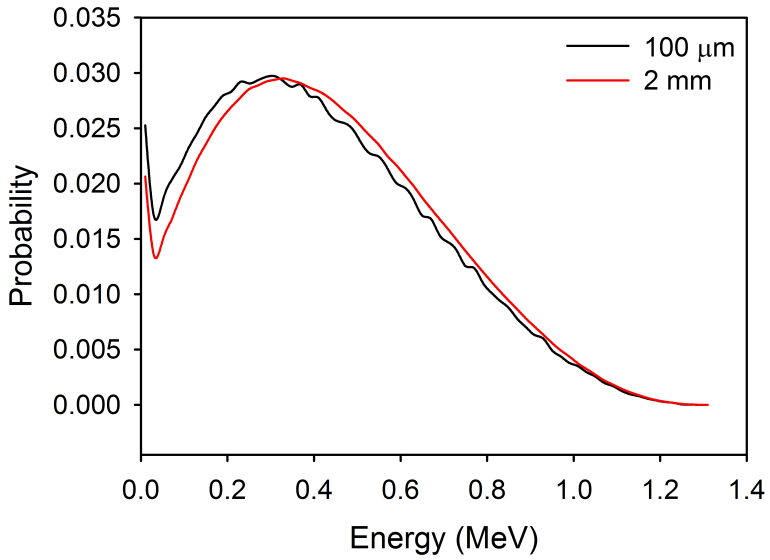


Figure 5.17: Infinite matrix spectra obtained for a 100 µm and 2 mm diameter spherical grain. There is only a small difference in the effect of altering the grain size.

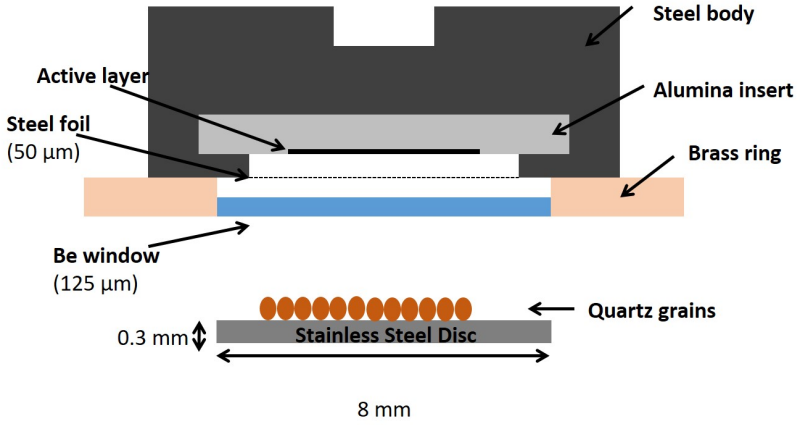


(a)

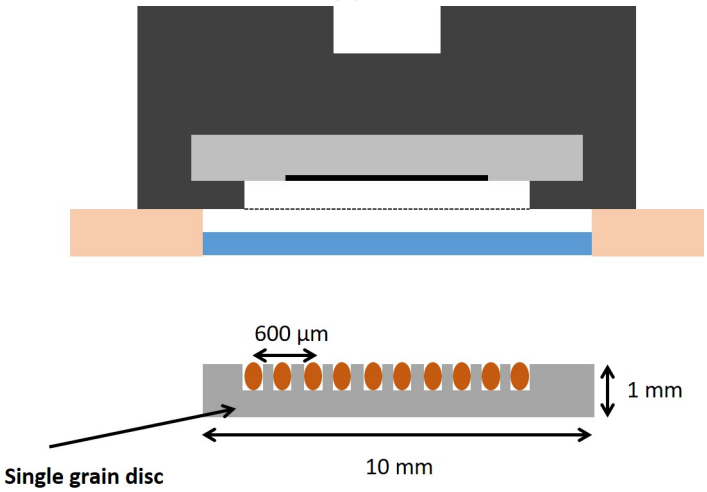


(b)

Figure 5.18: The irradiation geometries used for modelling spherical grains irradiated by the $^{90}Sr/^{90}Y$ source in the Risø TL/OSL reader. a) Close-packed spherical grains irradiated on a stainless steel disc and b) irradiation of spherical grains in a single-grain disc.

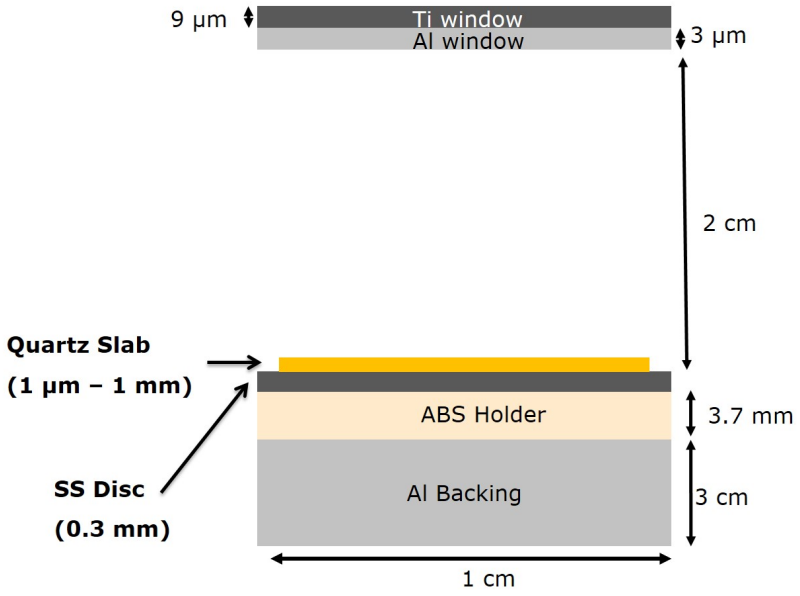


Figure 5.19: Geometry used for simulating the electron beam at various energies. The thickness of the quartz slab is varied between 5 µm and 2 mm.

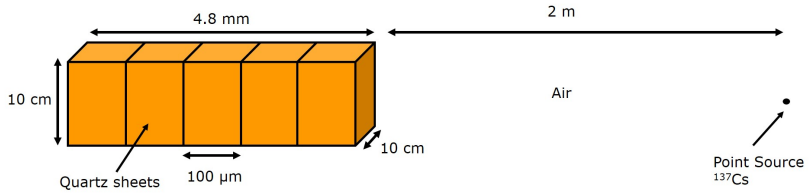


Figure 5.20: Geometry used for simulating the $^{137}$Cs gamma irradiation facility used in the manufacture of Risø calibration quartz. The glass holder has been replaced by full 10x10 cm$^2$, 100 µm thick quartz sheets. The $^{137}$Cs is approximated as a point source located 2 m from the front of the sample with air filling out the gap.

## 5.9 Absorption spectra for quartzite

Absorption spectra were measured for six quartzite slices before and after irradiation with 200 keV electrons using a Shimadzu UV-2700 UV-VIS spectrophotometer. These slices had previously been sensitised by annealing to 700 °C for 1 hour. Each quartzite slice was mounted with thin strips of tape on a holder with a 1 mm wide slit running down the centre of the slice. The orientation of each slice was noted. After irradiation, the OSL response of

each slice was measured using a 160 °C pre-heat and stimulation with blue LEDs at 125 °C similar to that used for the aliquots. After these measurements, the slices were mounted on the holder with the same orientation as the measurements prior to electron beam irradiation. All measurements were performed under daylight conditions.

Figure 5.21 does not show a marked change in spectrum, however, we are interested in changes around the stimulation wavelength of the blue LEDs (∼470 nm) and the emission wavelength (∼370 nm) as these may affect the OSL intensity which we observe. The relative difference as a result of irradiation was calculated using

$$Rel.Diff = \frac{A_{post}(\lambda) - A_{prior}(\lambda)}{A_{prior}(\lambda)} \tag{5.6}$$

where $A_{post}(\lambda)$ is the absorption after irradiation at a wavelength $\lambda$ and $A_{prior}(\lambda)$ is the absorption prior to irradiation at the same wavelength.

Plotting these for the wavelength range 300-570 nm, Figure 5.22, we see that the largest difference occurs at 700 kGy where there is a 6% increase in the absorption in the blue LED window as well as a 5% absorption increase in the filter window. However, for the largest dose, 5 MGy where we see the largest impact on luminescence due to electron beam irradiation, we observe virtually no change in the absorption. Given this, we conclude that the changes we observe in luminescence behaviour is not due to opacity changes of the material but rather a difference in recombination.

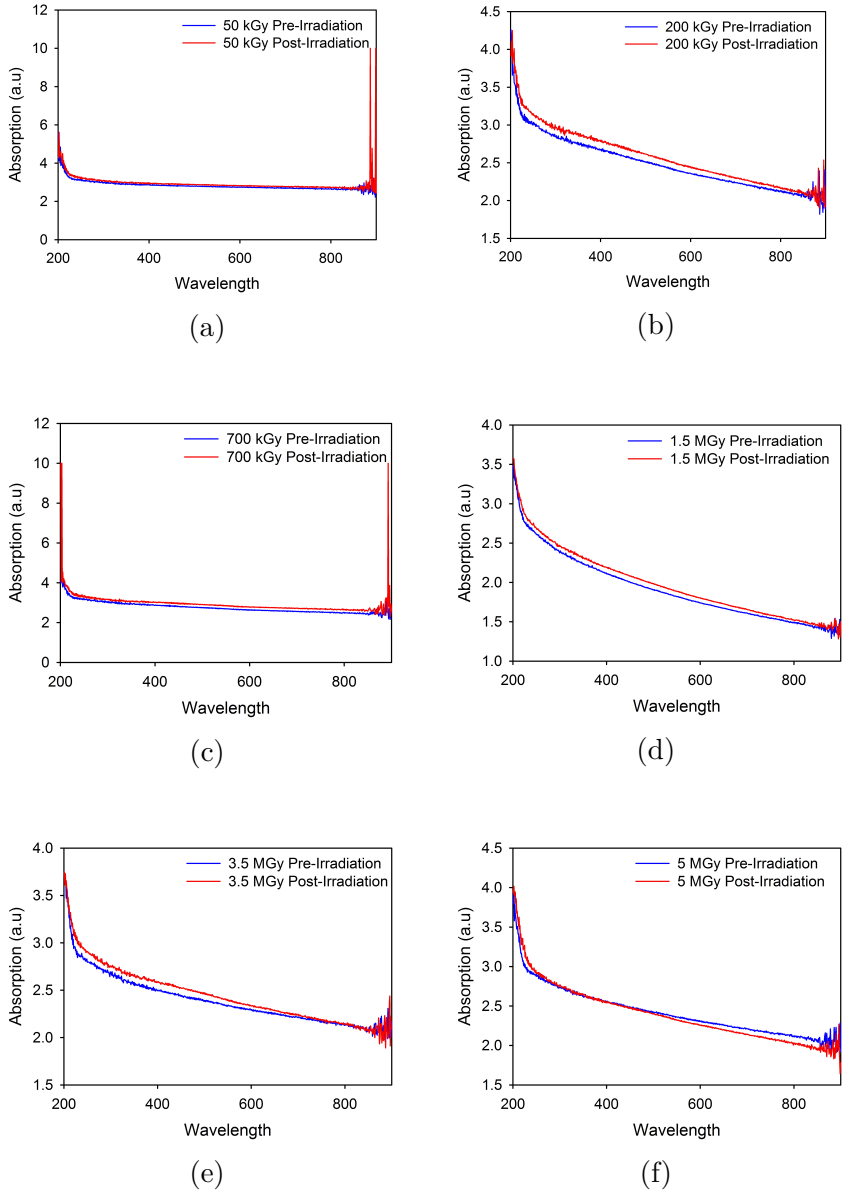


Figure 5.21: Quartzite absorption spectra measured before and after electron beam irradiation for a) 50 kGy, b) 200 kGy, c) 700 kGy, d) 1.5 MGy, e) 3.5 MGy, and f) 5 MGy

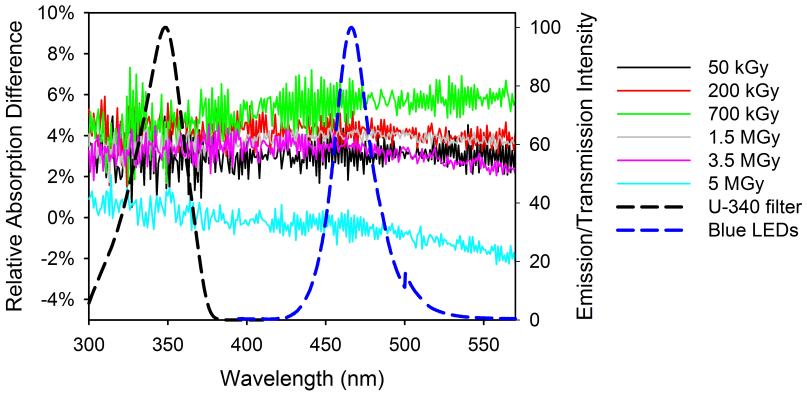


Figure 5.22: The relative increase in absorption as a function of electron beam dose. There is at most a 6% increase in absorption (700 kGy), however this is not enough to explain the changes in luminescence output and sensitivity observed in the experiments. The emission window of the blue LEDs as well as the transmission window of the U-340 filters are also plotted to assist the reader.

# References

Agostinelli, S., Allison, J., Amako, K., Apostolakis, J., Araujo, H., Arce, P., et al., (Geant4 Collaboration). Geant4 ,Äì a simulation toolkit *Nuclear Instruments and Methods in Physics Research Section A* 2003:**506(3)**;250-303

Autzen M., Guérin G., Murray A. S., Thomsen K. J., Buylaert J.-P., Jain, M. The effect of backscattering on the beta dose absorbed by individual quartz grains. *Radiation Measurements* 2017:**106**:491-497

Autzen, M. Murray, A.S., Guérin, G., Baly, L., Ankjærgaard, C., Bailey, M., Jain, M. and Buylaert, J.-P. Luminescence dosimetry: does charge imbalance matter? *Radiation Measurements* 2018 in-press

Bailey, R.M. Paper I - simulation of dose absorption in quartz over geological timescales and its implications for the precision and accuracy of optical dating *Radiation Measurements* 2004:**38**:299-310

Hansen, V., Murray, A., Buylaert, J.P., Yeo, E.Y., Thomsen, K. A new irradiated quartz for beta source calibration *Radiation Measurements* 2015:**81**:123-127

Pagonis, V., Chen, R., Wintle, A.G., Modelling thermal transfer in optically stimulated luminescence of quartz *Journal of Physics D: Applied Physics* 2007:**40**:998-1006

Pagonis, V., Wintle, A.G., Chen, R., Wang, X.L. A theoretical model for a new dating protocol for quartz based on thermally transferred OSL (TT-OSL) *Radiation Measurements* 2008:**43**:704-708

Reimer, L., *Scanning Electron Microscopy (PW Hawkes Ed.)*, Springer, Berlin, 1985

Stevens, T., Buylaert, J.-P., Lu, H., Thiel, C., Murray, A., Frechen, M., Yi, S., Zeng, L. Mass accumulation rate and monsoon records from Xifeng, Chinese Loess Plateau, based on a luminescence age model *Journal of Quaternary Science* 2016:**31**:391-405

Vigouroux, J.P., Jollet, F., Duraud, J.P., Le Gressus, C. Influence of ion implantation and gas exposure on the charge in silicon oxide created by electronic excitation *Scan. Electr. Microsc.* 1986:**4**:1311-1317

Wintle, A. G., Murray, A. S. A review of quartz optically stimulated luminescence characteristics and their relevance in single-aliquot regeneration dating protocols *Radiation Measurements* 2006:**41(4)**:369-391

# Chapter 6

# Summary

The overall aim of this thesis is to provide a better understanding of electron trapping and recombination processes in sedimentary quartz in order to improve quartz luminescence geochronology. This aim was split in two primary objectives: I) identifying contributions to intrinsic over-dispersion in single-grain dose distributions from natural minerals such as quartz and feldspar and II) to investigate the effects excess charge can have on quartz luminescence. The research was carried out using radiation transport models (Geant4 and MCNP) to simulate natural and laboratory irradiations of quartz grains of various sizes and shapes in order to provide quantitative estimates of dose and charge deposition. These simulation results were coupled with luminescence production models to predict the expected luminescence behaviour as a function of irradiation history. Modelling predictions were then tested by experiments. Here the major findings of each of the four chapters in the thesis, and Appendix A, are first summarised, and finally the overall conclusions are presented and possible directions for future research discussed.

## Chapter 2: The effect of backscattering on the beta dose absorbed by individual quartz grains

Chapter 2 describes Geant4 modelling and experimental observations used to investigate the over-dispersion of single-grain dose distributions under different irradiation conditions. The initial set of experiments dealt with irradiation on different substrates and showed that both dose rate and over-dispersion increased with increasing substrate Z. These observations are

consistent with predictions from Geant4 modelling, which also showed that both grain size and shape play a role in the deposited dose. This modelling indicates that larger grains are less sensitive than smaller grains to changes in substrate.

However, when the grain volume was kept constant for different shapes, the range of deposited doses decreased with increasing substrate Z, this was unexpected. Since real sediments are mixtures of grain sizes and shapes, the dependence on shape and volume should result in a higher grain-to-grain dose dispersion, especially during laboratory irradiations when using backscattering substrates with high Z. This supports the observation that the over-dispersion increases with increasing atomic number of the backscattering substrate. Geant4 modelling was used to derive the electron spectra incident on grains (including the backscattered component) for irradiations on the different substrates; this showed a softening of the spectrum with increasing Z, i.e. spectra increasingly dominated by lower energy electrons. It was thus hypothesised that the observed increase in over-dispersion may be linked to an increase in the low energy component.

This hypothesis was explored further in the second part of the chapter, which investigated the effect of attenuating the incoming beta spectrum using thin sheets of lead. Using a 0.2 mm thick lead attenuator modelling indicated an overall softening of the incoming spectrum. This attenuation led to a significant increase in the over-dispersion, from 5.8% to 12.6%. Further softening of the spectrum using 0.4 mm of lead resulted in, probably, no further increase in the over-dispersion. These observations provide a further indication that low energy electrons play a role in the over-dispersion of single-grain dose distributions.

## Chapter 3: Towards the origins of over-dispersion in beta source calibration

This chapter continues investigations into laboratory over-dispersion by experimentally investigating variations in apparent beta source dose rates using multi-grain aliquots. For grain diameters above 100 µm, the multi-grain apparent dose rate decreased by $0.07\,\%\,\mu m^{-1}$. This would lead to an expected upper limit in the difference in dose rate of 5% in the grain size fraction diameter range of 180 to 250 µm commonly used luminescence dating. This is only about half of the observed over-dispersion, and in practice

the range in dose rates will be substantially smaller than this.Variations in dose rate arising from variations in backscattering medium can be eliminated by ensuring a monolayer of grains is mounted on the substrate, and so it was concluded that neither variations in backscatter, nor variations in grain size, are likely to explain the observed over-dispersions in laboratory dose rates.

Using Geant4 modelling, it was deduced that the net electron spectrum is likely to move closer to that experienced by grains in nature as the substrate Z increases but the importance of this was not tested. Irradiating on high Z substrates results in a higher dose rate to the aliquot; the dose rate can be increased up to 40% by using platinum cups instead of stainless steel cups, or 75% when compared with Al cups. This has practical implications for luminescence dosimetry as it can greatly reduce the irradiation times, which is often the largest contributor to sequence run time. However, as was observed in the previous chapter, modelling suggests that irradiating on high Z substrates increases the dose rate dependence on grain size and grain shape.

Finally, it was observed that the apparent beta dose rate to feldspar was 15% lower than that to quartz. This is unexpected as modelling suggested that the absorbed dose to both minerals should be identical. This difference presumably arises from a difference in the luminescence efficiency between beta and gamma radiation for the two minerals; this is of considerable potential importance, and requires further investigation.

# Chapter 4: Luminescence dosimetry: does charge imbalance matter?

This chapter describes, for the first time, the existence of charge imbalance in retrospective dosimetry, and how it might affect the luminescence response from natural minerals. Previous and current luminescence models implicitly or explicitly assume charge neutrality during irradiation, leading to identical trapped populations of electrons and holes. However, modelling the beta irradiation of quartz grains using Geant4 showed that the deposition of an excess of electrons during both natural and laboratory irradiations is very likely. From this, it was hypothesised that, once all electron traps were saturated, these excess electrons would recombine with trapped holes, and so lead to a progressively smaller hole population. Since luminescence is the result of the recombination of electrons with holes, a decrease in the hole population would be expected to lead to a reduced luminescence out-

put and a reduced sensitivity. In addition, increasing electron retrapping rates would result in a slower decay curve.

These qualitative predictions were first tested using a 200 keV electron beam irradiation of 40-63 µm quartz grains. This grain size range was chosen because the predicted range of 200 keV electrons in quartz is ∼80 µm, suggesting that the entire grain volume would be exposed to the beam; with this facility doses of up to 5 MGy were possible. Modelling predicted that the excess electrons deposited by the electron beam, expressed as a fraction of the total number of ionisations, was similar to that under the beta source in the Risø TL/OSL reader.

In all 3 samples employed in the electron beam experiment, both the luminescence response to the electron beam irradiations and the subsequent response to a small beta dose, decreased substantially at large doses. Although it might be possible to explain these observations in terms of hole redistribution (rather than the using up of holes by excess charge) the OSL stimulation curves were also observed to decay more slowly with time at larger doses, consistent with the prediction of increased retrapping, and so these experiments are regarded as giving qualitative support to the hypothesis of a reduced hole population as a result of excess charge.

## Chapter 5: The history of charge deposition in quartz and its effect on luminescence production

This chapter expanded on the work described in Chapter 4. Modelling was first expanded to include the variation of charge imbalance with grain size in more irradiation geometries. This showed that the relative charge imbalance decreased with increasing grain size (i.e. small grains have a larger charge imbalance than large grains) in nature, and in the laboratory when the grains are irradiated with a spectrum of energies. At larger grain sizes the amount of relative excess was similar for both natural and laboratory irradiations, and it ceased to be dependent on grain size. This independence of grain size set in at smaller grain sizes in laboratory irradiations, and smaller grain sizes remained more charge negative in natural irradiations than in the laboratory.

This indicated that, at least for small grains, natural and laboratory irradiations are not similar in terms of total electron density, assuming that the ionisation rates remained constant. Modelling using a mono-energetic electron beam with a primary energy ranging from 100 - 500 keV, suggested

that for a fixed energy, the larger grains had a larger charge imbalance because larger grains were able to stop more of the incoming electrons. When the primary energy was increased, there was a corresponding decrease in the degree of charge imbalance due to both the larger penetration depth of the incoming electron and the increase in energy absorbed.

However, essentially charge neutral irradiations are possible if irradiations are performed using a gamma source; this was shown by modelling quartz irradiations using the well-calibrated $^{137}$Cs point source. This irradiation geometry is used to deliver a known dose to the quartz used to calibrate beta sources. This modelled gamma irradiation delivered a charge neutral dose, meaning that during beta source calibration, the quartz beta dose (with $\sim$2% excess electrons) is compared with an essentially charge neutral gamma dose. At this stage, it is unknown whether this asymmetry is of significance to calibration.

These model predictions of total ionisation and charge imbalance were, for the first time, used as input to luminescence production equations to model and predict the effect of excess electrons during irradiation. Excess electrons were shown not to significantly influence the trapping of electrons with increasing dose. After saturation of all electron traps (at $\sim$4 kGy), the hole population then began to decrease linearly with dose. Not surprisingly, the hole population decreased faster with an increasing proportion of excess electrons, confirming the qualitative expectations of Chapter 4. This was again tested experimentally by irradiating quartz aliquots with both 200 and 100 keV electrons; this time the dose range was extended to cover from 50 kGy to 5 MGy with a higher dose resolution than previously. At 200 keV, this experiment showed, as before, a depression of both luminescence output and sensitivity at high doses.

But the higher dose resolution in this experiment made it clear that the decrease was not linear, but rather asymptoted towards a finite value, suggesting no further reduction in hole population. It was suggested that this was because the excess charge had built up to such a degree that it was able to prevent further 200 keV electrons entering the grains. It would take $\sim 2.8 \times 10^8$ excess electrons to build up an electric field around a 50 µm grain capable of completely stopping a 200 keV electron. This is the excess charge deposited by $\sim$3.5 MGy, and it was concluded that charge buildup must affect the actual dose rate at high prior doses. This conclusion was tested by repeating the experiment with a lower energy (100 keV) beam. The luminescence signals following the lower energy irradiations showed a smaller decrease in luminescence output and sensitivity even though the degree of charge imbalance was predicted to be greater; these observations supported the hypothesis that the excess charge was sufficient to repel the

incoming electrons and so effectively prevent further dosing.

## Appendix A: A New Automated System for Combined Luminescence and Exo-Electron Measurements

Designing, developing and characterising the new exo-electron detector, REES, also formed a significant component of this thesis. Unfortunately there was insufficient time after the characterisation of the detector to then employ it to investigate luminescence production and charge imbalance at the level of individual grains. Nevertheless, it was possible to demonstrate a correlation between the exo-electron signal and OSL signal from single grains of quartz. Furthermore, a few grains were observed which had no significant OSL signals but gave strong exo-electron signals; this was unexpected. Such grains might give insight into the origins of over-dispersion by directly measuring the trapped charge population without relying on recombination.

We also observed that the exo-electron signal was affected by the stimulation wavelength, showing an increase when the blue LEDs were used instead of the green laser. Increasing the photon energy, i.e. decreasing the wavelength, of the focussed laser is likely to help achieve stronger exo-electron signals from more individual grains - an important first step to using this new detector to investigate the dispersion in trapped electron populations.

## Conclusion and Outlook

The overall aim of the thesis was to provide a better understanding of charge trapping and recombination in natural minerals such as quartz and feldspar by investigating the origins of intrinsic over-dispersion in single-grain dose distributions as well as the effects excess charge can have on luminescence production.

Some part of over-dispersion appears to be linked to the low energy component of the beta spectrum used to irradiate the grain. The over-dispersion increases with increasing substrate Z, a further indication of the importance of the low energy component. Grain size and shape was also found to be important when determining over-dispersion. These experi-

ments and models all suggest that close control of grain size and irradiation substrate is necessary to minimise these sources of over-dispersion.

Excess charge is a consequence of irradiating with electrons and has an effect on the luminescence output and sensitivity as the grains accumulate dose. Whether these effects are of significance in nature can now be tested, e.g. by examining the sensitivity of unaltered sandstones with age.

Although this thesis has provided new insights into charge trapping and recombination in natural minerals there is still a lot of interesting work that can be done to provide a more complete understanding of these processes:

- It is unknown if the sensitivity reduction observed after irradiation to high doses with low energy electrons is reversible. Experiments to test this would involve temperature annealing and monitoring the exo-electron response. Is this process reversible in nature, without significant heating? What are the implications for trap stability?

- While it was observed that the over-dispersion increased with the atomic number of the backscattering material, the possible effect of preconditioning of the grain (with a known prior charge imbalance) on over-dispersion can now be investigated. This could be readily tested by using samples with a high degree of charge imbalance as the initial material.

- This thesis did not attempt to measure directly the net charge in natural minerals after they were irradiated. This was in part because of uncertainty concerning the self-neutralisation that must occur by at the surface of charged grains. Measuring the polarizability of quartz irradiated under different circumstances might provide a method for directly measuring the excess charge.

- Finally, the single-grain exo-electron work resulted in some preliminary but very encouraging results. Using the HV-modulation at the single-grain level it is possible to build OSL and exo-electron dose response curves and thus dose distributions. Whether the over-dispersion will be different for the two signals has not yet been tested but this has the potential to yield new, fundamental knowledge regarding intrinsic over-dispersion - is it already present in the trapped electron population, or does it arise as a result of recombination?

# Appendix A

# A New Automated System for Combined Luminescence and Exo-Electron Measurements

M. Autzen[1], N. R. J. Poolton[1], A. S. Murray[2], M. Kook[1], and J.-P. Buylaert[1,2]

[1] *Center for Nuclear Technologies, Technical University of Denmark, DTU Risø Campus, Denmark,*
[2] *Nordic Laboratory of Luminescence Dating, Department of Geoscience, Aarhus University, Denmark*

---

**Abstract:** The measurement of OSL/TL relies on the initial trapping and subsequent release and recombination of charge in a suitable crystal structure. These measurements allow us to estimate the dose which the crystal has been subjected to and its age. During such processes, however, electrons can be emitted from the sample surface; the ability to measure such exo-electrons can provide information regarding the trapping process, as well as an alternative method of measuring trapped charge. Ideally, TL/OSL can be measured alongside exo-electrons.
We will present a new design for an exo-electron detector compatible with the classic Risø reader stimulation head featuring multiple anode configurations and the option for high-voltage modulation to reduce the UV component during TL/OSL measurements. We will also present, for the first

time, measurements of exo-electrons from single grains of quartz which may provide insights into the origins of the over-dispersion in single-grain dose distributions.

---

## A.1 Introduction

Here we describe a new instrument for the simultaneous measurement of electrons and photons emitted from minerals during optical and/or thermal stimulation. In trapped charge dosimetry, as energy is absorbed from ionising radiation, charge is trapped at defects in the crystal lattice of wide band gap insulators. This trapped charge can be released by stimulation with heat or light leading to the emission of photons, called thermoluminescence (TL) and optically stimulated luminescence (OSL), respectively. It can also be probed directly in the trap using Electron Paramagnetic Resonance (EPR/ESR) (e.g. Ikeya, 1991). These phenomena are known for both natural (e.g. quartz and feldspars, Ikeya, 1975; Tsukamoto et al., 2015, 2017) and artificial materials (BeO, $Al_2O_3$, etc. Ikeya, 1991; Milsch et al., 1990; McKeever, 1985). Luminescence relies on the recombination of an electron with a hole trapped at a separate site and is thus only an indirect measure of the trapped charge. On the other hand, exo-electron emission (Oster et al., 1999), where stimulated electrons escape the crystal surface, does not depend on recombination, and so provides a direct approach to the measurement of stimulated electrons. Thus, a comparison of changes in exo-electron and luminescence response to dose should provide valuable information about luminescence efficiency, and recombination pathways and probabilities.

Exo-electron emission describes the release of electrons from a surface that has been exposed to ionising radiation This can be either a one-step or two-step process, most likely either photon or phonon stimulation, or photon-phonon (thermally assisted photo eviction) or phonon-phonon process (Oster et al., 1999). Other processes such as photon-photon stimulation are possible but unlikely (Oster et al., 1999). In the one-step model, an electron is stimulated from a trap by heat or light, and enters the conduction band. If it has sufficient remaining energy to overcome the electron affinity it can escape the surface (Figure A.1). In the two-step model the electron is

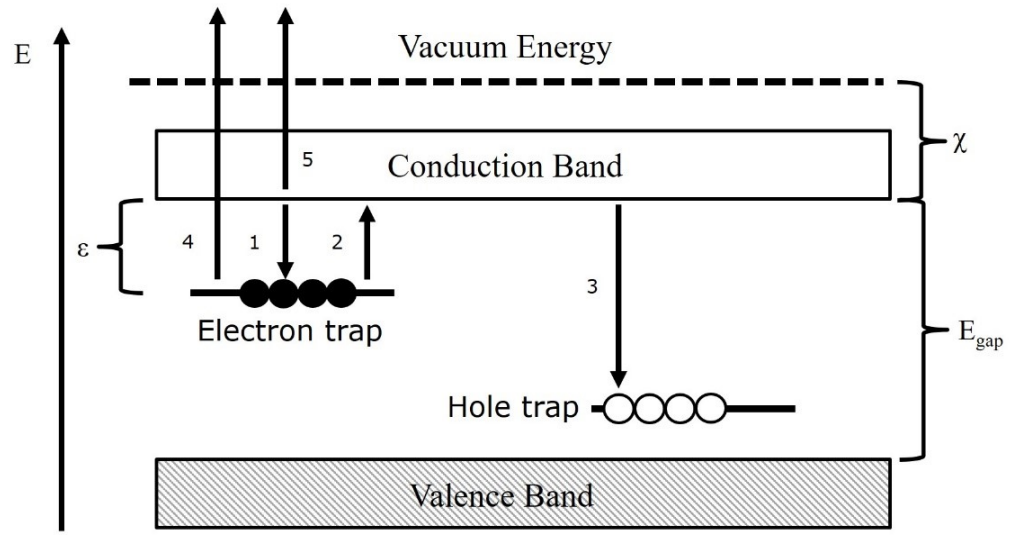


Figure A.1: Band diagram showing the pathways of exo-electrons and luminescence emission in wide band-gap materials. Trapping of electrons in traps occurs via (1). These electrons can then be stimulated into the conduction band (2) using heat or light. From the conduction band they can recombine with trapped holes and emit luminescence (3). Exo-electron emission (4, one-step process) and (5, two-step process) does not rely on recombination but (4) is only possible if the absorbed stimulation energy is greater than the sum of the trap depth ($\epsilon$) and electron affinity ($\chi$).

only given sufficient energy to enter the conduction band. There it acquires sufficient additional energy to overcome the electron affinity (Figure A.1).

Exo-electrons arising from thermal stimulation (here for consistency TSE rather than more commonly used TSEE) were first observed by Tanaka in the period 1935 to 1940 (Oster et al., 1999); he observed the slow emission of electrons from the surfaces of metal oxides which had previously been exposed to ionising radiation. A comprehensive list of materials emitting TSE can be found in Becker (1970).

When exo-electrons leave the crystal surface they will normally react rapidly with any electrophilic species such as water vapour. But if this reaction is minimised, these exo-electrons become available for measurement, for instance using an electron multiplier or a gas counter (Turner 1995). TSE studies on natural materials have been carried out on ceramics (Zastowny et al., 1998) and fired quartz (Zimmerman, 1971) using gas counters. Davies (1983a) studied powdered human enamel and enameloid from a Great White shark without any chemical or thermal treatment. In Davies (1983b) he

chemically treated sediments with 0.1 M hydrochloric acid and 30% hydrogen peroxide to remove carbonate and organic matter before TSE measurements. Ankjærgaard et al. (2006, 2008, 2009) and Tsukamoto et al. (2010) also used a gas counter and chemically cleaned quartz and feldspar extracted from sediments for their measurements. Ankjærgaard et al. (2006) were the first to measure Optically Stimulated Exo-Electrons (OSE). Their exo-electron detector was used with an automated Risø TL/OSL reader; this combination allowed automatic irradiation, thermal pretreatment and repeated simultaneous measurement of TL/OSL with TSE/OSE. However the luminescence signals were contaminated by a strong UV gas-fluorescence signal resulting from the ionisation of the counting gas (argon) during electron acceleration; de-excitation produces gas fluorescence (see Fig. 4 in Ankjærgaard et al., 2006). As a result, luminescence measurements had to be carried out separately from exo-electron measurements to avoid the contaminating UV signal. This had serious implications for the measurement of naturally irradiated materials (such as are used in luminescence dating): when measuring aliquots of such material, it was not possible to obtain a TL/OSL signal and a TSE/OSE signal from the same aliquot during the same measurement cycle. The detector head was also only suitable for broad-field stimulation with LEDs; in particular it was not compatible with an attachment used for the automatic laser stimulation of individual sand-sized grains (Bøtter-Jensen et al., 2000, 2003).

Here we present a new Risø Exo-Electron System (REES), based on a flow-through gas detector operated in the Geiger-Müller (GM) region. The system has a modular design that allows the user to easily change the distance from the gas-detector anode to sample or switch to a different anode configuration, with the intention of maximising detection efficiency for both exo-electrons and luminescence. It also employs high-voltage modulation to separate the OSL signal from UV fluorescence, and it can be used with both broad-field and focussed laser beam stimulation.

## A.2 Design and Construction

### A.2.1 Design Specifications

REES was designed with several goals in mind: (i) it should be compatible with the existing automated Risø TL/OSL reader able to accommodate up to 48 individual subsamples (aliquots) on a turntable, (ii) it should be capable of measuring TL/OSL and TSE/OSE simultaneously from the same aliquot - this suggests that the UV fluorescence from the Ar filler

gas should be minimised during luminescence measurement, (iii) since the UV fluorescence is caused by the acceleration of exo-electrons, the detector should be able to measure the UV fluorescence as a surrogate for exo-electrons, and finally (iv) the detector must be sufficiently sensitive to detect exo-electrons resulting from typical burial doses (e.g. 10 Gy) from natural minerals including quartz and feldspar. Items (ii) and (iii) in the above are, of course, to some degree incompatible with each other.

### A.2.2 Design of REES

REES is based around a GM detector mounted inside the Risø TL/OSL reader stimulation head for combined luminescence and exo-electron measurements. In order to minimise the contamination of the luminescence signal by gas fluorescence, three different anode configurations were chosen to physically separate the volume in which the UV is generated, from the optical path of the luminescence. As well as this spatial separation, the HV supply to the anode can be pulsed during stimulation (0-3 kHz, user defined mark/space ratio, rise/fall time of applied voltage approx. 3 µs). This is intended to allow the measurement of TL/OSL in the absence of electron multiplication (and so UV fluorescence) during the off-period. By interpolation, the uncontaminated luminescence signal can be subtracted from the combined UV and luminescence measured during the on-period, to give a pure gas fluorescence signal - providing a separate measurement of TSE/OSE. The point anode design (see later sections) also features a second PMT, which directly measures the UV generation around the anode (Figure A.2a).

Although REES is modular and allows for different anode configurations there are several parts in common. The detection volume is contained within a quartz tube glued to the bottom flange in the stimulation head of a Risø TL/OSL reader; the entire reader volume, including detector, can be evacuated down to 0.01 kPa prior to flushing with counting gas. The detection unit itself can be removed from the quartz tube to change the anode configuration or replace the 100 µm diameter anode wire.

The detection unit is built around a central, solid quartz rod, which also functions as a central light guide for collecting luminescence from the sample (Figure A.2). The different anode configurations are supported by separate quartz pipes, to reduce the risk of arcing to the earthed surfaces, and are supported by a secondary platform held in place on the central light guide. Vertical adjustment of the quartz pipes containing the anode wire allows easy manipulation of the sample/anode distance. The sample is located at the bottom of the detection volume; this is lifted into position by a movable

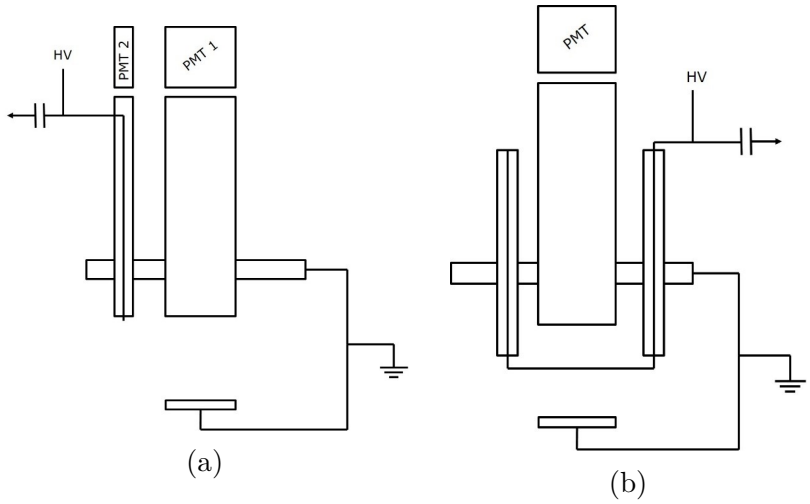


Figure A.2: Schematic of REES. a) point anode configuration with separate PMT (PMT2) to detect gas fluorescence. b) linear and circular anode configuration. The central light guide located under the PMT collects the TL/OSL. At the bottom of the view is the sample disc which sits on a heater plate connected to earth.

heating plate (part of the reader platform). A MACOR ring (not shown) is placed around the sample to reduce the risk of arcing from the anode to the corners of the bottom flange.

A schematic diagram illustrating the integration of REES with the Risø TL/OSL reader is shown in Figure A.3. Exo-electrons are collected at the anode and the resulting voltage pulse is passed through a Spectrum Techniques Inc. GM Tube Pulse Inverter (model GPI) and transformed into TTL pulses before passing to the control computer (Minisys, see Figure A.3). The measurement chamber is first evacuated and thereafter flushed with a 1% Ar-isobutane gas mixture at a flow rate of 0-0.5 l $\mathrm{min}^{-1}$, while maintaining a set pressure (typically 100 kPa) using an Alicat PC15PSIA-D/5P flow-meter. The standard programmable control software (Sequence Editor) running on the host PC has been modified to provide automatic control of HV modulation and synchronised counting of pulses from the anode and from the luminescence detector.

### A.2.3 Modelling

Electric field modelling of each anode configuration was done using COMSOL Multiphysics©[1] to predict the functioning of the various configurations.

[1]COMSOL Multiphysics © v. 5.2. www.comsol.com COMSOL AB, Stockholm, Sweden

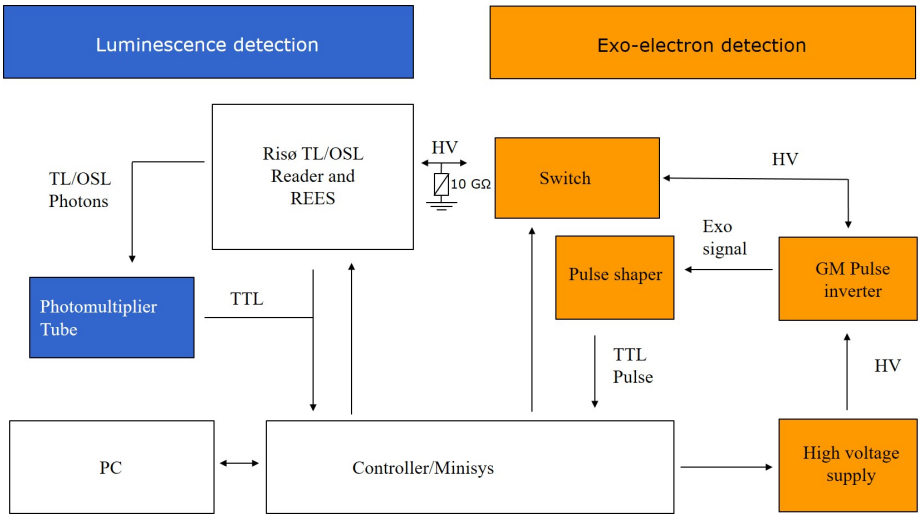


Figure A.3: Schematic of REES integration with the standard Risø TL/OSL measurement platform. It is worth noting that the 10 GΩ resistor allows the exo-electron signal to decay much faster than the modulation time when using pulsed HV.

This allows us to confirm that the electric field lines (presumably tracked by the exo-electrons and cascade electrons) from the sample will reach the anode. Figure A.4 shows the modelling results and a bottom view image of the different anode configurations.

### Ring anode

The ring anode configuration is one option for spatially separating TL/OSL and TSE/OSE by moving the anode away from the central light guide (Figures A.4a, A.4d and A.4g). It is possible to change the radius (typically ∼7 mm) of the ring. Here we can see that the electric field lines do not go through the central light guide, although there is some electric potential, but primarily terminate at the anode.

### Point Anode

The point anode configuration is another option to spatially separate TSE/OSE from the TL/OSL but it also provides a secondary method for detection of TSE/OSE using gas fluorescence (Figures A.4b, A.4e and A.4h). Most of the gas fluorescence will be generated in the region of the point anode as the argon gas is ionized and the resulting UV photons are guided up the quartz pipe and reflected into a separate, secondary PMT. This may be

a more sensitive method for detecting TSE/OSE than direct electric measurements. The radial location of the anode is fixed due to location of the quartz pipe, but it is possible to adjust the length of wire exposed to the counting volume. Using a point anode, flush with the light guide, all the field lines from the sample terminate at the anode tip; although the quartz tube intersects a few lines, only a small fraction of accelerating electrons in the avalanche will follow these lines and so will not be fully imaged on the anode. Since the detector operates in GM mode (i.e. charge saturation) moderate fluctuations in the number of accelerated electrons are very unlikely to affect the presence or absence of an anode pulse. Thus there is unlikely to be a significant advantage in exposing more wire, but there will be an increased risk of arcing to the ground plate.

#### Linear Anode

The linear anode design is shown in Figures A.4c, A.4f and A.4i. This anode configuration is similar to that used by Ankjærgaard et al. (2006, 2008, 2009) and Tsukamoto et al. (2010), except that it does not have a grid cathode on the opposite side of the anode from the sample. This configuration does not attempt to spatially separate TL/OSL from TSE/OSE as the other designs do, but it may provide greater detection efficiency due to the proximity of the anode to ground - the linear anode design has no horizontal offset and is thus closer to grounded surfaces compared to the point or ring anode at the same vertical distance. Thus for the linear anode, it is more likely that exo-electrons emitted obliquely will be accelerated sufficiently to cause an avalanche before becoming attached to an electrophilic impurity in the gas; on the other hand, it is possible that this proximity will also increase the chance of arcing.

It can be seen from Figure A.4f that all the field lines originating from the sample terminate at the anode wire and that due to the position of the wire there is a very low probability of field lines passing through the central light guide. The risk of arcing appears to be greatest where the anode makes a sharp turn when coming out of the quartz pipes as this increases the local field strength.

## A.3 Characterisation of the instrument

Here we document the detector characteristics (efficiency curve, arcing voltage, pressure dependence, HV modulation, etc.) of the REES gas detector based system.

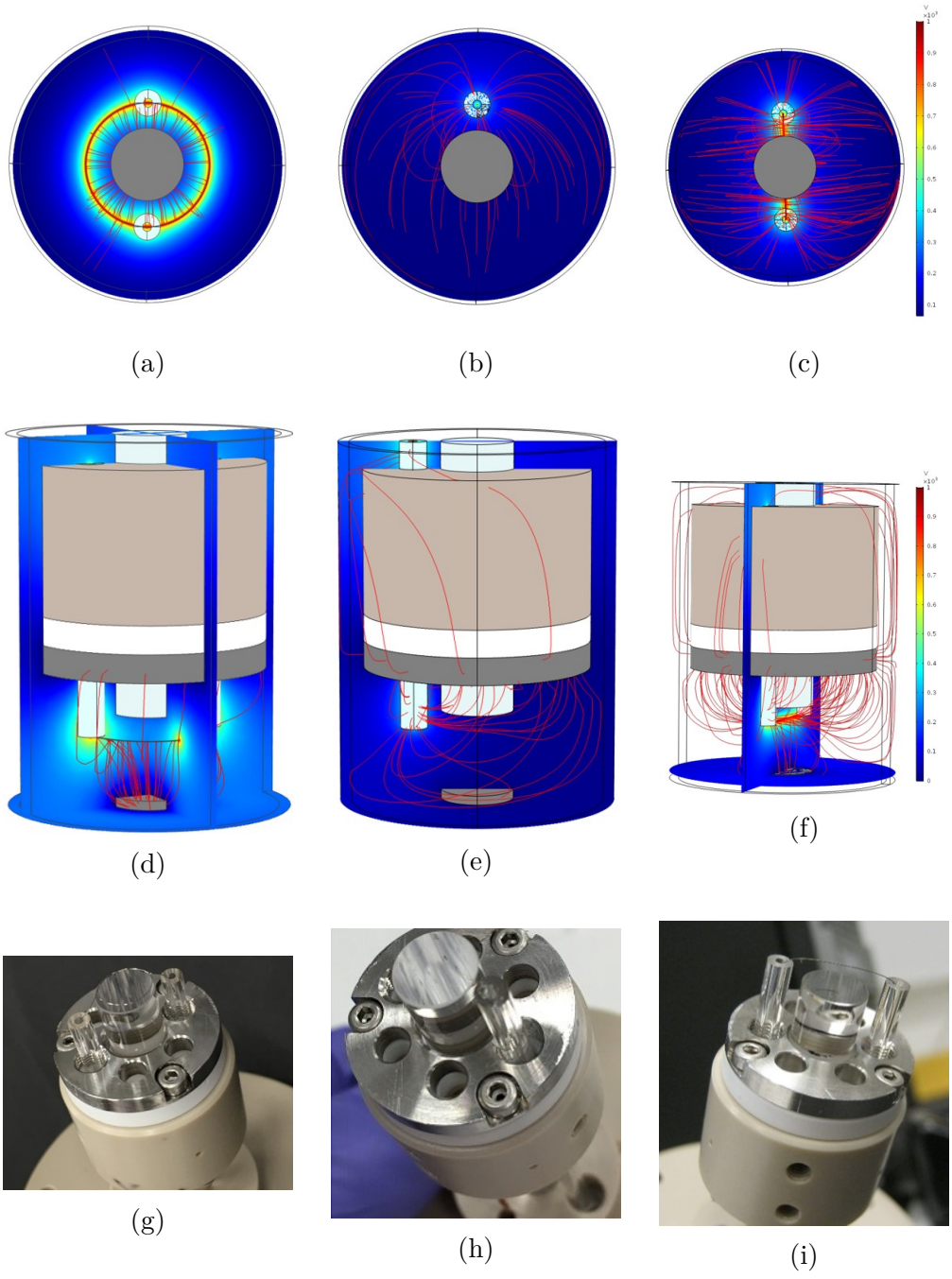

Figure A.4: Electric field modelling and photographs of ring anode (a,d,g), point anode (b,e,h) and linear anode (c,f,i) configurations. a, b, and c show a view of the detector from below, with the sample disc in the centre. d, e, and f show 3D modelling of the electric field lines. g, h, and i are photographs of the three anode configurations

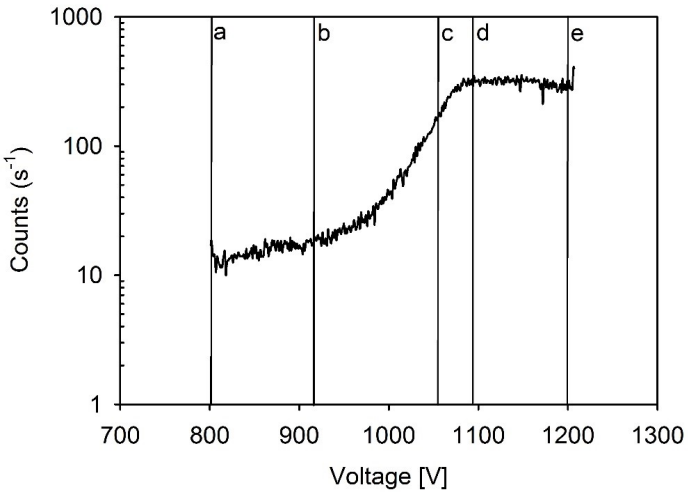


Figure A.5: Example of the variation in counting efficiency with anode voltage produced using REES and a $^{63}$Ni ($\bar{E} = 17\,\text{keV}$) source deposited on stainless steel and held at 50 °C. The curve can be divided into several regions: a) ion-chamber, b) proportional, c) semi-proportional, d) Geiger plateau, and e) electrical breakdown.

A gas detector can operate in several different regions, each with certain advantages and disadvantages. These regions are usually identified by the relationship of pulse height with applied voltage, but the efficiency relationship follows a similar shape, and so the traditional region names remain useful. In Figure A.5 these regions are illustrated using an efficiency curve measured using REES with a $^{63}$Ni source ($\bar{E} = 17\,\text{keV}$, $E_{max} = 66\,\text{keV}$, average CSDA range in argon $\sim$0.5 cm); each region has a different relationship between efficiency and voltage.

In the ion-chamber region, the number of ionization events in the gas is proportional to the initial electron energy, and so the total charge mirrored at the anode in each pulse is proportional to the energy of the individual electrons emitted by the source. Unfortunately, the efficiency in this region is very low, because electrons are not accelerated sufficiently to induce gas multiplication and many are lost to recombination. In the proportional counting region (b), multiplication does take place, and so progressively fewer electrons are lost to recombination as the voltage increases; this gives rise to a steady increase in efficiency with voltage. In the semi-proportional region (c), between the proportional and Geiger region, almost all electrons give rise to a signal, but the amplitude of each pulse can vary, and so some may still fall below the counting threshold. Finally, in the Geiger region

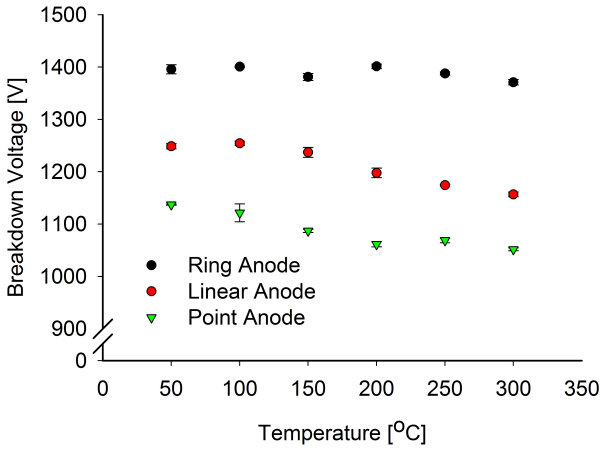


Figure A.6: Dependence of breakdown voltage on sample temperature The error bars are the standard error for three runs.

(d), an electron multiplication avalanche saturates the gas surrounding the length of the anode. As a result, all pulses have the same amplitude, and this is independent of the applied voltage; since essentially all emitted electrons give rise to a pulse, the count rate is independent of the applied voltage. This is the preferred region for our experiments because it is the most sensitive to the very low energies expected from exo-electrons. At increasingly higher voltages, electrical breakdown begins (e).

### A.3.1 Breakdown using thermo-ionic emission

Breakdown, or arcing, occurs when the voltage reaches the threshold for spontaneous breakdown in the gas. This voltage is dependent on pressure, temperature and the distance to the grounded sample plate. Since we keep the pressure, and the sample to anode distance fixed, we need only investigate the dependence on temperature, using empty, undosed stainless steel cups as the cathode. These are the same cups as are used for routine luminescence and exo-electron measurements and should provide a good indication of the manner in which the breakdown voltage can be expected to occur at different temperatures. The addition of exo-electrons from materials (usually grains) held in the steel cups may slightly lower this arcing voltage. The temperature dependence was investigated by bringing the cup to a given temperature between 50 °C and 300 °C and then increasing the voltage at a rate of $1\,\mathrm{V\,s^{-1}}$ until arcing is achieved (the chamber was kept at constant pressure of 1000 mbar). This experiment was repeated for the three different anode configurations and the results are shown in Figure A.6.

The linear and point anodes show a drop in breakdown voltage as the temperature is increased while the ring anode remains stable around 1400 V. This means that, when using the ring anode, it would be possible to keep a significantly higher fixed voltage across the temperature ranges normally used in OSL dating applications (at least from the point of view of breakdown) than for the other two anode configurations.

### A.3.2 Temperature dependence of efficiency

Luminescence production from quartz and other natural materials is known to be affected by a variety of parameters, including thermal pretreatment and measurement temperature (Spooner, 1994; Chen and McKeever, 1997 p. 74; Wintle and Murray, 1998, 2000). As a result, exo-electron measurements may also be affected by sensitivity changes, since luminescence production and exo-electron emission are competing processes (Figure A.1). In addition, thermal assistance is likely to allow electrons from deeper below the crystal surface to escape, increasing the crystal volume available as an exo-electron source; thermal assistance can also help electrons to escape the surface even if the stimulation light does not deliver sufficient energy (Oster et al., 1999). But to investigate these dependencies, it is clearly important that the detector efficiency is temperature independent, or at least that any dependence is well known. To investigate such efficiency dependence, the $^{63}$Ni source discussed above was used as a temperature-independent source of electrons. Using this source, we have constructed efficiency curves as a function of temperature for each different anode configuration.

It can be seen from Figure A.7a and Figure A.7b that as the temperature increases we achieve proportional counting at a lower voltage. Assuming that the thermionic background emission of electrons from stainless steel does not change significantly in this low temperature region (50-290 °C), these data suggest that the gain of the gas increases with increasing temperature, presumably because the argon becomes easier to ionize. Figure A.6 shows that the arcing voltage also decreases with increasing temperature for an empty, undosed stainless steel cup; the decrease is most pronounced for the linear and point anode configurations. The anode and UV signals appear to follow separate efficiency curves. At 1100 V, the anode signal at 50 °C is firmly on the plateau while the UV curve is still climbing, the reason for this is unknown.

The detection efficiencies for the different anodes are presented in Table A.1. The measurements were performed by keeping the $^{63}$Ni source at 125 °C and increasing the voltage by 1 V s$^{-1}$ and using the count rates in the GM region.

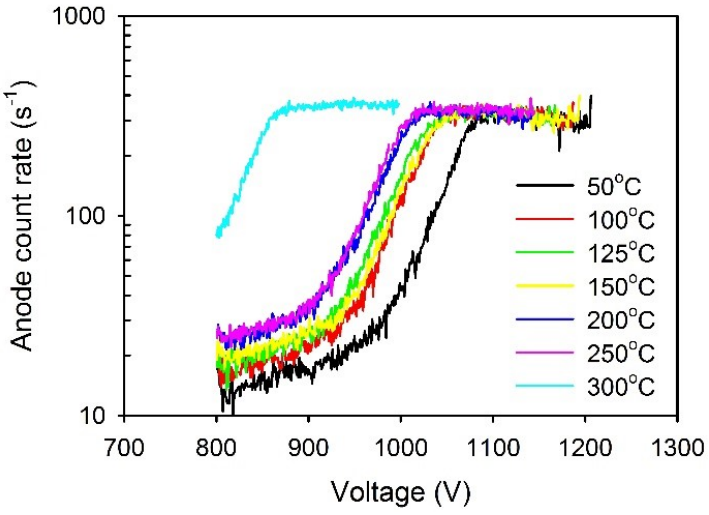


(a)

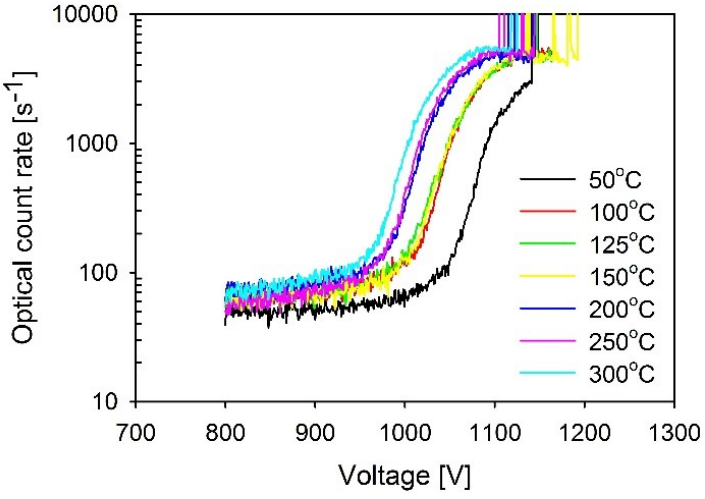


(b)

Figure A.7: Efficiency as a function of source temperature using a $^{63}$Ni source mounted on a stainless steel cup and the linear anode configuration. As the temperature is increased, both the proportional region and breakdown starts at a progressively lower anode voltage. a) Anode count rate as a function of voltage. The count rates are essentially independent of temperature in the plateau region. b) The UV intensity corresponding to the anode count rate in a). The electron:UV ratio on the plateau is independent of temperature (note that the 50 °C UV data do not reach the plateau before breakdown).

Table A.1: Comparison of the different anode configurations and detection modes using a $^{63}$Ni source operating in the GM region. The electron count rates are also given, normalised to that of the linear anode.

| | Ring Anode | Point Anode | PMT2 Gas Fluorescence | Linear Anode |
|---|---|---|---|---|
| Electron Counts ($s^{-1}$) | $174 \pm 2$ | $54 \pm 6$ | - | $258 \pm 3$ |
| UV Signal ($s^{-1}$) | $310 \pm 6$ | $250 \pm 21$ | $57 \pm 1$ | $3767 \pm 60$ |
| Normalised Efficiency | $67.7 \pm 1.3\%$ | $20.9 \pm 2.6\%$ | $22.1 \pm 0.6\%$ | 100% |

Table A.1 shows that the ring anode is 33% less efficient than the linear anode, and the point anode (and the UV signal recorded by PMT2) 79% less efficient. It is clear that the linear anode gives the highest count rate and would thus also appear to be the most sensitive. However, the ring anode is much more efficient in reducing the UV component recorded by the PMT ($310\pm\ 6\,s^{-1}$ rather than $3767\pm60\,s^{-1}$). While this is useful, our exo-electron sensitivity is much lower than our OSL sensitivity and so it is more important to maintain exo-electron count rate than to reduce the UV background underlying the OSL signal. Using the secondary PMT provides another measure of the exo-electron signal, but it also detects a significant TL/OSL signal from the sample; this is usually much stronger than exo-electron UV signal, and so this detector is of limited value.

### A.3.3 HV Modulation

REES uses HV-modulation to avoid contamination of the TL/OSL signal by gas fluorescence and so allows the simultaneous measurement of both TL/TSE and OSL/OSE. HV-modulation is common to all anode configurations and operations of REES.

The HV modulation frequency may be varied as appropriate; for fast decaying signals, such as the OSL fast component in quartz, a high frequency is required. To test the separation of exo-electron derived signals from potential luminescence signals we use graphite; graphite contains trapping states (Telling and Heggie, 2007) and so gives OSE but no OSL because recombination is non-luminescent, and so it can be used to demonstrate the effectiveness of the HV switching. Figures A.8a and A.8b show that there is no detectable optical (or anode) signal when the HV is off. The benefits of HV modulation during the measurement of TL is shown in Figures A.8c and A.8d for a chip of synthetic quartz; the modulation allows for clear distinction between the pure TL signal from the sample during the off-period and the combined TL and UV gas fluorescence during the on-period. The

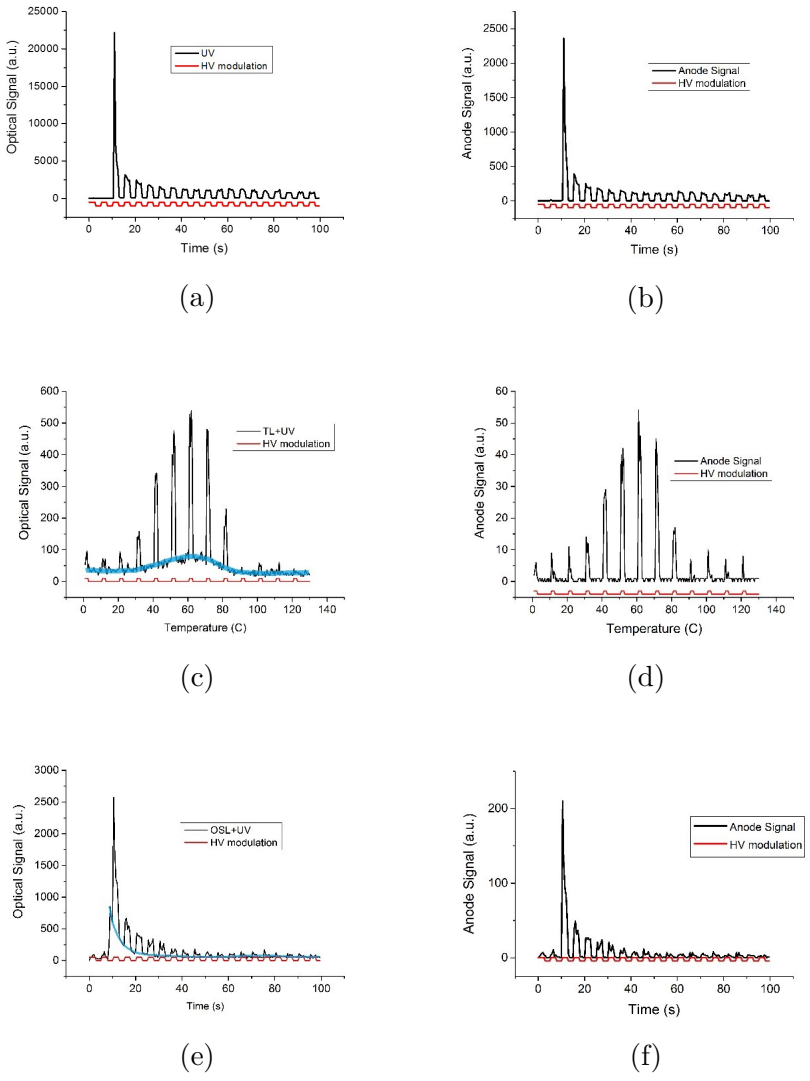


Figure A.8: Simultaneous measurement of UV (a) and OSE (b) from graphite (graphite does not produce OSL). Simultaneous TL+UV (c) and TSE (d) measurements of synthetic quartz with HV modulation, pure TL highlighted with blue. OSL+UV (e) and OSE (f) measurements on the same sample, pure OSL highlighted with blue. TL/TSE measured with a 4 channel on and 16 channels off (0.1 Hz) HV modulation. OSL/OSE measured with a 6 channel on and 5 channels off HV modulation (0.2 Hz).

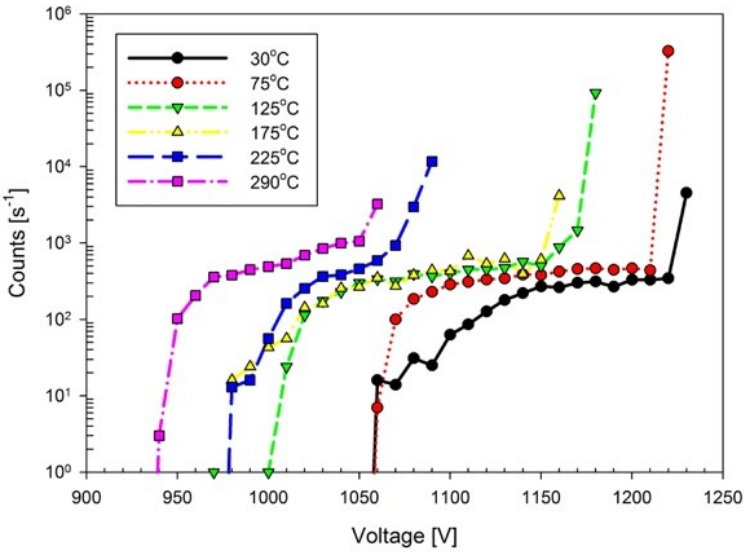


Figure A.9: The efficiency dependence on temperature for exo-electrons from quartz are very similar to those obtained for $^{63}$Ni (Figure A.7) although breakdown is more clearly defined. The count rates on the plateau are also similar, although the plateaus are not as flat as in Figure A.7

corresponding effect of HV modulation during OSL measurements is shown in Figures A.8e and A.8f. From these data it appears that the ratio of UV fluorescence count rate to anode signal count rate is similar for all 3 measurements, at about 10:1, suggesting considerable sensitivity advantage in using the UV signal to measure the rate of exo-electron emission. However, it must be recognised that the resulting signal is not likely to follow Poisson statistics, because each exo-electron presumably produces ∼10 correlated photons.

## A.4 Measurements on sedimentary quartz

One of the primary minerals used in luminescence dating is quartz and it is therefore important to show that REES is sufficiently sensitive to detect exo-electrons from sedimentary quartz grains.

### A.4.1 Dependence of efficiency on temperature: exo-electrons from quartz grains on stainless steel

Efficiency curves, similar to those shown for $^{63}$Ni (Figure A.7) but rather using calibration quartz (Hansen et al., 2015) are shown in Figure A.9. Several hundred 180-250 µm quartz grains were placed in a clean stainless steel cup, given a beta dose of 10 Gy and then stimulated with blue LEDs at different fixed temperatures and voltages until electrical breakdown is observed (Figure A.9). As with Figure A.7, we observe that the required voltage for proportional counting decreases with increasing temperature, although without increasing the count rate in the plateau region significantly.

For a measurement temperature of 125 °C the plateau is relatively wide (∼1050 to ∼1140 V). This allows the operation of the detector within a range of temperatures, but with almost constant gain. For instance by setting the HV to 1150 V the detector can be operated up to 175 °C without a large change in sensitivity. However, the efficiency plateau becomes significantly narrower as the sample temperature continues to increase, making it more difficult to operate the detector without breakdown. It is also interesting that the plateau regions at the various temperatures are not as well defined as found using the $^{63}$Ni beta source, and the change in absolute efficiency with temperature is somewhat larger than in Figure A.7. This may be a result of the very low residual energy with which exo-electrons are ejected into the counting gas. This would be expected to allow increased electron capture at low electron accelerations (low HV), but it is less obvious why increased gas temperature should also apparently decrease electron capture . Efficiency curves of similar form were also measured using NaCl (data not shown).

## A.5 Illustrative applications

Here we illustrate the potential of REES in studies of natural minerals by reporting various experiments involving multi-grain and single-grain samples of quartz.

### A.5.1 Multi-grain growth curve

The OSL/OSE response to dose of sedimentary quartz was measured using 100 grains of quartz mounted in a single-grain disc (Bøtter-Jensen et al., 2003) following a SAR protocol (Murray and Wintle, 2000) using a preheat of 260 °C for 10 s, and OSL/OSE measurement using the blue LEDS and

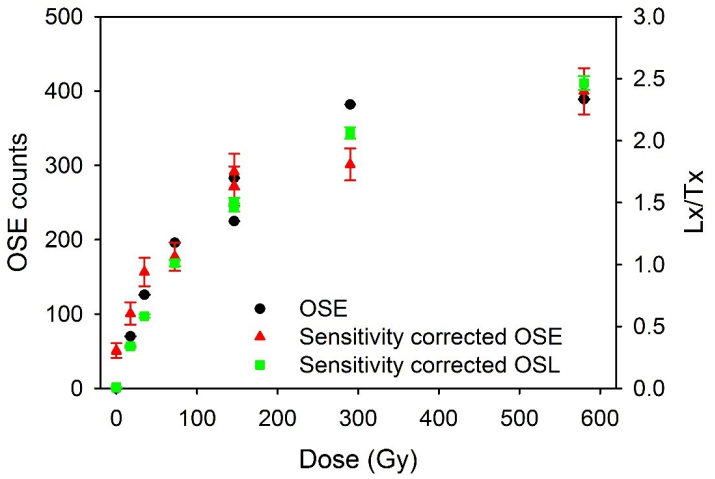


Figure A.10: Growth curves from 100 grains of calibration quartz. The curves are very similar to each other, however, sensitivity correcting the OSE signal results in a better recycling ratio ($0.92 \pm 0.14$) than doing a simple background subtraction (0.79). Each signal has been integrated for 0.4 s and had an early background subtraction i.e. the following 0.4 s

the sample held at 125 °C. The OSL and OSE were sensitivity corrected using a 100 Gy test dose with a cut-heat of 220 °C. The OSL and UV signals were separated using HV modulation (1.25 Hz, 0.4 s on / 0.4 s off).

Figure A.10 shows an OSE growth curve along with a sensitivity corrected OSE and OSL growth curve for the same sample. The signals were integrated for the initial 0.4 s and had an early background subtraction using the next 0.4 s. The three curves are virtually indistinguishable from one another suggesting a similar behaviour for the fast-components in both signals, as was earlier reported by Ankjærgaard et al. (2008, 2009).

### A.5.2 OSL and OSE dependence on prior heating and stimulation temperature

Natural dose measurements using OSL from sedimentary quartz involve thermal pretreatment and stimulation at elevated temperature (usually 125 °C) to ensure that the OSL signal is not influenced by shallow traps (e.g. the 110 °C TL trap in quartz). Varying the preheat and/or stimulation temperature in such measurements gives insights into the origins of the stored charge giving rise to the OSL, and into the characteristics of the recombination site (Spooner, 1994; Chen and McKeever, 1997 p. 74; Wintle and Murray, 1998, 2000). We chose such investigations to illustrate further

the flexibility and applicability of REES in the simultaneous measurement of OSL and OSE.

Here we first examine the dependence of fast-component OSL and fast-component OSE on prior heating. A pulse anneal experiment was performed by giving a quartz aliquot a dose of 30 Gy, preheating to some temperature between 160 °C and 300 °C, and measuring the OSL and OSE with the sample held at 125 °C. A test dose of 10 Gy, preheating to 220 °C and measuring the OSL and OSE with the sample held at 125 °C was used to sensitivity correct the OSL signal (but not the OSE as this remained stable, see also Ankjærgaard et al., 2008); the results of these experiments are shown in Figure A.11a. The sensitivity-corrected fast-component OSL remains constant between 160 °C and 250 °C; above this temperature the OSL begins to decrease due to thermal erosion of the 325 °C OSL trap (Wintle and Murray, 1998). However, the fast-component OSE measurements undertaken at the same time decrease steadily with preheat temperature, confirming the unexpected results of Ankjærgaard et al. (2008). Secondly, the effect of measurement temperature on the fast-component OSL and OSE signals was investigated by giving a quartz aliquot a dose of 30 Gy, preheating to 260 °C in order to empty shallow traps, and then performing OSL measurement at a range of temperatures from 50 °C to 300 °C. Once again, the OSL signal was sensitivity corrected using a 10 Gy test dose with a cut-heat of 220 °C and OSL measured at 125 °C.

If the HV is kept constant, the OSE and sensitivity-corrected OSL curves are consistent with those presented in Ankjærgaard et al. (2008). However, Figures A.7 and A.9 show that, if the voltage is kept constant, the detector will operate with very different efficiencies as the temperature is increased. In contrast, if the detector is kept operating at a voltage within the efficiency plateau for each measurement temperature, very different results are observed (Figure A.11b, black crosses). In this case the shape of the OSE variation with temperature is very similar to that of the OSL data. Nevertheless, this result remains unexpected because the decrease in OSL is believed to be due to thermal quenching of the signal (e.g. Spooner, 1994; Chen and McKeever, 1997 p. 74). If the OSE signal indeed reflects trap emptying, this suggests that, while thermal quenching presumably does occur, the fast-component trap is simultaneously emptied. Clearly the observations of Figure A.11 require further investigation.

### A.5.3 Single-grain operation

Initial testing has also been undertaken to investigate whether REES has sufficient sensitivity to make useful measurements of OSE from individual quartz grains. These tests employed both a standard Risø reader,

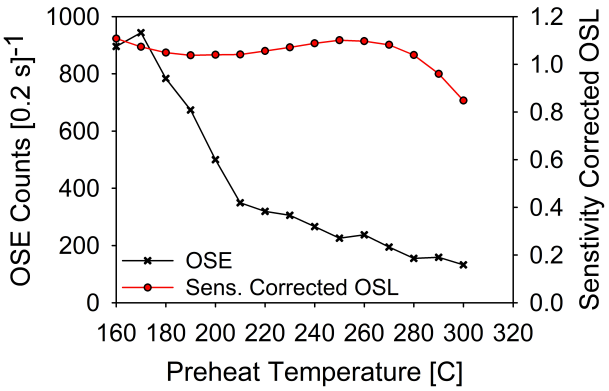


(a)

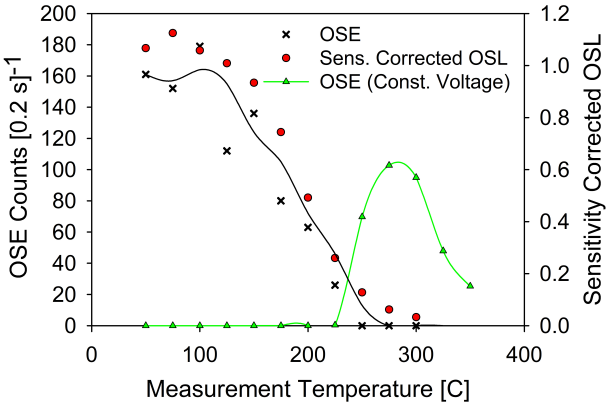


(b)

Figure A.11: Fast-component OSE and sensitivity corrected OSL as a function of preheat and measurement temperature. a) Pulse anneal measurements using a quartz aliquot measured at 125 °C. The (dimensionless) sensitivity corrected OSL (red circles) does not change significantly until 250 °C above which it starts to decline due to thermal erosion of the trap (Wintle and Murray, 1998). In contrast, the OSE decreases as a function of preheat temperature. b) OSL and OSE measurements of a quartz aliquot held at various temperatures during stimulation. The behaviour of the OSE signal (green triangles) when the HV is held constant and the sensitivity-corrected OSL (red circles) is consistent with that shown in Ankjærgaard et al. (2008). However, if the HV is adjusted to keep the detector on the efficiency plateau as the stimulation temperature is changed (see Figure A.9) the OSE signal (black crosses) decreases with stimulation temperature in a similar manner to the OSL.

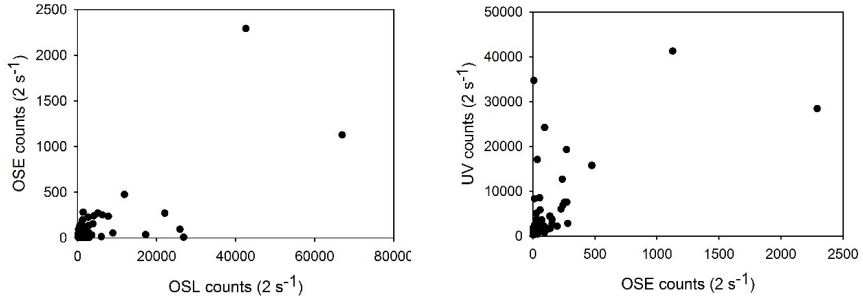


(a) (b)

Figure A.12: a) OSE counts against corresponding OSL counts. There is a weak correlation between OSE and OSL. b) UV count rate against corresponding OSE count rate. The UV signal is also weakly correlated with the OSE signal.

and a reader fitted with the automatic single-grain stimulation attachment (Bøtter-Jensen et al., 2003). The system uses a green laser (532 nm) to stimulate individual grains fixed in holes (300 µm in diameter, 300 µm deep) placed on a 10x10 grid with centre-to-centre distances of 600 µm.
Ninety-six single grains of calibration quartz (212-250 µm) were loaded in stainless steel cups (1 grain/cup), given a dose of 150 Gy, preheated to 260 °C for 10 s and measured using blue LEDs at 125 °C for 40 s with HV pulsing (0.4 s on / 0.4 s off). The results are presented in Figures A.12 to A.14.

Figure A.12a shows the correlation between OSL and OSE using the linear anode for collection of the OSE signal. There is a weak correlation between the two but the OSE signal is very weak. Figure A.12b shows the correlation between the UV signal and OSE; despite their common origin, the correlation is still not well defined, and the UV signal is much stronger. Figure A.13 is similar to Figure A.12a but shows the correlation of UV with OSL, rather than OSE with OSL. The correlation between exo-electrons and OSL is much better defined than in Figure A.12a.

As the UV signal has a much higher count rate than that of the electronic signal collected at the anode, it provides a better measure of the exo-electrons from individual grains. Using the HV modulation to record separate OSL and UV signals simultaneously enables us to have a second, more sensitive measurement of the exo-electron signal without losing information about the recombination. This is a major benefit of the new detector, and is clearly of particular value with single grain measurements.

Cumulative sum curves for both OSL and exo-electron signals are sim-

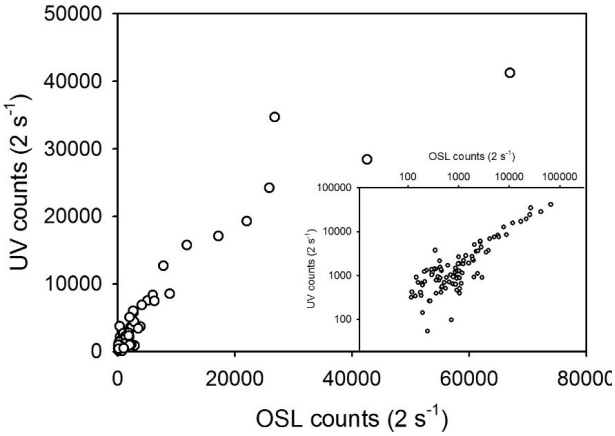


Figure A.13: UV counts against OSL counts (rather than OSE and OSL as in Figure A.12a). The UV signal is generated by the exo-electrons in the argon gas. Inset is plotted on a log-log scale

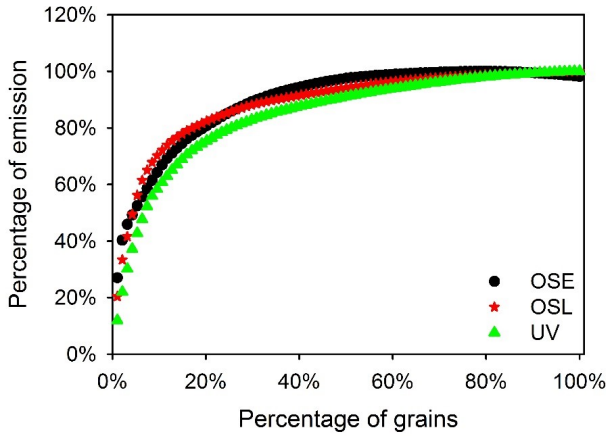


Figure A.14: Cumulative sums for OSL, OSE and UV signals for calibration quartz.

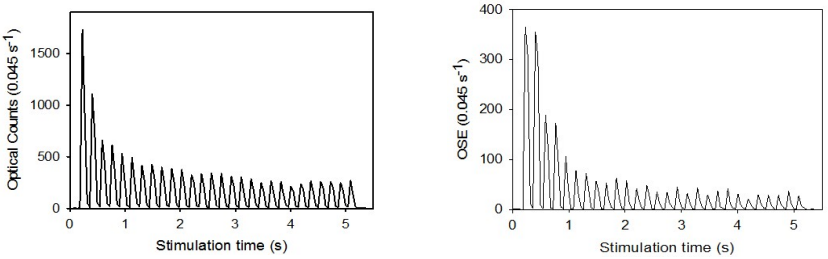


(a) (b)

Figure A.15: a) Optical (OSL and UV) from a single grain of calibration quartz (1 kGy), measured using the green laser at 125 °C. b) Corresponding OSE detected at the anode for the same grain and measurement. (with HV pulsing, 5.55 Hz, 0.09 s on / 0.09 s off)

ilar in shape. For calibration quartz, ∼80% of the luminescence and exo-electron signals come from ∼20% of the grains. These data were collected using individual grains on individual stainless steel cups, and stimulating with blue LEDs (470 nm). We have also made similar observations using the single-grain stimulation attachment; it appears that the single grain disc and green laser (532 nm) both reduce the number of exo-electrons detected. Comparing the electrical exo-electron signal measured on a cup with blue LEDs and in a single grain disc using the grain laser on the same grain, we observe an 84% drop in the total exo-electron signal. A similar comparison was made by summing the exo-electron signals for all grains when measured individually on a cup, with these measured in a single grain disc, both stimulated with blue LEDs. Here we see a 72% drop in exo-electron signal, this indicates that the single grain disc itself reduces the exo-electron signal; the difference does not arise only because of the longer wavelength simulation. On the other hand, comparing the total exo-electron signal for all grains in a single grain disc using the green laser and blue LEDs, we observe that the blue LEDs result in an extra 31% exo-electrons. This suggests that the 0.3 eV difference between the two stimulation wavelengths also has a significant impact on the exo-electron emission (see Figure A.1).

Nevertheless, using the single grain disc with green laser stimulation a few individual grains (6 out of 1700) have been observed which only showed an optical signal when the HV was turned on, i.e. little or no OSL production. Optical and OSE decay curves for such a grain are shown in Figure A.15.

It is clear from Figure A.15a that an optical signal is only present when the HV is turned on; this must derive only from exo-electron emission from

the grain. Although it is not yet known what fraction of grains falls into this category, the implication is clear: some grains can trap electrons in the apparently fast-component trap, but these electrons do not produce any OSL signal when stimulated. These data were collected using a green laser (532 nm); by using a shorter wavelength laser (e.g. 470 nm) it is likely that more such grains will be found.

## A.6 Conclusion

We have constructed and described a new exo-electron detection system compatible with the OSL stimulation/detection head of a Risø TL/OSL reader. This design improves on the previous detector presented by Ankjærgaard et al. (2006), particularly by incorporating HV-switching which allows the separation of uncontaminated luminescence signals (TL or OSL) from the UV signal generated by the corresponding exo-electrons. The detector comes with several different anode configurations; although the ring anode gives the best spatial separation of luminescence and UV fluorescence, the linear anode gives the highest counting efficiency. We have shown that it is possible to measure exo-electron signals from a laboratory pretreated quartz with absorbed doses of a few Gy and, using HV modulation, it will be possible to resolve much lower doses by using the UV signal produced by the de-excitation of argon atoms in the gas. The improved detector has been used to repeat thermal pretreatment and elevated stimulation experiments described previously; we confirm the results of the pulse anneal experiment, but show that the previously reported discrepancy between the dependence of OSE and OSL emission on stimulation temperature was probably an experimental artefact. The system is compatible with the single-grain attachment of a Risø TL/OSL reader and we have presented the first experimental observations of OSE from single grains of quartz. At the single grain level especially, the UV signal is very likely to provide a more sensitive measurement of exo-electrons. However, it should also be noted that the single-grain disc geometry and the green laser used for stimulation appear to be less efficient for exo-electron detection than the much more labour-intensive approach of placing individual grains separately on stainless steel cups and stimulating with blue LEDs.

**Acknowledgements**
M.A., N.R.J. P, and J.-P. B. receive funding from the European Research Council (ERC) under the European Union's Horizon 2020 research and innovation programme ERC-2014-StG 639904 - RELOS. The authors would

like to thank C. Ankjærgaard for sharing her experience with the previous exo-electron detector, and Louise M. Helsted and Vicki Hansen for help with samples. A special thanks to Lars P. Pirtzel, Jørgen H. Jacobsen, Søren V. Dalsgaard, Finn Jørgensen and Karsten B. Nielsen for their invaluable help and knowledge in the design, construction and integration of the detector with the Risø TL/OSL reader platform and software.

# References

Ankjærgaard, C., Murray, A. S., Denby, P. M., and Bøtter-Jensen, L. Measurement of optically and thermally stimulated electron emission from natural minerals *Radiation Measurements* 2006:**41**:780-786

Ankjærgaard, C., Denby, P. M., Murray, A. S., and Jain, M. Charge movement in grains of quartz studied using exo-electron emission *Radiation Measurements* 2008:**43**:273-277

Ankjærgaard, C., Murray, A. S., Denby, P. M., and Jain, M. Using optically stimulated electrons from quartz for the estimation of natural doses. *Radiation Measurements*. 2009:**44**:232-238

Ankjærgaard, C. Electron Emission from Natural Minerals: Implications for Charge Movement and Dosimetry. MSc. Thesis. Copenhagen University, Copenhagen, Denmark

Bøtter-Jensen, L., Bulur, E., Duller, G.A.T., Murray, A.S. Advances in luminescence instrument systems. *Radiation Measurements* 2000:**32**:523-528

Bøtter-Jensen, L., Andersen, C.E., Duller, G.A.T., Murray, A.S. Developments in radiation, stimulation and observation facilities in luminescence measurements *Radiation Measurements* 2003:**37(4-5)**;535-541.

Chen, R., McKeever, S.W.S., *Theory of Thermoluminescence and Related Phenomena* 1997. World Scientific, Singapore, p. 559.

Davies, J. E. Exoemission and thermoluminescence from human enamel and shark enamleoid. *Radiation Protection Dosimetry* 1983:**4(3/4)**:181-184

Davies, J. E., and Townsend, P. D. Exoemission of Ethiopian soils and the endemicity of non-filarial elephantiasis *Radiation Protection Dosimetry* 1983:**4(3/4)**:185-188

Ikeya, M. Dating a stalactite by electron spin resonance *Nature* 1975:**255**:48-50

Ikeya, M. Electron Spin Resonance (ESR) Microscopy in Materials Science *Annu. Rev. Mater. Sci.* 1991:**21**:45-63

McKeever, S.W.S. *Thermoluminescence of solids* 1985 Cambridge University Press pp 376

Milsch, B., Kerbe, F., and Michalowsky, L. Defect Centres in Beryllium Oxide Ceramic Studied by Electron Paramagnetic Resonance (EPR) *Ceramics International* 1990:**16**:311-318

Murray A.S. and Wintle A.G. Luminescence dating of quartz using an improved single-aliquot regenerative-dose protocol *Radiation Measurements* 2000:**32(1)**;57-73.

Oster, L., Yaskolko, V., and Haddad, J. Classification of exoelectron emission mechanisms *Phys. Status Solidi* 1999:**174**:431-439

Spooner, N.A. On the optical dating signal from quartz *Radiation Measurements* 1994:**23**:593-600

Telling, R. H., and Heggie, M. I. Radiation defects in graphite *Philosophical Magazine* 2007:**87(31)**:4797-4846

Thomsen, K.J., Murray, A.S., Bøtter-Jensen, L. Sources of variability in OSL dose measurements using single grains of quartz *Radiation Measurements* 2005:**39**:47-61

Tsukamoto, S., Murray, A., Ankjærgaard, C., Jain, M., and Lapp, T. Charge recombination processes in minerals studied using optically stimulated luminescence and time-resolved exo-electrons *J. Phys. D: Appl. Phys.* 2010:**43**:325502

Tsukamoto, S., Toyoda, S., Tani, A., Opperman, F. Single aliquot regenerative dose method for ESR dating using X-ray irradiation and preheat

*Radiation Measurements* 2015:**81**:9-15

Tsukamoto, S., Porat, N., Ankjærgaard, C. Dose recovery and residual dose of quartz ESR signals using modern sediments: Implications for single aliquot ESR dating *Radiation Measurements* 2017:**106**:472-476

Turner, J. E. *Atoms, Radiation, and Radiation Protection* 1995 John Wiley & Sons, Inc., New York, NY, USA, 2nd edition. ISBN 0-471-59581-0

Wintle, A. G., Murray, A. S. Towards the development of a preheat procedure for OSL dating of quartz *Radiation Measurements* 1998:**29**:81-94

Wintle, A.G., Murray, A. S. Quartz OSL: Effects of thermal treatment and their relevance to laboratory dating procedures *Radiation Measurements* 2000:**32**:387-400

Zastawny, A., and Białoń, J. Influence of the mechanical sample treatment on the thermally stimulated exoelectron emission in aspect of the application for sample dating *Applied Radiation and Isotopes* 1998:**50**:673-676

Zimmerman, J. The radiation-induced increase of the 100 °C thermoluminescence sensitivity of fired quartz *J. Phys. C: Solid St. Phys.* 1971:**4**:3265-3276